DEPARTMENT OF PHYSICS
UNIVERSITY OF JYVÄSKYLÄ
RESEARCH REPORT No. 7/2017

JET FRAGMENTATION TRANSVERSE MOMENTUM FROM h–h CORRELATIONS IN pp AND p–Pb COLLISIONS

BY

JUSSI VIINIKAINEN

Academic Dissertation
for the Degree of
Doctor of Philosophy

To be presented, by permission of the
Faculty of Mathematics and Science
of the University of Jyväskylä,
for public examination in Auditorium FYS1 of the
University of Jyväskylä on December 15, 2017
at 12 o'clock noon

Jyväskylä, Finland
December 2017

PERSONAL CONTRIBUTION

Viinikainen, Jussi
Jet fragmentation transverse momentum from h–h correlations in pp and p–Pb collisions
Jyväskylä: University of Jyväskylä, 2017, 114 p.
Department of Physics Research Report No. 7/2017
ISSN 0075-465X; 7/2017
ISBN 978-951-39-7288-2 (paper version)
ISBN 978-951-39-7289-9 (electronic version)
Diss.

Keywords: Jet, fragmentation, transverse momentum, ALICE, correlations, proton, lead, CERN, LHC

The main contributions of the author to the research presented in this thesis are listed below.

- Commissioning and maintenance of the level-0 trigger of the electromagnetic calorimeter at the ALICE experiment. (Section 2.3.6)
- Jet fragmentation transverse momentum (j_{T}) analysis for $\sqrt{s} = 7\,\mathrm{TeV}$ pp data and $\sqrt{s_{\mathrm{NN}}} = 5.02\,\mathrm{TeV}$ p–Pb data.
  - Implementation for the observable j_{T} (Section 4.2).
  - Implementation for the background of the j_{T} distribution (Section 4.2).
  - Deriving the acceptance correction for the analysis (Section 4.4).
  - Validating analysis assumptions using PYTHIA 8 simulation (Section 4.5).
  - Fitting the measured j_{T} distributions (Section 4.6).
  - Deriving the final results from the fit parameters (Section 4.7).
  - Systematic uncertainty analysis (Chapter 5).
  - Interpretation of the results and comparing data to models (Chapter 6).

Author

Jussi Viinikainen
University of Jyväskylä
Helsinki Institute of Physics
Finland

Supervisor

Professor Jan Rak
University of Jyväskylä
Helsinki Institute of Physics
Finland

Reviewers

Professor Olga Evdokimov
University of Illinois at Chicago
USA

Doctor Nathan Grau
Augustana University
USA

Opponent

Professor Gunther Roland
Massachusetts Institute of Technology
USA

PREFACE

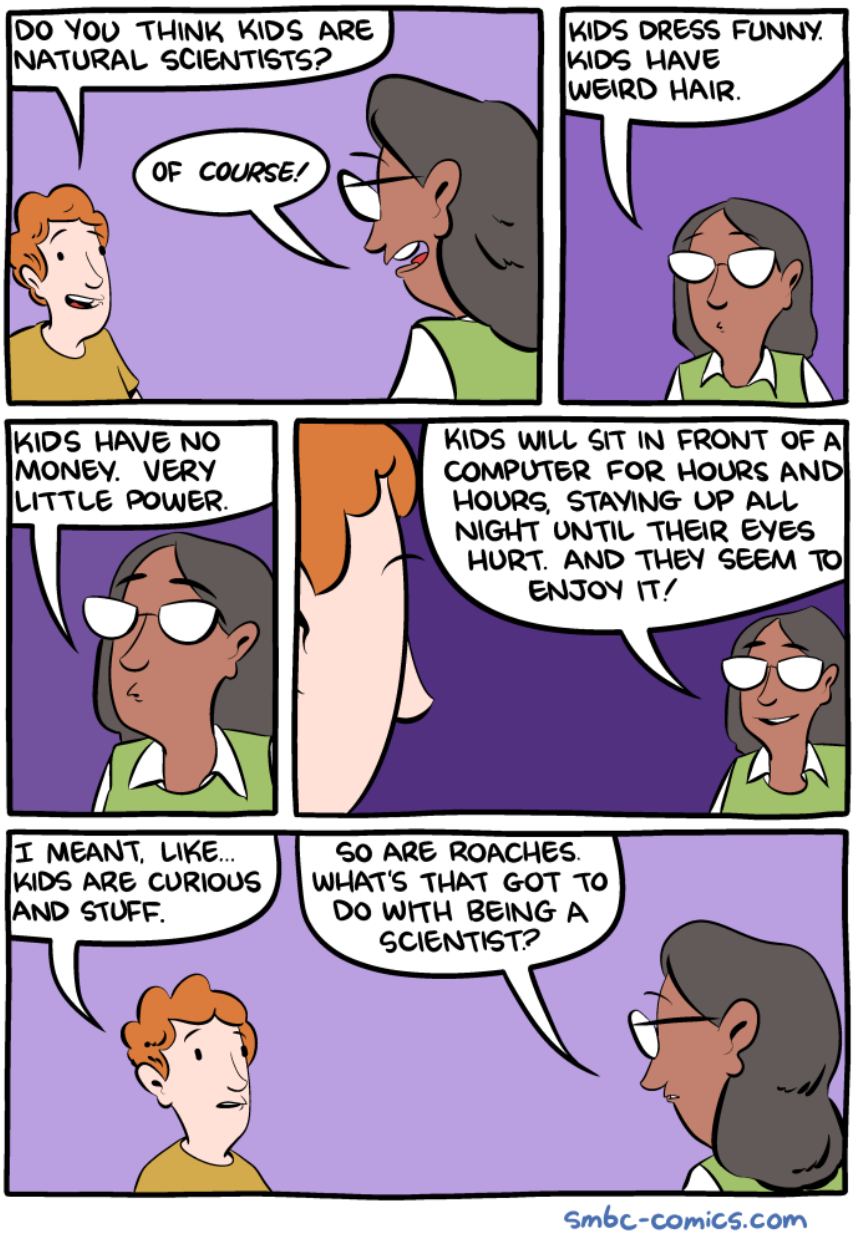

FIGURE 1 Cartoon drawn by Zach Wienersmith.

ACKNOWLEDGEMENTS

The work presented in this thesis has been carried out between 2012 and 2017 at the University of Jyväskylä and at CERN. Here, in the beginning of my thesis, I would like to acknowledge the help I have received from several other people that has made my graduation possible.

First, I would like to than my supervisor Jan Rak. Under his guidance I have learned how to become an independent researcher, which is a quality that is for sure helpful in the future.

From our research group, I would also like to highlight Sami Räsänen and Dong Jo Kim. The support I have received from Sami has been invaluable. We have had numerous discussions on physics and practical issues during the PhD work, and Sami also provided a lot of feedback from my thesis. With Dong Jo we have also had physics discussions and his pieces of advice on how to write analysis code have been helpful in improving the analysis techniques.

Regarding the experimental work at CERN, I would like to thank Jiří Král for teaching me all I know about the level-0 trigger system of the electromagnetic calorimeter in ALICE. I would also like to thank Martin Poghosyan for his help and advice regarding the practical work with the detector.

I would like to thank Olga Evdokimov and Nathan Grau for reviewing my thesis and providing useful comments and Gunther Roland for promising to be my Opponent.

For providing me things to do also outside physics, I would like to thank my friends both in Jyväskylä and in CERN. This aspect should not be underrated.

A special thanks goes also to my family, from which I can always get unconditional love and support.

I would also like to acknowledge the financial support I have received from the University of Jyväskylä, the Magnus Ehrnrooth foundation and the Helsinki Institute of Physics. You cannot do science with an empty stomach.

CONTENTS

1 INTRODUCTION

The nature is governed by four basic interactions: electromagnetic, strong, weak and gravity. While the gravity is best modeled by the theory of relativity [1], all the other forces are very successfully and accurately described in the Standard Model of particle physics [2]. The Standard Model consists of the electroweak model [3–5] combining the electromagnetic and weak interactions, and quantum chromodynamics (QCD) [6] describing the strong interactions. This thesis concentrates on studying QCD. The constituents of matter interacting via the strong force are quarks and these interactions are mediated by gluons. A peculiar feature of QCD is that no free quarks or gluons can be seen in the nature under normal conditions [7], they are always confined into bound states called hadrons. However, the quarks can be seen indirectly in high energy particle collisions as jets [8], streams of collimated final state particles.

Jets in high energy particle collisions have been studied already for over 50 years. In theory descriptions, jet fragmentation is usually modeled in two phases. The fragmentation starts with a perturbative parton shower phase that is followed by a non-perturbative hadronization phase, where the generated partons are transformed into final state hadrons. Experimentally jets are often studied using a jet reconstruction algorithm, which clusters final state particles in order to find a reasonable representation of the initial parton kinematics [9]. Another approach, which is also the one adopted in this thesis, is to study jets using dihadron correlations and obtain the jet properties statistically. The main observable in the thesis is the jet fragmentation transverse momentum j_{T}, which is defined as the momentum component of the jet fragment perpendicular to the jet axis. The jet axis is the axis around which the jet fragments are distributed, and it is thought to coincide with the momentum vector of the parton initiating the fragmentation process. We argue that when we study a biased sample of events containing high transverse momentum trigger particles, we can distinguish different components for the parton shower and hadronization phases of the jet fragmentation from the measured j_{T} distributions. The main goal of the thesis is to extract the RMS and per trigger yield for both of these components from the j_{T} distributions.

This thesis is organized as follows. In Chapter 1 first a general introduction to QCD and heavy ion physics is given. Then the discussion concentrates on how jet fragmentation is treated in perturbative QCD calculations and in PYTHIA [10,11] and Herwig [12,13] Monte Carlo event generators.

Chapter 2 introduces the CERN accelerator facilities. A special emphasis is given for the ALICE experiment, as I am a member of this experiment and all the data shown in this thesis is measured by the ALICE detector. In this chapter I will also discuss my personal contribution to the L0 trigger system of the electromagnetic calorimeter.

The event and track selection used in the analysis are presented in Chapter 3. Then the analysis details are discussed in Chapter 4. This chapter begins with an introduction to the two-particle correlation technique, which is the main analysis method used in this thesis. The observable j_{T} and the required corrections to the raw data are introduced. Finally the used fitting methods and the mathematics behind the final results are discussed.

Before going to final results, the different sources of systematic uncertainties are explained in Chapter 5. After that, the final results for $\sqrt{\langle j_{\mathrm{T}}^2 \rangle}$ and per trigger yields of j_{T} distributions are presented and interpreted in Chapter 6. Also comparisons of ALICE data to PYTHIA and Herwig event generators are presented. In the end the main results are summarized and an outlook for the analysis is given in Chapter 7.

1.1 Quantum chromodynamics

The Standard Model of particle physics is a quantum field theory, in which the particle interactions are dictated by local gauge symmetries [8]. The symmetry group of the Standard Model is SU(3)×SU(2)×U(1). The different groups here correspond to different fundamental interactions of nature. The classical quantum field theory for electromagnetic interactions is the quantum electrodynamics (QED), which has the symmetry group U(1) encoding the conservation of electric charge. In the Standard Model the electromagnetic and weak interactions are coupled together to an electroweak model with the symmetry group SU(2)×U(1). The Higgs sector and massive gauge bosons are included to the model by spontaneously breaking the local gauge symmetry by selecting a specific ground state. What is left for the strong interactions is the group SU(3), and the corresponding theory is called quantum chromodynamics. SU(3) guarantees the conservation of the color charge.

QCD has many interesting properties stemming from the fact that the underlying symmetry group is SU(3). This group consist of unitary 3×3 matrices with $\det U = 1$. The fundamental representation of SU(3) is a triplet, which leads to the fact that there are three possible color charges for quarks. When a quark is said to belong to a color triplet, it means that a quark can carry any of these three charges. The number of colors has been experimentally confirmed to be 3 by

studying, for example, the neutral pion decays to two photons [14] and comparing the measured decay width to theory calculations for different number of colors. The group has $3^2 - 1 = 8$ generators T_a, which are a set of linearly independent traceless hermitian 3×3 matrices. This reflects the fact that gluons can have eight different color charges, and are thus said to be color octet states. As no colored particles are observed in nature, the quarks and gluons must connect into color neutral states to form the observed particles. A color neutral state is also called a color singlet.

Arguably the most interesting properties of QCD come from the fact that the generators of SU(3) do not commute with each other. Instead, for them it holds that

$$[T_a, T_b] = i f_{abc} T_c \ , \tag{1}$$

where f_{abc} are real constants, called the structure constants of SU(3). The implications of this non-Abelian nature of SU(3) can be seen when we write the gauge invariant QCD Lagrangian:

$$\mathcal{L} = \bar{q}_j (i\gamma^\mu \partial_\mu - m) q_j - g_\mathrm{s} (\bar{q}_j \gamma^\mu T_a q_j) G^a_\mu - \frac{1}{4} G^a_{\mu\nu} G^{\mu\nu}_a \ . \tag{2}$$

In the Lagrangian q_j and $\bar{q}_j$ are the color and anticolor fields for color j, g_s is the coupling strength, γ^μ is a gamma-matrix, G^a_μ is the gauge field for color a and $G^a_{\mu\nu}$ is the field strength tensor for color a. The local gauge invariance requires that the field strength tensor is of the form

$$G^a_{\mu\nu} = \partial_\mu G^a_\nu - \partial_\nu G^a_\mu - g_\mathrm{s} f_{abc} G^b_\mu G^c_\nu \ . \tag{3}$$

We can read the interactions of the theory from the Lagrangian. The first term in equation (2) has two color fields, so it describes the free propagator for the quarks. The second term specifies the coupling of quarks to gluons. In the third term there are three different terms for gluons, containing two, three, and four gauge fields, as can be seen from the specific form of the field strength tensor in equation (3). This means that in addition to the free gluon propagator, also three-gluon and four-gluon interaction vertices arise. The fact that gluons can also couple with themselves has several striking features, which will be explored in more detail in the next section.

1.1.1 Asymptotic freedom

The strong coupling constant g_s is, in fact, not a constant as its effective strength depends on the energy scale of the system. When the energy scale is high, the coupling becomes small. This behavior is called the asymptotic freedom of QCD [15–17]. Intuitively, this behavior can be understood as a vacuum polarization effect [18]. Imagine you have two test color charges. The vacuum between them has $\mathrm{q\bar{q}}$-fluctuations, but also purely gluon fluctuations since gluons have self-coupling in QCD. The test charge polarizes the vacuum aligning the $\mathrm{q\bar{q}}$-fluctuations in such a way that they act like a screen between the charges. This means that when the charges are brought closer together, they feel each others

charge stronger. The effect of gluon fluctuations turns out to be exactly opposite. Because gluons have an integer spin, the test charge tends to polarize the vacuum in such a way that, for example, a red color charge gets predominantly surrounded by more red charge. This creates an antiscreening effect, where the charge felt by the test charges decreases as they are brought closer together as they penetrate the sphere of predominantly red charge. Antiscreening turns out to produce a stronger effect than screening, and thus the effective interaction strength decreases as the charges are brought closer to each other. Short length scales here correspond to large energy transfer scales in collider experiments.

The formal derivation of the running coupling from QCD requires introduction of renormalization groups and is beyond the scope of this thesis. Interested readers can look for more details, for example, from [19]. The evolution of the strong coupling constant is given by so-called β-function and the lowest order result turns out to be

$$\alpha_s = \frac{g_s^2}{4\pi} = \frac{1}{\beta_0 \ln(Q^2/\Lambda_{QCD}^2)} , \tag{4}$$

where β_0 is the 1-loop β-function coefficient, Q^2 the energy scale and Λ_{QCD} the QCD scale, which gives the energy scale where β-function diverges and α_s becomes infinite. Λ_{QCD} is an important parameter in QCD, since it gives the energy scale above which the perturbative approach starts to make sense and Feynman rules can be applied to solve problems. Below Λ_{QCD} the coupling becomes large and non-perturbative methods must be used. The value of Λ_{QCD} is renormalization scheme dependent. The most used scheme nowadays is the modified minimal subtraction ($\overline{\text{MS}}$) scheme [20]. For this scheme and for 5 effective quark flavors the current world average value is $\Lambda_{QCD}^{\overline{\text{MS}}} = (210 \pm 14)$ MeV [2].

The evolution of the strong coupling constant as a function of the energy scale Q is presented in Figure 2. The colored points in the figure show the measured data from different types of experiments. Different experiments have extracted α_s to a different order in perturbation theory, where LO denotes the leading order and each N preceding it indicates going to higher orders. The black line is the QCD prediction, provided that the value of α_s at the mass of the Z^0 boson is the current best world average $\alpha_s(M_{Z^0}) = 0.1181 \pm 0.0011$ [2]. We see that the theory curve matches the experimental results really well.

The behavior of α_s also gives an explanation why we do not observe free colored particles. Consider again the system of two test charges. The color charge is seen stronger when the test charges are farther apart. The potential energy of the system turns out to be proportional to the distance of the color charges $V(r) \propto r$. The nature tends to minimize the energy of a given system and this minimum energy principle leads to states where colored particles are confined into colorless hadrons.

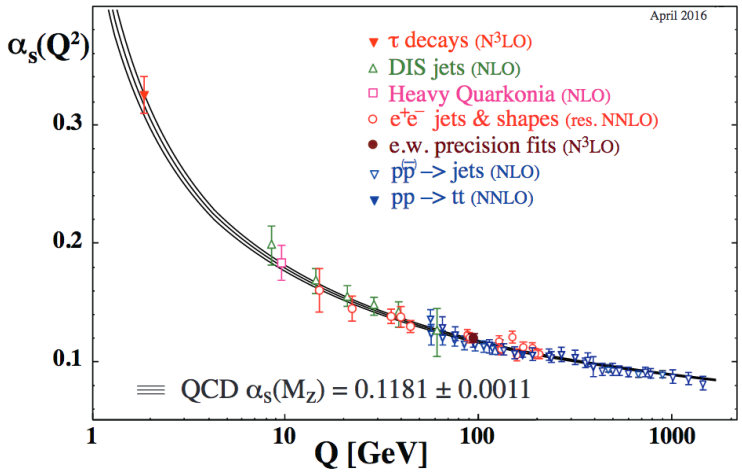

FIGURE 2 Summary of measurements of α_s as a function of the energy scale Q. Figure from [2].

1.2 Heavy ion physics

1.2.1 Nuclear phase diagram

The asymptotic freedom leads to a prediction that at high enough energy densities a new phase of nuclear matter emerges [21]. This phase consists of quarks and gluons that are no longer confined to colorless hadrons, but can move freely within this quark-gluon plasma. Experimentally high enough energy densities to produce quark-gluon plasma can be obtained in heavy ion collisions. The experimental heavy ion program started in 1984 in the Plastic Ball experiment in Bevalac [22]. The program continued later in the 1980s when the Alternating Gradient Synchrotron (AGS) in Brookhaven National Laboratory (BNL) and Super Proton Synchrotron (SPS) at CERN became operational at 1986. There were some hints of quark-gluon plasma found by the AGS [23] and a lot more by the SPS [24–27]. However, the existence of the quark-gluon plasma was not truly confirmed until 2005 at the Relativistic Heavy Ion Collider (RHIC) in BNL [28–31]. At RHIC also deuteron-ion collisions were measured together with ion-ion collisions ruling out explanations that the observed signals would be initial state effects [32–35]. At the present day RHIC is still operational and heavy ions are collided also by the Large Hadron Collider (LHC) at CERN. As the existence of the new phase of matter is already confirmed, the goal of the heavy ion physics at the moment is to study the properties of the quark-gluon plasma and to continue exploring the nuclear phase diagram.

A schematic picture of the nuclear phase diagram is shown in Figure 3. In this figure the vertical axis is temperature and the horizontal axis is net baryon density (the density of baryons minus the density of antibaryons). The black point at low temperature and where the net baryon density is normalized to 1 is the region where nuclei are under normal conditions. The quark-gluon plasma

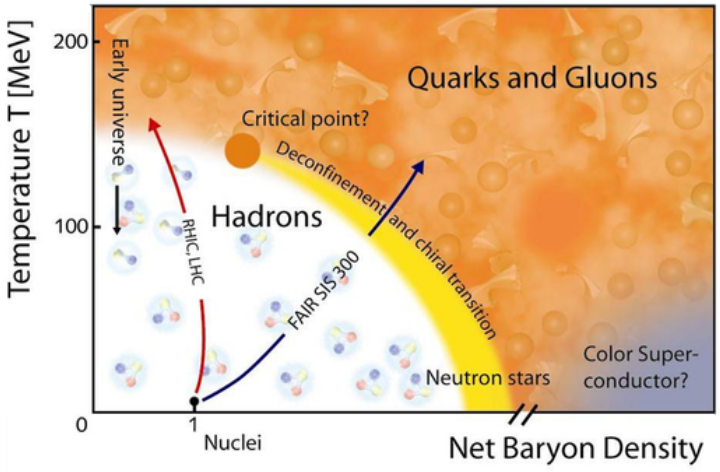

FIGURE 3 A schematic picture of the nuclear phase diagram. Figure from [43].

phase is found at high temperatures and densities. There is also a predicted color superconductor phase [36] in low temperature and high density region. The high energy particle colliders like RHIC and LHC probe the high temperature and low density region. In this region a cross-over transition from the quark-gluon plasma phase to the hadronic phase is predicted by lattice calculations [37]. Experimentally the nature of the phase transition and the existence of the critical point are studied, for example, by the STAR collaboration, which has measured the net-charge multiplicity distributions for several different beam energies at RHIC [38]. However, no definitive conclusions can be made from the currently available data. Lattice calculations also predict a first order phase transition at higher densities [39]. Currently this region has only been partially probed experimentally. In the future RHIC will continue probing the nuclear phase diagram in the phase 2 of the beam energy scan [40]. There are also two facilities under construction, the FAIR accelerator facility in Germany [41] and the NICA accelerator facility in Russia [42], that aim to study the unexplored region of the nuclear phase diagram by creating quark-gluon plasma at moderate temperature and high density.

1.2.2 Developments on quark-gluon plasma signatures

One of the first signs of quark-gluon plasma was the discovery of hydrodynamical flow, where the internal pressure of the created blob of quark-gluon plasma turns the initial state spatial anisotropies into final state momentum anisotropies as illustrated in Figure 4. The anisotropic flow is characterized using a Fourier decomposition of the azimuthal angle distribution of the produced particles with respect to a symmetry plane [44]

$$E\frac{\mathrm{d}^3N}{\mathrm{d}^3p} = \frac{1}{2\pi}\frac{\mathrm{d}^2}{p_\mathrm{T}\mathrm{d}p_\mathrm{T}\mathrm{d}\eta}\left(1+2\sum_{n=1}^{\infty} v_n(p_\mathrm{T},\eta)\cos[n(\varphi-\Psi_\mathrm{n})]\right), \tag{5}$$

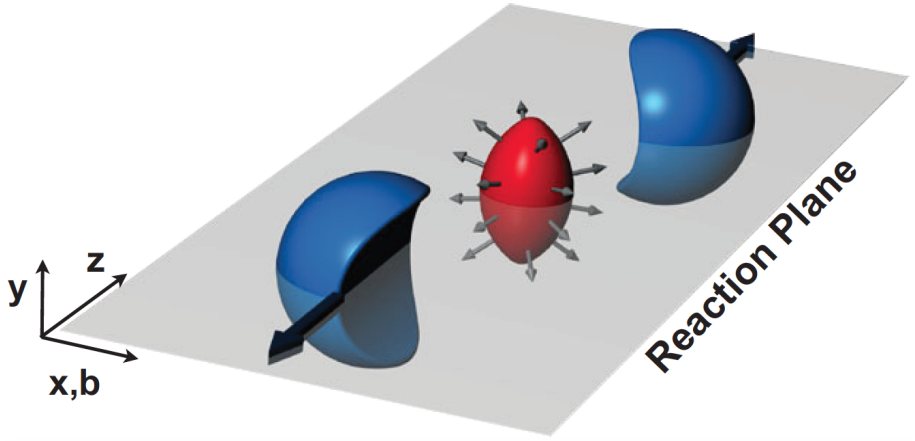

FIGURE 4 The internal pressure of the created quark-gluon plasma turns the initial spatial anisotropies into final momentum anisotropies in the phenomenon called flow. Figure from [44].

where E, p, p_{T}, φ and η are the energy, momentum, transverse momentum, azimuthal angle and pseudorapidity of the particle. The number 1 before the sum corresponds to the spectrum averaged over the azimuthal angle. At low p_{T}, this carries information about the radial flow, which is the dominant flow phenomenon [45,46]. The coefficients v_n describe the shape of the flow. In non-central collisions the dominant coefficient in the expansion is the elliptic flow v_2, reflecting the geometric shape of the collision. In the most central collisions the biggest contribution is given by the triangular flow v_3 [47], originating from the initial state fluctuations. The angle Ψ_{n} is the symmetry plane angle of the harmonic v_n, which might deviate from the reaction plane in Figure 4 due to initial state fluctuations.

Recently ALICE has measured the correlations between higher order and lower order flow harmonics [48] to constrain the value of the sheer viscosity over entropy ratio η/s, which describes the strength of viscous corrections to ideal non-viscous hydrodynamics. The higher order harmonics are sensitive to the fluctuations of the initial conditions and the magnitude of η/s [49, 50], while the v_n correlations have potential to discriminate between these two contributions [51]. The correlations are measured using symmetric cumulants [52], defined as $\mathrm{SC}(n,m) = \langle v_n^2 v_m^2 \rangle - \langle v_n^2 \rangle \langle v_m^2 \rangle$. The measured values as a function of centrality are shown in Figure 5. The positive value for $\mathrm{SC}(4,2)$ means, that for events where the elliptic flow v_2 is stronger than average, also the quadrangular flow v_4 is likely to be stronger than average. Similarly the negative value for $\mathrm{SC}(3,2)$ means that if elliptic flow v_2 is stronger than average, the triangular flow v_3 is likely to be weaker than average. All the correlations are increasing with increasing centrality, which is expected as at higher centralities the initial state is more anisotropic causing more flow in the first place. Lately this analysis has been extended to higher order cumulants, where the correlations are smaller but sensitivity to initial conditions and η/s is improved [53]. Conclusions from these studies can be drawn by comparing the experimental results to different model calculations. It turns out

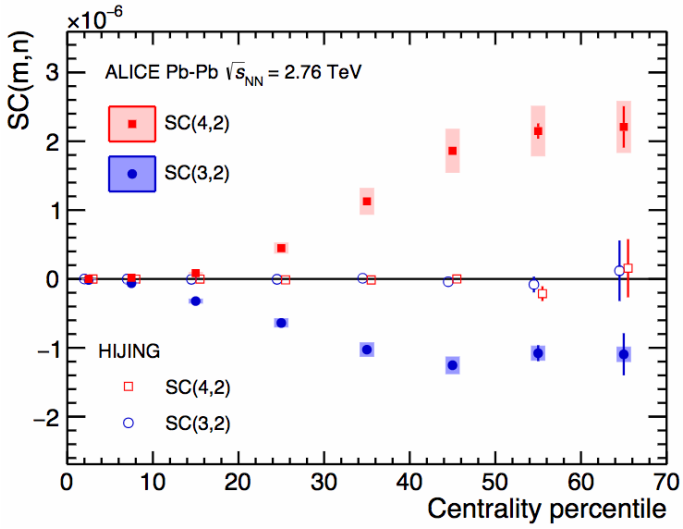

FIGURE 5 Correlations of flow coefficients as a function of centrality measured by the ALICE experiment. The notation SC(n,m) stands for symmetric cumulant of v_n and v_m, which measures the correlation between these two coefficients. Figure from [48].

that the ALICE data supports a low value for η/s and initial conditions such as in the AMPT [54–56] and EKRT [57] models.

If a di-jet is produced near the surface of a blob of quark-gluon plasma, experimentally only one clear jet peak is seen [58]. As the other jets goes through the medium, it loses energy as it interacts with the medium and produces more lower momentum particles that spread into much wider area as compared to a jet in vacuum. This phenomenon is called jet quenching and it provides more evidence for the creation of the new phase of matter. Initially the jet quenching was assessed with the nuclear modification factor R_{AA} [59], defined as the ratio of charged particle yield in nucleus-nucleus collisions and the charged particle yield in proton-proton collision scaled by the mean number of binary nucleon-nucleon collisions

$$R_{AA}(p_{\mathrm{T}}) = \frac{\left(1/N_{\mathrm{evt}}^{AA}\right) \mathrm{d}^2N_{\mathrm{ch}}^{AA}/\mathrm{d}\eta\mathrm{d}p_{\mathrm{T}}}{\langle N_{\mathrm{coll}}\rangle \left(1/N_{\mathrm{evt}}^{\mathrm{pp}}\right) \mathrm{d}^2N_{\mathrm{ch}}^{\mathrm{pp}}/\mathrm{d}\eta\mathrm{d}p_{\mathrm{T}}} \,. \tag{6}$$

At RHIC a suppression of a factor of 5 was reported for high-p_{T} particles in central heavy ion collisions [30,31]. At LHC, the suppression of high-p_{T} particles is a bit stronger, as can be seen, for example, from a study done by ALICE [60] presented in Figure 6. The stronger suppression in the region $5 < p_{\mathrm{T}} < 10$ GeV/c tells us that the quark-gluon plasma created in LHC is denser than in RHIC due to larger collisions energy. The peak around $p_{\mathrm{T}} = 2$ GeV/c may reflect a variation of particle composition in heavy ion collisions with respect to pp collisions [61,62].

More recently CMS experiment has been studying more carefully where does the energy lost by the quenched jet go. They report that there is a strong enhancement of low-p_{T} particles at large angles with respect to the jet axis in central heavy ion collisions [63]. The overall momentum balance can be restored when these particles are taken into account.

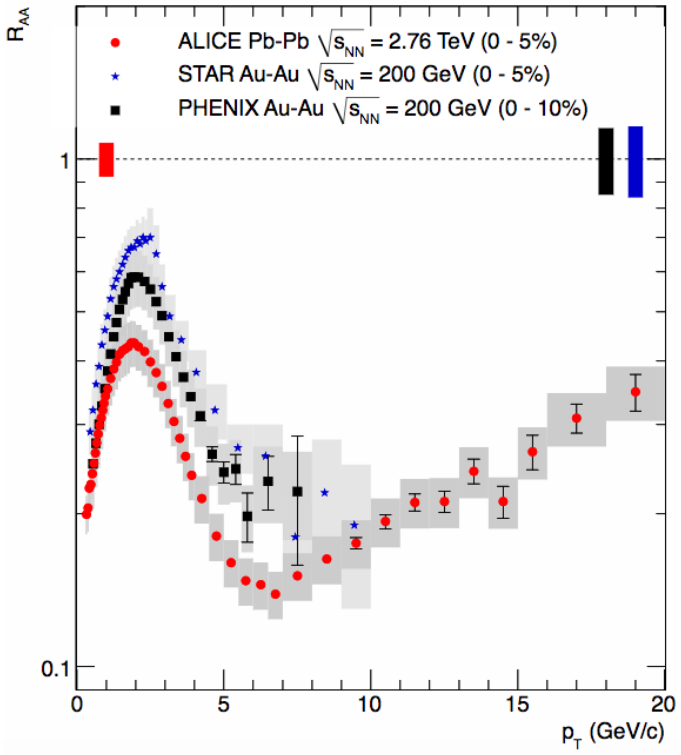

FIGURE 6 The R_{AA} measured by the ALICE experiment (red) compared to previous measurements by STAR (blue) and PHENIX (black). Figure from [60].

There are also efforts to study jet quenching from Z^0 boson - jet correlations. Using Z^0 bosons as a probe instead of charged particles gives a better handle to the initial parton energy since Z^0 bosons do not interact strongly with the quark-gluon plasma [64–66]. The background is also very clean for Z^0 bosons, which makes them a better probe than isolated photons which suffer from photons created in the jet fragmentation process [67,68]. Furthermore, the Z^0+jet production is dominated by quark jets for $p_{\mathrm{T}}^{\mathrm{jet}} \gtrsim 30$ GeV/c [69], providing extra information on parton flavor and kinematics [69]. Thus Z^0-jet correlations are very well suited to do tomographic studies for quark-gluon plasma. A study from CMS [70] reports that the average number of jet partners per Z^0 boson is lower in Pb–Pb than in pp collisions, suggesting that larger fraction of jets associated with Z^0 bosons lose energy and fall below the threshold of $p_{\mathrm{T}}^{\mathrm{jet}} = 30$ GeV/c used in the analysis. This provides new input for determination of jet quenching parameters.

Quark-gluon plasma can also be studied via quarkonium. A quarkonium state consists of a heavy quark and its antiquark. It is expected that the production of quarkonium is significantly suppressed in heavy ion collisions as compared to proton-proton collisions since the deconfined matter screens the force that binds the quarkonium state [71,72]. One can imagine that the quarkonium "melts" in the quark-gluon plasma. The melting should happen sequentially, according to the binding energy of each state. Comparing the suppression of different states can thus give information about the initial temperature of the plasma.

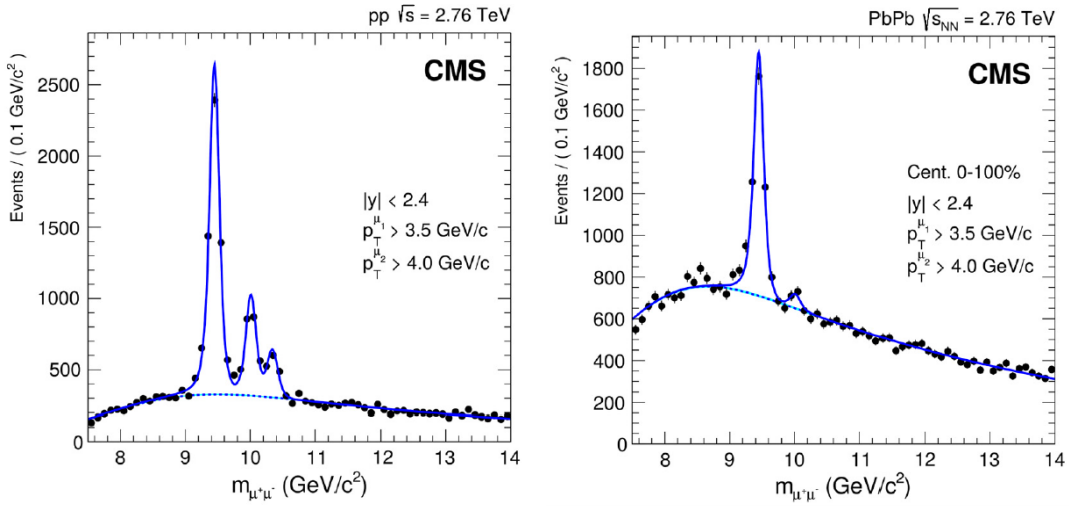

FIGURE 7 The $\mu^+\mu^-$ invariant mass distribution measured by the CMS experiment. The three peaks are from left to right the bottomonium states $\Upsilon(1S)$, $\Upsilon(2S)$ and $\Upsilon(3S)$. Figure from [73].

Recently CMS has measured the melting of different bottomonium states $\Upsilon(1S)$, $\Upsilon(2S)$ and $\Upsilon(3S)$ [73]. The di-muon invariant mass spectra from pp and Pb–Pb collisions averaged over all centralities are shown in Figure 7. The most weakly bound state $\Upsilon(3S)$ is not visible in the Pb–Pb data and the suppression factors for $\Upsilon(1S)$ and $\Upsilon(2S)$ are 2 and 8, respectively. It is also found out in this study that the suppression of these bottomonium states shows strong centrality dependence. These observations are compatible with theoretical models of sequential melting of quarkonium in quark-gluon plasma.

1.2.3 Cold nuclear matter

A crucial intermediate step in understanding the characteristics of the quark-gluon plasma is to study how does the presence of the heavy nucleus itself modify the collision process. Even if no quark-gluon plasma is formed, the studied observables can be modified as the scattering happens in the middle of a nucleus as opposed to vacuum. Possible effects coming from this source are collectively called cold nuclear matter effects and they can be studied in proton-nucleus collisions.

Traditionally proton-nucleus collisions have been consider as control measurements to better understand quark-gluon plasma, as explained above. The deuteron-gold collisions at RHIC played a crucial role in discovering the quark-gluon plasma [32–35]. More recently after observations like flow in small systems [74–76] have been made, the proton-nucleus collisions have become an interesting topic to study also on their own.

For this thesis, the relevant cold nuclear matter effects would be those that affect high-p_{T} jet production. One possible effect in this category could come from multiple scattering of partons inside the heavy nucleus [77,78]. This is expected to

lead to broadening of jets, since the scattered partons are likely to deviate from the jet axis.

Multiple scattering inside the nucleus might also lead to jet broadening via another effect. In QCD the color factor associated with gluon emission from a quark is $C_F = \frac{4}{3}$ and the color factor associated with gluon emission from a gluon is $C_A = 3$ [2]. Thus we expect gluons to interact more strongly in the matter than quarks. It is argued in [79] that when the hard scattering happens inside a nucleus, the nucleus acts like a "gluon filter", enhancing the fraction of gluon jets at high p_{T}. We know from previous studies that gluon jets are wider than quarks jets [80].

Based on the two phenomena presented above, the cold nuclear matter effects are expected to widen the measured jets in proton-nucleus collisions with respect to proton-proton collisions.

1.3 Jet fragmentation

Jets are collimated streams of hadrons that are produced in hard scattering processes in particle collisions. The origin of jets can be intuitively explained by the properties of the strong coupling. Consider a simple case where a $\mathrm{e}^-\mathrm{e}^+$ collision produces a $\mathrm{q\bar{q}}$ pair. As the colored charges move away from each other, the potential energy between them grows. At some point the potential energy grows so large, that a new $\mathrm{q\bar{q}}$ pair can be created from the vacuum. This process continues and new $\mathrm{q\bar{q}}$ pairs are created from the vacuum until their kinetic energy has degraded into colorless clusters of quarks and gluons. Energy and momentum conservation ensures that the newly created particles follow approximately the direction of the original quark and antiquark created in the scattering.

Even though the explanation above gives a nice intuitive picture of the jet fragmentation process, we cannot make quantitative predictions based on it. We need to find a more detailed description. This can be provided by perturbative QCD. After the hard scattering the energy scale is high, so perturbative approach can be used create a shower of partons. Towards the end of the parton shower process the energy scale diminishes, and the final state hadrons must be produced from the created parton cascade by some non-perturbative hadronization process.

1.3.1 Parton shower evolution

The work involved to do complete pQCD calculations increases a lot with the order, so in most cases the calculations have been performed only up to next-to-leading order. In the formation of the jet after a hard scattering the higher order terms coming from soft gluon radiation and collinear splittings are enhanced, so these cannot be neglected in the description of the event [6]. A solution to this problem is to change the approach a bit, and try to find an approximate result where such enhanced terms are taken into account to all orders. This leads to a physically appealing parton shower picture, where the complex $2 \to n$ process

is viewed as a hard $2 \to 2$ collision followed by $1 \to 2$ splittings with decreasing virtuality [81].

When the collinear splittings are taken into account in all orders, it is found out that the probability for splittings is governed by the DGLAP evolution equation [82–84]

$$\mathrm{d}\mathcal{P}_a(z,Q^2) = \frac{\mathrm{d}Q^2}{Q^2}\frac{\alpha_s}{2\pi}P_{a\to bc}(z)\mathrm{d}z \,, \tag{7}$$

which tells the differential probability that a mother parton a will branch into two daughter partons b and c at a virtuality scale Q^2 with parton b taking a fraction z of the energy of the mother a and parton c a fraction $1-z$. The splitting kernels $P_{a\to bc}(z)$ for massless quarks are

$$P_{\mathrm{q}\to\mathrm{qg}}(z) = \frac{4}{3}\frac{1+z^2}{1-z} \,, \tag{8}$$

$$P_{\mathrm{g}\to\mathrm{gg}}(z) = 3\frac{(1-z(1-z))^2}{z(1-z)} \,, \tag{9}$$

$$P_{\mathrm{g}\to\mathrm{q\bar{q}}}(z) = \frac{n_f}{2}(z^2+(1-z)^2) \,, \tag{10}$$

where n_f is the number of flavors kinematically allowed. Here it should be noted that if $Q^2 = f(z)m^2$, then for any smooth and positive function $f(z)$ it holds that $\frac{\mathrm{d}Q^2}{Q^2}\mathrm{d}z = \frac{\mathrm{d}m^2}{m^2}\mathrm{d}z$. Thus there is some freedom on how to define the evolution variable Q^2.

The DGLAP evolution equation (7) formally corresponds to emission of infinite amount of partons. Thus a cut-off scale is needed, below which the evolution is stopped and the partons are transformed into hadrons. This cut-off scale Q_0 is usually taken to be of the order of $Q_0 = 1$ GeV.

To decide which of the allowed emissions will occur first, a time ordering is introduced in the form of a Sudakov form factor [85]

$$\mathcal{P}_a^{\mathrm{no}}(Q^2_{\mathrm{max}},Q^2) = \exp\left(-\int_{Q^2}^{Q^2_{\mathrm{max}}}\int_{z_{\mathrm{min}}}^{z_{\mathrm{max}}}\mathrm{d}\mathcal{P}(z',Q'^2)\right) \,. \tag{11}$$

This factor gives the probability that no emissions occur between the initial scale Q^2_{max} and the current scale Q^2 within kinematic limits $z_{\mathrm{min}} < z < z_{\mathrm{max}}$. Combining this with the DGLAP evolution equation (7), the differential probability $\mathrm{d}\Delta_a(z,Q^2_a,Q^2_{\mathrm{max}})$ that the first branching of parton a occurs at scale Q^2_a is

$$\mathrm{d}\Delta_a(z,Q^2_a,Q^2_{\mathrm{max}}) = \mathrm{d}\mathcal{P}_a(z,Q^2_a)\mathcal{P}_a^{\mathrm{no}}(Q^2_{\mathrm{max}},Q^2_a) \,. \tag{12}$$

This branching produces partons b and c, for which the maximum virtuality scale is $Q^2_{\mathrm{max}} = Q^2_a$. These partons will again undergo splitting at scales Q^2_b and Q^2_c and so the shower builds up and continues until the cut-off scale Q_0 is reached.

Now that we have a method to evolve the shower dealing with collinear splitting enhancement, we still need to consider soft gluon enhancement and see how this affects the above picture. Consider a case where after a gluon splits into

a $q\bar{q}$ pair and afterwards one of the created quarks emits a soft gluon. This is illustrated in the leftmost diagram in Figure 8. We can estimate the time it takes to emit such a gluon from the uncertainty principle [86]. In the laboratory frame the emission time of the gluon from the quark is

$$t_{\text{emit}} \approx \frac{1}{E_{\text{q}}} \,, \tag{13}$$

where E_{q} is the energy of the quark. We can rewrite this equation using the energy of the quark in the rest frame of the quark instead, and boost the result to the laboratory frame to get the emission time. In the rest frame the energy of the quark is given by its virtuality M_{Virt} and assuming the quark is massless the Lorentz factor γ between the rest frame and the laboratory frame becomes $\gamma = \frac{E_{\text{q}}}{M_{\text{Virt}}}$. Thus we may write

$$t_{\text{emit}} \approx \frac{1}{M_{\text{Virt}}} \frac{E_{\text{q}}}{M_{\text{Virt}}} = \frac{E_{\text{q}}}{(k+p)^2} \,, \tag{14}$$

where k and p are the four-momenta of the gluon and the quark after the gluon emission. Since squared four-momentum is Lorentz invariant, we can write it open in the laboratory frame. Assuming that both end products are massless and Taylor-expanding the resulting cosine term leads to a form where we can express the gluon emission time using the opening angle θ_{kq} between the quark and the gluon

$$t_{\text{emit}} \approx \frac{1}{k\theta_{\text{kq}}^2} \,. \tag{15}$$

Using the transverse wavelength of the emitted gluon $\lambda_{\perp}^{-1} = k_{\perp} \approx k\theta_{\text{kq}}$, we can rewrite this as

$$t_{\text{emit}} \approx \frac{\lambda_{\perp}}{\theta_{\text{kq}}} \,. \tag{16}$$

In order for the gluon to be able to probe the quark produced in the earlier splitting, the transverse wavelength must be smaller than the transverse separation of the produced $q\bar{q}$ pair. The transverse separation is

$$r_{\perp}^{q\bar{q}} \approx \theta_{q\bar{q}} t_{\text{emit}} \approx \lambda_{\perp} \frac{\theta_{q\bar{q}}}{\theta_{\text{kq}}} \,. \tag{17}$$

From here we see that in order for the emission to probe the individual quark, we must have $\theta_{q\bar{q}} > \theta_{\text{kq}}$. The wide angle radiation where $\theta_{q\bar{q}} < \theta_{\text{kq}}$ cannot resolve between quark and antiquark in the system, so it probes the state of the system before the splitting. Therefore it can be treated as if it had been emitted by the splitting gluon, imagined to be on-shell. Figure 8 illustrates this color coherence effect, which leads to angular ordering of soft gluon radiation, where each successive angle must be smaller than the previous one. The effect can be calculated to all orders [6] and it turns out that to take this effect into account in the DGLAP evolution equation (7) it suffices to select the evolution variable Q^2 in such a way that it ensures angular ordering.

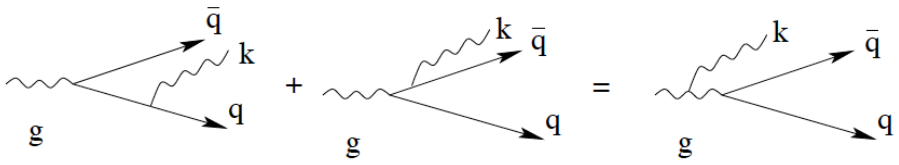

FIGURE 8 Wide angle soft gluon k emission off q or $\bar{q}$ acts as if it came off the parent gluon g, imagined to be on-shell. Figure from [86].

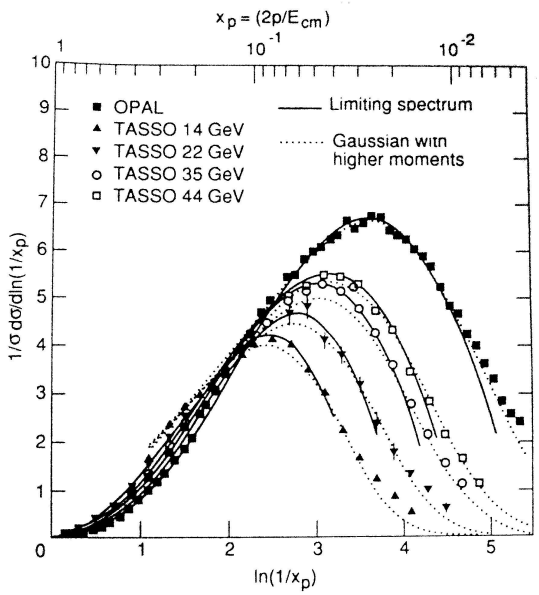

FIGURE 9 The measured $\ln\left(\frac{1}{x_p}\right)$ distributions of charged particles in $e^+e^- \to$ hadrons process from OPAL [87] and TASSO [88] collaborations compared to pQCD predictions. Figure from [86].

Experimentally the angular ordering is visible, for example, in the momentum distribution of charged particles in the $e^+e^- \to$ hadrons process. The requirement for successively decreasing angles reduces the available phase space. This leads to a slower rise in gluon multiplicity within a parton jet and changes the shape of the gluon momentum distribution compared to an incoherent case [87]. When the momentum is probed with the help of the variable $\ln\left(\frac{1}{x_p}\right)$, where $x_p = \frac{2p}{E_{\mathrm{CM}}}$, the pQCD calculation taking into account color coherence effects gives a nearly Gaussian distribution. The pQCD calculations are compared to experimental results from OPAL [87] and TASSO [88] in Figure 9. The black lines denoted "Limiting spectrum" are the pQCD predictions and they can be seen to follow the experimental data nicely, giving evidence that the color coherence phenomena are important in jet fragmentation. In this pQCD calculation the resulting partons were transformed into final state hadrons using the local parton-hadron duality hypothesis, which will be introduced in the next section.

1.3.2 Hadronization

After the parton shower reaches a scale close to Λ_{QCD}, the perturbative description is not valid anymore and the final state particles must be produced in some non-perturbative manner. One simple scenario that is used in several theory calculations is the so-called local parton-hadron duality [89]. In the local parton-hadron duality hypothesis it is assumed that there exists a low virtuality scale Q_0 in which the hadronization happens, that is independent of the scale of the primary hard process. At this scale the partons are transformed into hadrons, assuming that the flow of momentum and quantum numbers for the hadrons can be directly obtained from those of partons introducing only small normalizing constants.

In general the hadronization is assumed to be universal, meaning that it does not depend on the colliding system or the collision energy. This is due to the fact that as explained above, the hadronization is expected to happen in a low virtuality scale Q_0, regardless on how this scale is reached. More advanced hadronization scenarios used by PYTHIA and Herwig events generators are presented in the next section together with these generators.

1.3.3 Experimental techniques

There are two main experimental approaches to study jets, jet reconstruction and multi-particle correlations. In the jet reconstruction the idea is to cluster particles together as jets in each event. The goal is to obtain a reasonable representation of the initial parton kinematics [9]. A set of rules that relates the observed particles into jets is called a jet algorithm. There are many jet algorithms on the market, such as k_{T} [90, 91], Cambridge/Aachen [92] and anti-k_{T} [93] jet algorithms. As these will not be used in this thesis, I will give no more details here and just leave the references for interested readers.

The second option is to do the jet analysis based on particle correlations. Here a high-p_{T} trigger particle can be taken to approximate the jet and jet properties can be obtained statistically by correlating the other particles in the event with the trigger particle. The chosen approach in this thesis is to study jets via two-particle correlations. A more detailed introduction to this method will be given in the beginning of Chapter 4.

The main reason why two-particle correlations are chosen as the analysis technique is that the correlations are expected to be more sensitive to the soft and non-perturbative phases of the jet fragmentation than full jet reconstruction [9]. The reason for this is that a jet given by the jet reconstruction algorithm is designed to give a reasonable description of the initial parton kinematics. Clustering particles together to form a jet suppresses the physics close to the Λ_{QCD} scale to achieve this. Thus the correlations can give a better handle to study the parton shower and hadronization phases of the jet fragmentation separately. The correlations can also be more sensitive to medium modifications, like cold nuclear matter effects.

1.4 Monte Carlo implementations of jet fragmentation

Understanding the final state in a high energy particle collision is a very difficult theoretical problem. There can be hundreds of particles produced in the collisions whose momenta can span over a large range. These particles can involve all the standard modal species and maybe even some beyond the Standard Model. The hard processes can be calculated in the perturbation theory, but the calculations become very laborious beyond the few lowest orders. On top of this, the partons are transformed into hadrons in an intrinsically non-perturbative hadronization process that cannot be, at the moment, calculated from the first principles. To take all this into account and to produce predictions that can be compared to the experiments, Monte Carlo event generators are developed [94]. The event generators take an advantage of the pQCD factorization theorem [95], which guarantees that different stages of collision can be treated separately. This allows to systematically improve the description of initial state radiation, final state radiation and hadronization. Monte Carlo techniques are used to solve the pQCD matrix elements and to produce the final state of particles. As the output is a final state of particles, this can be easily compared with experiments.

In the following subsections two Monte Carlo event generators, PYTHIA and Herwig, are presented. We focus on the way they deal with the jet fragmentation process, since this is the relevant part for this thesis.

1.4.1 PYTHIA

PYTHIA [96–101] is a Monte Carlo event generator developed at the Lund University in Sweden. The development of JETSET [102–105], another event generator developed at Lund, began in 1978. JETSET later merged with PYTHIA and the development of PYTHIA still continues, so the current version has seen almost 40 years of development and is the most widely used event generator by the high energy physics community. The PYTHIA versions used in this thesis are the two most recent versions PYTHIA 8.1 [10] and PYTHIA 8.2 [11]. The two versions are very similar, and will be commonly denoted PYTHIA 8.

To simulate the evolution of the event after the hard scattering, PYTHIA 8 uses the shower approach presented in Section 1.3.1. In the PYTHIA 8 shower algorithm, the evolution scale Q^2 in the DGLAP equation (7) is probed using the transverse momentum $p_\perp$ of the splitting daughters with respect to the momentum of the mother particle [81]. This is illustrated in the right side of Figure 10. Choosing the evolution variable this way ensures that the hardest interaction, which is the most important for the experimental consequences, happens first. The regular measured parton densities can then be used for this first scattering and the possible correlation effects only show in the later lower p_T scatterings.

To see that this definition is of the allowed form, take a look at the situation in the light cone coordinates, defined as $\mathbf{p} = (p^+, p^-, p_\perp)$, where $p^\pm = E \pm p_z$. Using the relation $p^+p^- = E^2 - p_z^2 = m^2 + p^2 - p_z^2 = m^2 + p_\perp^2$ and defining for $a \to bc$

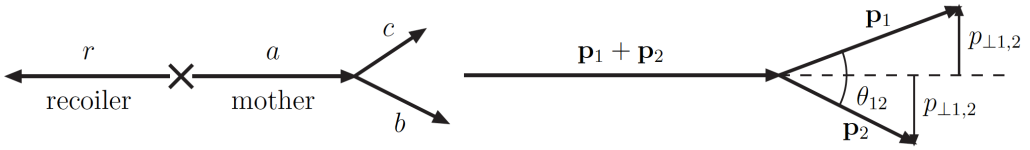

FIGURE 10 *Left:* Illustration of one splitting. The x in the figure represents the hard scattering vertex. *Right:* Definition of $p_\perp$ in the PYTHIA 8 shower algorithm. Figure from [81].

splitting that $p_a^+ = zp_b^+$ and $p_a^+ = (1-z)p_c^+$, it follows from the conservation of p^- that

$$m_a^2 = \frac{m_b^2 + p_\perp^2}{z} + \frac{m_c^2 + p_\perp^2}{1-z} \,. \tag{18}$$

This can be rewritten for $p_\perp$ as

$$p_\perp^2 = z(1-z)m_a^2 - (1-z)m_b^2 - zm_c^2 \,. \tag{19}$$

The final state shower in modeled as a timelike shower, meaning that a virtual parton splits into two on-shell partons. As the partons are massless in the model, it follows that $m_a^2 = Q^2$ and $m_b^2 = m_c^2 = 0$. Thus the $p_\perp^2$ used to evolve the system becomes

$$p_{\perp\,\mathrm{evol}}^2 = z(1-z)Q^2 \,. \tag{20}$$

We see that this definition fulfills the requirement $Q^2 = f(z)m^2$ as $p_{\perp\,\mathrm{evol}}^2 = z(1-z)m_a^2$ and is thus of the allowed form for the DGLAP evolution equation.

With this information, we can understand the main points of the PYTHIA 8 showering algorithm. The steps in the algorithm are [81]

1. Define the evolution variable: $p_{\perp\,\mathrm{evol}}^2 = z(1-z)Q^2$.
2. Evolve all partons that may branch downwards in $p_{\perp\,\mathrm{evol}}^2$ according to equation (12). This defines all the branching that may happen next.
3. Choose the branching with the highest $p_{\perp\,\mathrm{evol}}^2$ as the next actual branching.
4. Derive the virtuality from the picked up $p_{\perp\,\mathrm{evol}}^2$ and z values and construct the kinematics based on this. All the partons that have not branched yet are assumed to be on a mass shell. Define a recoiler for the branching parton in order to conserve energy and momentum in the splitting. For a branching of q or $\bar{\mathrm{q}}$ in a simple $\mathrm{q}\bar{\mathrm{q}}$ system the recoiler is the other half of this dipole, as illustrated in Figure 10. In a more complex system the exact definition of the recoiler can be more complicated. The energy and momentum of the recoiler are adjusted when a virtuality is assigned for the branching parton so that overall energy and momentum are conserved in the system.
5. Iterate towards lower values of $p_{\perp\,\mathrm{evol}}^2$ until no further branchings occur above the cutoff scale $p_{\perp\,\mathrm{min}}^2$.

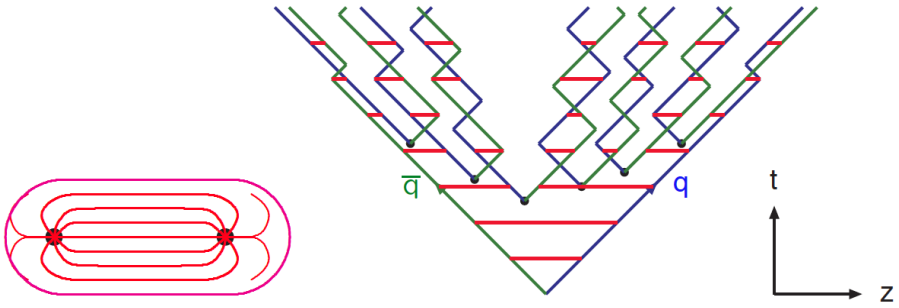

FIGURE 11 *Left:* A flux tube between a quark and an antiquark. *Right:* Illustration of the string breaking. The blue lines are quarks, green lines antiquarks and red lines illustrate the string field. Figure from [94].

One might think that there is a problem with soft gluon radiation in this approach, since the evolution variable $p_{\perp\,\mathrm{evol}}$ does not seem to guarantee angular ordering, as was required in Section 1.3.1. However, it turns out that when the shower is defined using the radiator-recoiler dipole approach, transverse momentum ordered showers are formally as accurate in describing the soft gluon emissions as the angular ordered showers [94].

After the parton cascade is generated by the showering algorithm, the generated partons must hadronize to produce the final state particles. For the hadronization a Lund string fragmentation algorithm [106] is used by PYTHIA 8. The string model is based on the fact that in QCD linear confinement is expected over large distances [94]. One can model this by imagining a color flux tube beings stretched between the outgoing partons. The left side of Figure 11 illustrates this point for a $q\bar{q}$-pair. The tube is assumed to have a uniform fixed transverse size of about 1 fm along its length, which leads to a linearly rising potential $V(r) = \kappa r$. The string constant κ describes the amount of energy per unit length and from the hadron mass spectroscopy a value of $\kappa \approx 1$ GeV/fm ≈ 0.2 GeV^2 is obtained.

The evolution of string fragmentation is illustrated schematically on the right side of Figure 11. This figure is drawn in a light cone presentation, so the initial quark and antiquark are going to separate directions at the speed of light. The string between them, illustrated in the figure by red line, stretches until its potential energy becomes high enough that it can break forming a new quark-antiquark pair. If the original pair was $q\bar{q}$ and the new pair $q'\bar{q}'$, now two new pairs $q\bar{q}'$ and $q'\bar{q}$ are formed. As these particles are also moving away from each other, the strings between them can stretch and break and yet new pairs form. The process continues until the invariant mass of the system connected by the string becomes small enough, in which case a final state meson is formed.

Mathematically the string connecting a quark and an antiquark is modeled by a massless relativistic string with no transverse degrees of freedom. The gluons are represented as energy and momentum carrying kinks on the string with an incoherent sum of one color charge and one anticolor charge. When such a string breaks, it classically required that the created quark and antiquark are produced at

a certain distance if they are to have any mass or transverse momentum. However, quantum mechanically the quark-antiquark pair must be created at one point and then tunnel out to the classically allowed region. Thus the probability to create a new quark-antiquark pair becomes proportional to the tunneling probability [106]

$$P_{\text{tunneling}} \propto \exp\left(\frac{-\pi m_\perp^2}{\kappa}\right) = \exp\left(\frac{-\pi m^2}{\kappa}\right) \exp\left(\frac{-\pi p_\perp^2}{\kappa}\right) . \tag{21}$$

In the above equation the transverse mass $m_\perp$ is defined as $m_\perp^2 = m^2 + p_\perp^2$. The transverse momentum here is defined to be transverse to the string axis. This probability formula leads to flavor-independent Gaussian $p_\perp$-distribution for the created $q\bar{q}$ pairs.

As explained above, the string fragmentation would only produce mesons in the final state. However, we know that also baryons exist in the nature. The baryon production is included in the string fragmentation model by adding some probability that when a string breaks, a diquark-antidiquark pair is created instead of a quark-antiquark pair.

The kinematics of each string break are determined iteratively. Since there is no natural ordering, the string breakings can be considered in any order and the same answer must be obtained. We can, for example, start from the q leg and work our way to the $\bar{q}$ leg, or vice versa. This leads to a left-right symmetry of the string fragmentation. In PYTHIA this is taken into account by defining the Lund symmetric fragmentation function [106]

$$f(z) \propto \frac{1}{z}(1-z)^a \exp\left(-\frac{bm_\perp^2}{z}\right) \tag{22}$$

to break the string into a hadron and a remainder system. In this function z is the fraction of light-cone momentum p^+ given to the hadron in the string breaking, $m_\perp$ is the transverse mass of the hadron and a and b are tunable parameters of the model. The process can be thought as follows: first start from the q-leg of a $q\bar{q}$ system and choose the consider the breaking to new $q'\bar{q}'$ pair closest to this leg. Now the breaking will produce a hadron $q\bar{q}'$ and a remainder system spanning from q' to $\bar{q}$. Then the process is continued until the $\bar{q}$-leg is reached. A small detail here is that in equation (22) it is assumed that the mass of the remainder system is large. Thus some patching up is needed for the last two hadrons coming from a string. The patching up is done such that the place where it happens looks as closely like any other string break as possible.

There is also a possibility that a string has so low mass that it cannot break at all. In this case a single hadron is generated out of it shuffling some energy and momentum with other partons in the event if necessary.

After all the hadrons are produced, the short-lived ones can still decay before the set of final state particles in the simulation process is obtained. [81, 94, 106]

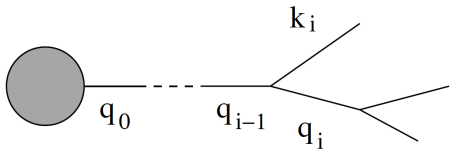

FIGURE 12 A schematic figure about final state parton branching. The blob represents the hard process. Figure from [108].

1.4.2 Herwig

Herwig (Hadron Emission Reactions With Interfering Gluons) is another long developed and widely used event generator. It was first published on 1986 [107] and has been developed ever since. The most recent version and the one that is used in this thesis is Herwig 7 [12, 13].

In Herwig 7, the parton shower is evolved according to DGLAP evolution equation (7) as in PYTHIA 8. What is different is the choice of the evolution variable Q^2, which for Herwig is denoted as $Q^2 \equiv \tilde{q}^2$. To be able to define this variable, we first need to look how the shower evolution can be described in the Sudakov basis [108]. Using the notation as in Figure 12, the quark four-momentum after the ith gluon emission $q_{1-i} \to q_i + k_i$ in Sudakov basis is defined as

$$q_i = \alpha_i p + \beta_i n + q_{\perp i} \,, \tag{23}$$

where p is the four-momentum of the parton initiating the shower (labeled q_0 in Figure 12) assuming that $p^2 = m^2$, n is defined such that $\vec{n} = -\vec{p}$ holds for three-momenta and $n^2 = 0$ and $q_\perp$ is the transverse momentum with respect to original parton momentum $\vec{p}$. Using this notation, the momentum fraction given to next stage in splitting is defined as

$$z_i = \frac{\alpha_i}{\alpha_{i-1}} \tag{24}$$

and the relative transverse momentum as

$$p_{\perp i} = q_{\perp i} - z_i q_{\perp i-1} \,. \tag{25}$$

Now that we have defined the Sudakov basis, we can look at the evolution variable $\tilde{q}$ in Herwig. For the splitting $i-1 \to i+j$ where the daughters i and j are assumed to be on-shell this becomes

$$z(1-z)\tilde{q}^2 = -m_{i-1}^2 + \frac{m_i^2}{z} + \frac{m_j^2}{1-z} - \frac{p_\perp^2}{z(1-z)} \,. \tag{26}$$

The evolution variable is chosen like this to ensure that the angular ordering required by QCD color coherence in explicitly obeyed. This point is not completely clear of the form of equation (26), but this formula can be rewritten as [12]

$$\tilde{q}^2 = \frac{2E_{i-1}^2(1-\cos\theta_{ij})(1+\cos\theta_{i-1})^2}{(1+\cos\theta_i)(1+\cos\theta_j)} \,, \tag{27}$$

where the angle θ_{ij} is the angle between partons i and j and θ_{i-1}, θ_i and θ_j are the angles between partons $i-1$,i,j and the initial parton momentum $\vec{p}$. For small angles this becomes

$$\tilde{q} = E_{i-1}\theta_{ij}(1 - \mathcal{O}(\theta_x^2)) \ . \tag{28}$$

When a branching occurs, the daughter partons i and j, with momentum fractions z and $1-z$, have their starting evolution scales set to $z\tilde{q}$ and $(1-z)\tilde{q}$, respectively. As z gives also approximately the energy fraction taken by the daughter, we may write $z\tilde{q} \approx E_i\theta_{ij}$ and $(1-z)\tilde{q} \approx E_j\theta_{ij}$. The next branchings must happen at lower scales than the previous ones. From this it follows that the next opening angles are smaller than θ_{ij} and angular ordering is fulfilled.

A slight drawback in this approach is that is leaves a dead region in the phase space [94], where too little emission is produced. This is filled by either a hard matrix element correction or by higher order emissions.

Similarly as previously in PYTHIA, the DGLAP evolution continues to produce new partons until a cutoff scale Q_0 is reached. After that the produced parton cascade needs to hadronize. In Herwig, the hadronization is handled by a cluster model [12]. This model is based on the preconfinement property of parton showers [109]. Preconfinement means that the color structure of the shower at any evolution scale Q_0 is such that color singlet combinations of partons can be formed with an asymptotically universal invariant mass distribution. Universal here means that the invariant mass does not depend on the initial hard process scale Q, but only on Q_0 and the QCD scale Λ_{QCD}. Asymptotic means that $Q \gg Q_0$.

The first step in the Herwig hadronization algorithm is that all the gluons are non-perturbatively transformed into $\mathrm{q\bar{q}}$ pairs. This requires a mass to be assigned to the gluons, which must be at least twice the lightest quark mass. After the gluons are transformed to quarks, the adjacent color lines can be clustered together to color singlet states with mesonic quantum numbers. The momentum of these clusters is defined to be the sum of the momenta of the clustering partons. According to preconfinement, the mass distribution of these clusters is independent of the details of the hard scattering process. As it is also peaked at low masses, the clusters can be regarded as highly excited hadron resonances and decayed into the final state hadrons.

After the initial clusters have been formed, some of them are too heavy to reasonably describe an excited state of a hadron. These clusters have to be split before they are allowed to decay. The cluster C is split if its mass fulfills the condition [12]

$$M_C^p \geq M_{\mathrm{max}}^p + (m_1 + m_2)^p \ , \tag{29}$$

where $m_{1,2}$ are the masses of the constituent partons of the cluster and M_{max} and p are the main parameters of the model. The parameters M_{max} and p are chosen separately for clusters containing light, charmed and bottom quarks. When a cluster is split, a pair of light quarks is generated from the vacuum and two new clusters are made both containing of one quark from the original cluster and one from the newly generated pair. The splitting is continued until no clusters with a mass M_C fulfilling the equation (29) remains.

When all the clusters are light enough, they decay into final state hadrons. If the mass of the cluster is sufficiently high that in can decay into a baryon-antibaryon pair, first there is a parameter deciding whether the cluster undergoes mesonic or baryonic decay. For a mesonic decay a quark-antiquark pair is created from the vacuum and for the baryonic decay a diquark-antidiquark pair is made. Then the exact decay products are chosen and the cluster decayed isotropically in the rest frame of the cluster. If there are partons produced in the perturtabive phase involved in the decay, they retain their original direction in the cluster rest frame, up to some Gaussian smearing. If the cluster mass is too low to decay into a pair of mesons, is it decayed into the lightest possible hadron and some energy and momentum is reshuffled with the adjacent clusters. Now we are left with the final state hadrons, some of which might still decay until the end of the simulation if they are very short-lived. [12, 94, 108]

2 EXPERIMENTAL DETAILS

2.1 CERN

The European Organization for Nuclear Research (CERN) is the biggest particle physics laboratory in the world. The laboratory was founded on 1954 and is located near Geneva in the borderlands of France and Switzerland. Nowadays CERN consists of 22 member states and a number of other countries and institutions associated with CERN in some other ways. CERN itself employs around 2500 people and in addition to that some 12000 visiting scientists from over 600 institutions in over 70 countries come to CERN for their research.

The research made at CERN is based around it's accelerators. A schematic view of the CERN's accelerator complex is presented in Figure 13. The main focus of the research today is in particle collisions provided by the biggest accelerator in this figure, the Large Hadron Collider LHC. However, there is active and interesting research being done also with the smaller accelerators. The beam from the second largest accelerator, called the super proton synchrotron SPS, is used by various diverse experiments. The fixed target experiments COMPASS, NA61/SHINE, NA62 and NA63 use it to study structure (COMPASS) and properties (NA61/SHINE) of hadrons, rare decays of kaons (NA62) and radiation processes in strong electromagnetic fields (NA63). Also accelerator research and development is conducted with the help of SPS. The AWAKE experiment uses the SPS beam to explore the use of plasma to accelerate particles and the UA9 experiment to investigate how crystals could help to steer particle beams.

Going down in the size of the accelerators, after SPS the third largest accelerator in CERN is the proton synchrotron PS. The DIRAC experiment uses the beam from PS to gain insight into the strong force. A somewhat different experiment is the CLOUD experiment, which studies the effect of cosmic rays to cloud formation using controlled particle beams from PS. A third experiment using the PS beam is nTOF, which studies neutron-nucleus interactions.

Antimatter is studied at CERN using the antiproton decelerator AD. AD uses the beam from PS and a block of metal to generate antiprotons, which it then

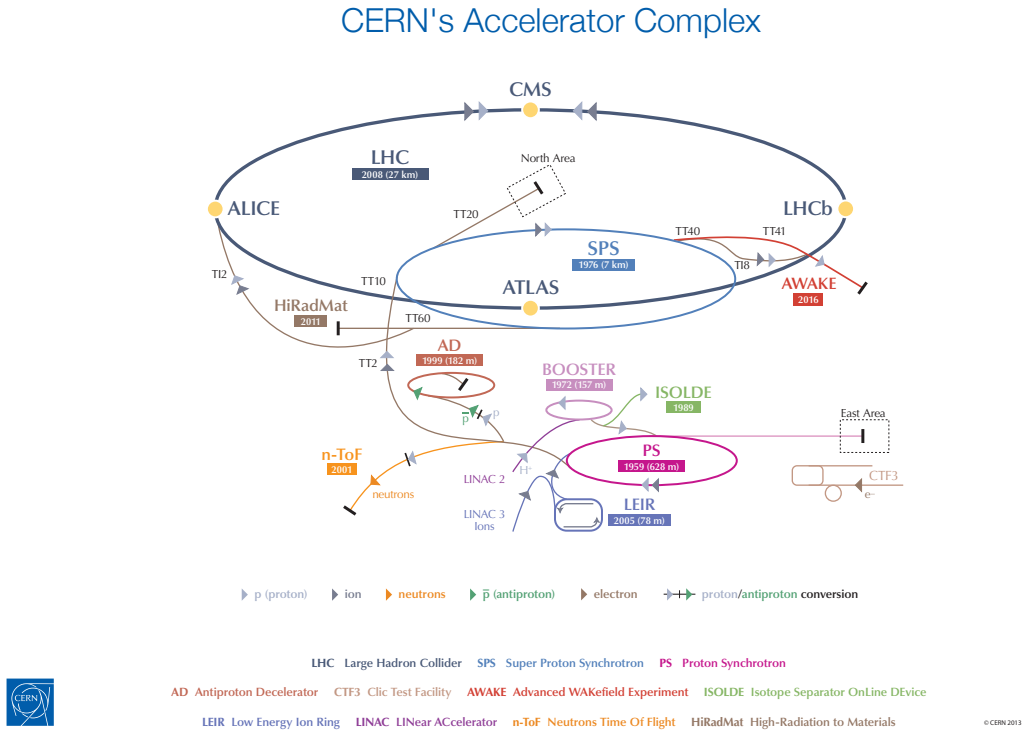

FIGURE 13 Schematic picture of CERN's accelerator complex. Before the particles arrive to LHC to get the final kick in their momentum, they go through linear accelerator (LINAC2), Booster, Proton Synchrotron (PS) ans Super Proton Synchrotron (SPS). Figure from CERN-Poster-2013-377.

tries to decelerate into a usuful, low-energy beam. AEGIS, ALPHA, ASACUSA, ATRAP, and BASE experiments use the antiprotons provided by AD to study the properties of antimatter.

The beam from BOOSTER accelerator is used for a nuclear physics program in the ISOLDE experiment. By directing this beam into specially developed, thick targets, low energy beams of radioactive nuclides can be obtained. This permits to study the properties of atomic nuclei, including the most exotic species.

There are also a few experiments decoupled from the beam facilities. CAST and OSQAR experiments are built from pieces of LHC magnets to study hypothetical particles called axions, which could explain the differences between matter and anti-matter. The AMS detector at the international space station was also assembled at CERN. This spectrometer tries to find dark matter, antimatter and missing matter.

More information about the various CERN experiments can be found online from [110].

2.2 Large Hadron Collider

The Large Hadron Collider is the largest particle collider ever built by the mankind. With a circumference of 26.7 km, the LHC is designed to accelerate the proton beams up to the energy of 7 TeV and lead beams up to 2.76 TeV per nucleon [111]. The highest energy achieved by proton beams at the time of writing of this thesis has been 6.5 TeV. The design luminosity of the machine is 10^{34} $\mathrm{cm}^{-2}\mathrm{s}^{-1}$ for proton beams and 10^{27} $\mathrm{cm}^{-2}\mathrm{s}^{-1}$ for lead beams. The current record for peak luminosity for proton beams is approximately $1.75 \cdot 10^{34}$ $\mathrm{cm}^{-2}\mathrm{s}^{-1}$ from June 2017 and for lead beams approximately $2 \cdot 10^{27}$ $\mathrm{cm}^{-2}\mathrm{s}^{-1}$ from December 2015 [112], meaning LHC has already exceeded the design luminosities.

It is technically difficult to accelerate a beam from zero energy into LHC energy of 7 TeV. Thus the particles that are injected to the LHC have to be pre-accelerated by other machines. The feeding chain is illustrated in Figure 13. For protons, the chain starts from a bottle of hydrogen next to the linear accelerator LINAC2. This linear accelerator accelerates the protons up to the energy of 50 MeV and after that the protons are transferred into the PS Booster. With booster an energy of 1.4 GeV is achieved and the protons are given for PS for further acceleration. PS pushes the energy up to 25 GeV and leaves the next kick for SPS, which can achieve an energy of 450 GeV. This the injection energy for the LHC, which takes care of the final boost until 7 TeV. For ions, the acceleration chain is slightly different. Ions are first acceleratod with the linear accelerator LINAC3, after which they go to the low energy ion ring (LEIR). From LEIR the ion go to PS and from there on follow the same path as protons.

The acceleration of the particles is done using radio-frequency (RF) cavities. The RF cavities are built in a way, that the electromagnetic waves become resonant and build up inside the cavity. The passing charged particles feel the overall force and are pushed forward along the accelerator. The field in the RF cavities is made to oscillate. This means that the particles must be inserted to the cavity at the correct phase of oscillation. When timed correctly, the particles will feel zero accelerating voltage when they have exactly the correct energy. Particles with higher energies are decelerated and particles with lower energies are accelerated. This focuses the particles in a distinct bunches, which can contain up to $1.15 \cdot 10^{11}$ particles in the LHC. The RF oscillation frequency is LHC is 400.8 MHz and the bunch frequency 40 MHz. This bunch frequency means that different bunches are 25 ns apart from each other in the accelerator.

To keep a beam with the LHC energy in a circular orbit, strong dipole magnets are needed. In the LHC there are 1232 dipole magnets that need to produce a magnetic field of 8.33 T for 7 TeV proton beams. The magnets must be superconducting to achieve such a high field. This requires them to be cooled down to the temperature of 1.9 K. This is achieved by liquid helium cooling system. Together with the dipole magnets, also quadrupole magnets are needed to keep the beam focused inside the beam pipe. 392 quadrupole magnets are placed along the ring to achieve this. In addition to these, some higher multipole magnets

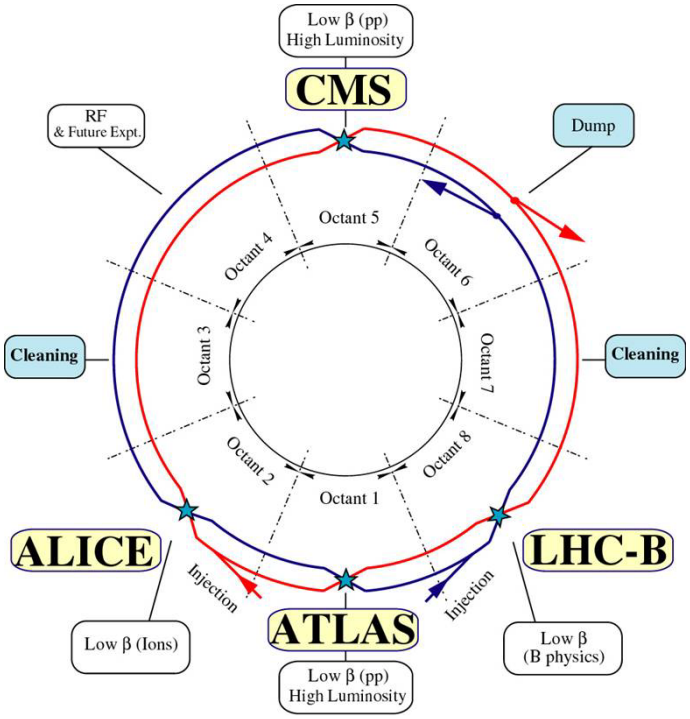

FIGURE 14 Division of LHC into octants. Figure from [111].

are used for smaller corrections. The number of bending and focusing magnets totals at about 10000.

The LHC construction is divided into octants, where each octant has a different function. A schematic view of this division is presented in Figure 14. The beams are injected to the machine from octants 2 and 8. They are crossed in octants 1, 2, 5 and 8 and the experiments are build around these interaction points. The rest of the octants do not have beam crossings. Octants 3 and 7 have collimators, that are used for beam cleaning. With these collimators particles with too high momentum or position offsets are scattered off from the beam. The RF cavities used for accelerating the beam are located at octant 4. The beam dump is found from octant 4. At the beam dump facility, each beam has its own iron septum magnet that can kick the beam away from machine components into an absorber.

2.2.1 Heavy ion experiment: ALICE

ALICE (A Large Ion Collider Experiment) [113] is the dedicated heavy ion experiment at the LHC. It is specialized in functioning well in the high multiplicity environment of heavy ion collisions. Among the most important results published by the ALICE experiment are the measurements of elliptic flow [114] and suppression of charged particles [60] in $\sqrt{s_{\mathrm{NN}}} = 2.76\,\mathrm{TeV}$ Pb–Pb collisions. These are both indications of a strongly interacting phase of matter, the quark-gluon plasma. A detailed description of the ALICE experiment is given in Section 2.3.

2.2.2 Multipurpose experiments: ATLAS and CMS

ATLAS (A Toroidal LHC ApparatuS) [115] and CMS (Compact Muon Solenoid) [116] are the two big multipurpose experiments at the LHC. They are designed to be sensitive to many different possible new physics signals, including extra dimensions and supersymmetric particles. The biggest discovery so far made by these two experiments is the discovery of the Standard Model Higgs boson, which both of the experiments published in 2012 [117, 118].

2.2.3 Matter-antimatter asymmetry: LHCb

The LHCb (LHC beauty) experiment [119] specializes in the physics of bottom quark. The main physics goal is to measure the parameters of CP violation using decays of hadrons containing the bottom quark. One of the most important results published by LHCb is the first measurement of $B_s^0 \to \mu^+\mu^-$ decay [120]. This decay channel is a powerful probe for deviation from the Standard Model, especially in the non-standard Higgs section. However, the branching ratios of the decay are found to be in line with the Standard Model.

2.2.4 Smaller experiments: LHCf, TOTEM and MoEDAL

Together with the four big experiments, there are also three smaller experiments scattared along the LHC ring, LHCf (LHC forward) [121], TOTEM (TOTal Elastic and diffractive cross section Measurement) [122] and MoEDAL (Monopole and Exotics Detector At the LHC) [123]. LHCf is located at the interaction point 1 together with ATLAS and it aims to simulate cosmic rays by the particles thrown forwards by the collisions in the LHC. TOTEM can be found from interaction point 5 together with CMS and it studies the protons as they emerge from collisions to small angles. The main goal is to measure the total, elastic and inelastic cross-sections in pp collisions [124]. The MoEDAL experiment is located at the interaction point 8 with the LHCb experiment, and tries to measure direct signatures of hypothetical particles with magnetic charge, magnetic monopoles.

2.3 ALICE

As a designated heavy ion experiment at the LHC, ALICE has been designed to perform in the high multiplicity environment of heavy ion collisions [113]. The different detector subsystems are optimized to provide high momentum resolution and excellent particle identification capabilities over a broad range of momentum. Thorough study of hadrons, electrons, muons and photons is possible with this setup.

A schematic figure of the ALICE detector is presented in Figure 15. The positioning of the detectors inside the ALICE experiment follows the layered onion-like scheme as is adopted by all the major high energy physics experiments. Closest

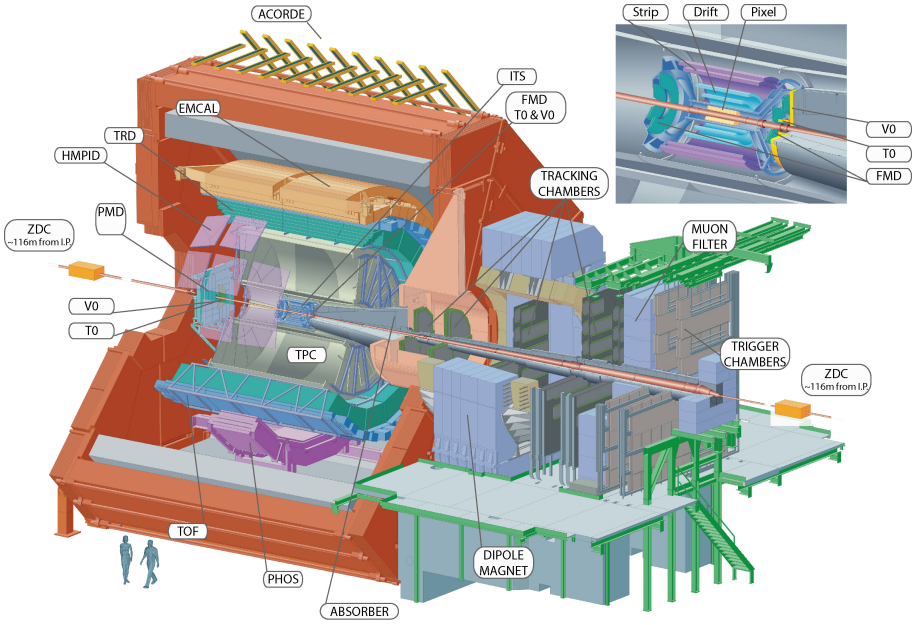

FIGURE 15 The ALICE experiment during run 1. After run 1, DCal and AD have been installed. Figure from [125].

to the interaction point are the tracking detectors. The main task of these detectors is to locate accurately the position of the primary interaction vertex and to record the tracks of charged particles. This information is complemented by particle identification detectors, which provide additional information needed to identify the particle species. These detectors can be in the innermost layers, as they do not significantly affect traversing particles. Calorimeters, on the other hand, must be placed after these detectors. Calorimeters measure the energy of the particles by absorbing the particles. Inside the magnet ALICE has only electromagnetic calorimetry, specialized in measuring electrons and photons. Outside the magnet is the muon detection system. Muons are charged particles, so they can be detected by their electric charge. In ALICE an absorber made of carbon and concrete is placed between the muon detection system and the interaction point to reduce the hadronic background in the muon measurement.

2.3.1 Tracking detectors

The design of the tracking detectors in the ALICE experiment is driven by the requirement to have a high granularity and good two track separation in the high multiplicity environment of heavy ion collisions. The particle density was expected to be as high as 8000 changed particles per unit of rapidity [113]. The actual particle density turned out to be significantly smaller than this as a value of $\mathrm{d}N/\mathrm{d}\eta \approx 1600$ was measured [126]. To best accommodate these requirements, the choice for the main tracking detector was a time projection chamber (TPC) [127]. TPC is a cylindrical detector filled with 90 m^3 of $\mathrm{Ne/CO_2/N_2}$ (90/10/5) gas mixture. When charged particles traverse the gas, they ionize it. The gas is contained in a field cage, which provides a voltage gradient of about 400 V/cm

throughout the detector. For this, a high voltage of 100 kV is needed in the central electrode. With this voltage gradient, the maximum drift time of the electrons knocked out of the ionized particles is about 90 µs. When the electrons hit the end plates of the TPC, they are measured using multi-wire proportional chambers. This design gives TPC capability to provide three dimensional tracking information, which means that several tracking points are obtained for each track.

The relatively slow drift time of 90 µs is the limiting factor for the luminosity ALICE can take. To keep the occupancy of the TPC in a manageable level, the luminosity in the ALICE is leveled by separating the beams before they collide. This decreases the recorded luminosity significantly, for example, for the $\sqrt{s} = 13\,\text{TeV}$ pp run in 2017 the peak instantaneous luminosity for ALICE was approximately four orders of magnitude smaller than for CMS and ATLAS [112]. Even though the same bunch pile-up is not significant due to the separation of beams, many bunch crossings take place during the drift time, which may result in several different events whose tracks are detected together with the triggered event. Tracks from these pile-up events can be eliminated because they are pointing into a wrong vertex.

Taking into account the maximum particle density, the minimum possible inner radius of TPC is $r_{\text{in}} \approx 85$ cm. Below this radius the hit density would be too high for precision measurements. The outer radius ($r_{\text{out}} \approx 250$ cm) is determined by the requirement that the ionization energy loss ($\mathrm{d}E/\mathrm{d}x$) resolution needs to be better than 7 %.

Between TPC and the beam pipe there is an array of six layers of silicon detectors, called the inner tracking system (ITS) [128]. Their layout is presented in Figure 16. The main tasks of the ITS are to locate the primary vertex with a resolution better than 100 µm, to reconstruct the secondary vertices from decaying particles, to track and identify particles with momentum below 200 MeV, and to improve the momentum and angle measurements of TPC. The two innermost layers of the ITS are called the silicon pixel detector (SPD), which is the fundamental element in vertex reconstruction. The choice to use pixels in the innermost layers comes from the fact that around 50 particles per cm^2 are expected in central heavy ion collisions. Small enough pixels can provide the required resolution in this particle density.

The next two layers are the silicon drift detector (SDD). This detector has very good multitrack capability and it provides two out of the four $\mathrm{d}E/\mathrm{d}x$ samples in the ITS. The particle density in SDD is still expected to be roughly 7 cm^{-2}, which requires a two-dimensional detector. The SDD is made out of homogeneous neutron transmutation doped silicon. When a charged particle goes through this material, it ionizes it. The generated charge then drifts to the collection anodes, where it is measured. The maximum drift time in SDD is about 5 µs.

The two remaining layers in the ITS are the silicon strip detector (SSD). The SSD is crucial for matching the tracks from the TPC to the ITS. SSD also provides a two dimensional track position measurement and $\mathrm{d}E/\mathrm{d}x$ information. The silicon strips work in a similar way as pixels. When a charged particle hits a grid of strips, it produces an electric charge in two intervening ones. The position of the hit can be then deduced from the place where these strips cross each other.

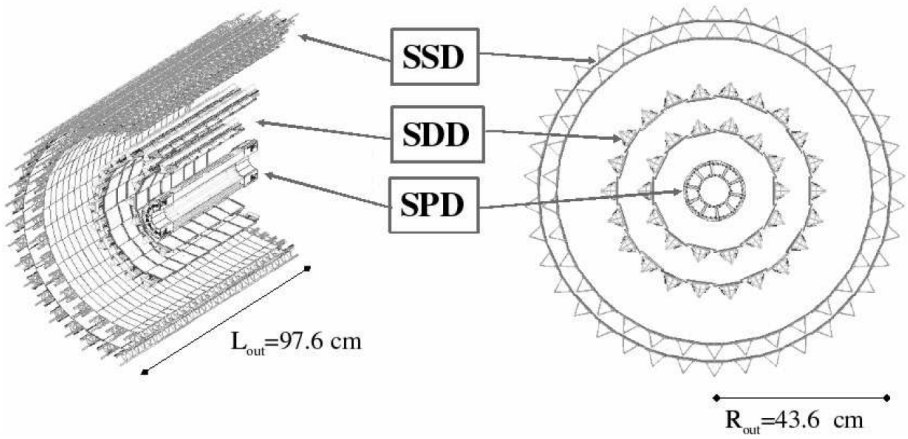

FIGURE 16 Layout of the inner tracking system. Figure from [113].

2.3.2 Particle identification detectors

An important design feature of ALICE is to have good particle identification over a large part of phase space and for several different particles. One of the particle identification detectors inside the central barrel is the transition radiation detector (TRD) [129], whose main task is to identify electrons with momentum larger than 1 GeV. Transition radiation is produced when highly relativistic particle traverses the boundary between two media having different dielectric constants. The average energy of the emitted photon is approximately proportional to the Lorentz factor γ of the particle, which provides an excellent way to discriminate between electrons and pions. In TRD the transition radiation is produced with a composite layer of foam and fibres. The emitted photons are then measured in six layers of Xe/CO_2 filled time expansion wire chambers.

A more general particle identification is provided by the time of flight detector (TOF) [130]. Here the physics principle is simple, from the time of flight between two points, the velocity of the particle can be calculated. When the momentum of the particle can be deduced from the tracking detectors, this information can be used the calculate the mass of the particle. Particles are then identified based on the mass. The TOF detector consist of multigap resistive wire chambers. These are stacks of resistive plates spaced equally one from the other. They allow time of flight measurements in large acceptance with high efficiency and with a resolution better than 100 ps.

The particle identification capabilities of ALICE are supplemented by the high momentum particle identification detector (HMPID) [131]. The HMPID uses ring imaging Cherenkov counter to identify particles with momentum larger than 1 GeV. Cherenkov radiation is produced when charged particle moves through a material faster than the speed of light in that material. The radiation is emitted at a characteristic angle, which depends on the velocity of the particle. Measuring this Cherenkov angle gives the velocity of the particle, from which the mass can be calculated if the momentum is known. HMPID uses liquid radiator to produce Cherenkov photons and photocathodes in conjunction with multiwire proportional chambers to measure them.

2.3.3 Electromagnetic calorimetry

Electromagnetic calorimeters are designed to measure the energy of particles that interact mainly via the electromagnetic interaction, namely photons and electrons. This makes them an important tool in many neutral meson [132] and direct photon [133] analyses. The energy information is also important for the jet physics. In the context of heavy ion physics, the electromagnetic calorimeters enhance ALICE's capabilities to do jet quenching measurements [134].

There are two electromagnetic calorimeters in ALICE, photon spectrometer (PHOS) [135] and electromagnetic calorimeter (EMCal) [134]. PHOS is a homogeneous calorimeter constructed from scintillating $PbWO_4$ crystals, which generate the bremmstrahlung shower and produce the scintillation light. The amount of light produced is proportional to the particle energy. PHOS also comes with a charged particle veto detector (CPV) [135], which improves the charged particle rejection. PHOS has a very fine granularity, making it well suited for measuring direct photons and neutral mesons.

EMCal is a sampling calorimeter. It consists of layers of lead and scintillator tiles. The lead tiles produce the shower and scintillator tiles the light. The signal is read using wavelength shifting fibres. During the long shutdown 1 in years 2013-2015, EMCal was extended with the di-jet calorimeter (DCal) [136]. The construction of DCal is similar to EMCal. The acceptance of EMCal in the azimuthal angle is $80^\circ < \varphi < 187^\circ$ and DCal extends it by $260^\circ < \varphi < 320^\circ$, providing partial back-to-back coverage. Compared to PHOS, EMCal has coarser granularity but much larger acceptance, making it better suitable for jet physics.

2.3.4 Muon spectrometer

In the forward direction outside the magnet, ALICE has a spectrometer dedicated to measuring muons [137]. Muons in heavy ion collisions are interesting mainly to measure the production of the heavy quark resonances J/ψ, Ψ', Υ, Υ' and Υ''. The muon spectrometer consist of three parts, absorber, muon tracker and muon trigger. The job of the absorber is to remove the hadronic background as efficiently as possible. After the absorber there are ten plates of thin cathode strip tracking stations with high granularity. Between this tracker and the trigger there is still a layer of iron to filter out any remaining particles, that are not muons. Finally in the end of the detector there are four resistive plate chambers that are used to trigger on muons.

2.3.5 Forward and trigger detectors

Besides the detectors mentioned above, ALICE contains a set of small and specialized detectors. The event time is determined with very good precision (< 25 ps) by the T0 detector [138]. T0 is made of a two sets of Cherenkov counters that are mounted around the beam pipe on both sides of the interaction point. The luminosity measurement in ALICE is also done by T0.

Another small detector in the forward direction is the V0 detector [138]. This consist of two arrays of segmented scintillator counters located at $-3.7 < \eta < -1.7$ and $2.8 < \eta < 5.1$ and is used as a minimum bias trigger and for rejection of beam-gas background. V0 is also the main detector used in centrality determination in heavy ion collisions, since the event centrality can be related to the multiplicity of particles in the forward direction [139].

The particle multiplicity measurement to a forward direction is extended by the forward multiplicity detector (FMD) [138]. With the five rings of silicon strip detectors that make up the FMD the charged particle multiplicity can be measured in the range $-3.4 < \eta < -1.7$ and $1.7 < \eta < 5.0$.

To measure the multiplicity of photons, there is the photon multiplicity detector (PMD) [140]. This is done using two planes of gas proportional counters with cellular honeycomb structure. With this arrangement the multiplicity and the spatial distribution of photons can be measured from region $2.3 < \eta < 3.7$.

On top of the ALICE magnet there is an array of 60 large scintillators called the ALICE cosmic ray detector (ACORDE) [141]. This serves as a trigger for cosmic rays for calibration and alignment and can also be used in cosmic ray physics.

The only hadronic calorimeters in ALICE are the zero degree calorimeters (ZDC) [142], which are located next to the beam pipe in the machine tunnel about 116 m from the interaction point. There are two sets of calorimeters: one, made of tungsten, is specialized in measuring neutrons, and the other, made of brass, is specialized in measuring protons. In heavy ion [139] and especially in proton-lead [143] collisions, ZDC gives important information about the centrality of the event. The idea here is to detect spectators, parts of the colliding ions that do not take part in the interaction, after the collision. The more spectators there are, the less central the collision is likely to be.

A new detector installed during the long shutdown 1 is the ALICE diffractive detector (AD) [144, 145]. AD consists of two assemblies, one in each side of the interaction point, both made of two layers of scintillators. These assemblies are situated about 17 m and 19.5 m away from the interaction points. The pseudo-rapidity coverage is $-6.96 < \eta < -4.92$ and $4.78 < \eta < 6.31$, which greatly enhances the capability of ALICE to do diffractive physics measurements that require a large pseudorapidity gap.

2.3.6 L0 trigger in EMCal

Triggers give a possibility to select more probably interesting events in high energy physics collisions. I have made a personal contribution to the development and maintenance for the EMCal level-0 (L0) trigger.

The L0 trigger decision in EMCal and DCal is provided by trigger region units (TRU). A photo of a TRU is presented in Figure 17. The input signal for the TRU comes via the analog input gates at the bottom of the board. The signal goes through analog-to-digital converters (ADC) and arrives to the Virtex FPGA (field-programmable gate array) chip. The main functionality of the TRU is programmed to this FPGA chip. The trigger decision is made inside the chip using an algorithm

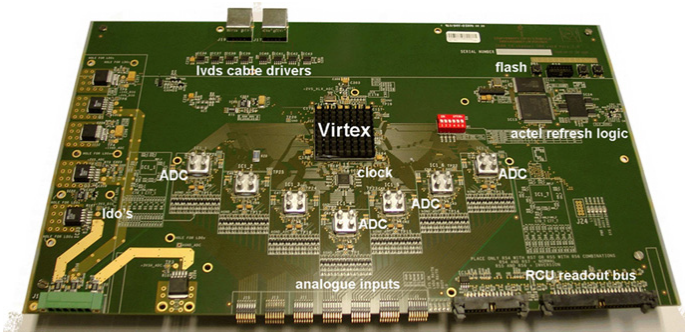

FIGURE 17 A photo of a TRU. Figure from [146].

that will be presented later. The data is sent out from the ethernet ports connected to low-voltage differential signaling (LVDS) drivers in the top of the board. The flash memory in the top right corner of the board is used to load the firmware to FPGA. The low-dropout regulators (LDO) on the left side of the board keep the voltages on the board at desired values. The readout control unit (RCU) readout bus is obsolete, and will not be used anymore in run 2 of LHC. There are a total of 46 TRUs in EMCal and DCal.

After a trigger decision is made in a TRU, the TRU sends this information to a summary trigger unit (STU). There is one STU in EMCal and one in DCal. STU makes a simple OR of all the TRU inputs it receives and forwards this decision to the central trigger processor (CTP). STU also does more complicated calculations on the TRU data to produce a level-1 (L1) trigger, but this out of the scope of this discussion. CTP collects the trigger decisions from all the detectors and sends a confirm signal back to the detectors for the events where the existence of a trigger is verified. The raw data is then read from the detectors upon the arrival of this confirm signal.

The trigger algorithm of the EMCal L0 trigger is described in detail in [146]. I will give here a short overview of it. The EMCal and DCal detectors are formed by a grid of towers, which are the smallest separate regions where a signal can be detected. One TRU channel receives a signal from an area of 2×2 towers. TRU works on a 40 MHz clock, so it receives a new data point every 25 ns. A hit on a tower produces a signal that is several clock cycles wide. An example of such a signal is given in the leftmost histogram in Figure 18. To check if the signal indicates a presence of an interesting event, the first thing the TRU does is to integrate the signal over four time steps. An illustration of this is presented in the left side Figure 18. The purpose of this integration is to minimize the impact of random noise on the input signal. After this, an integration is done over a sliding window of 2×2 channels inside the TRU. This means that trigger decision is done separately for each possible 4×4 tower region in the area of the detector that is connected to a given TRU. Two different conditions must be fulfilled for a trigger decision to be made, as shown in the right side of Figure 18. First of them is that the amplitude of the signal must exceed a preset threshold of ADC counts. This value converted to energy was set to 2.5 GeV for the data taking during 2016. The second condition is that the signal must have expected shape. The trigger is only

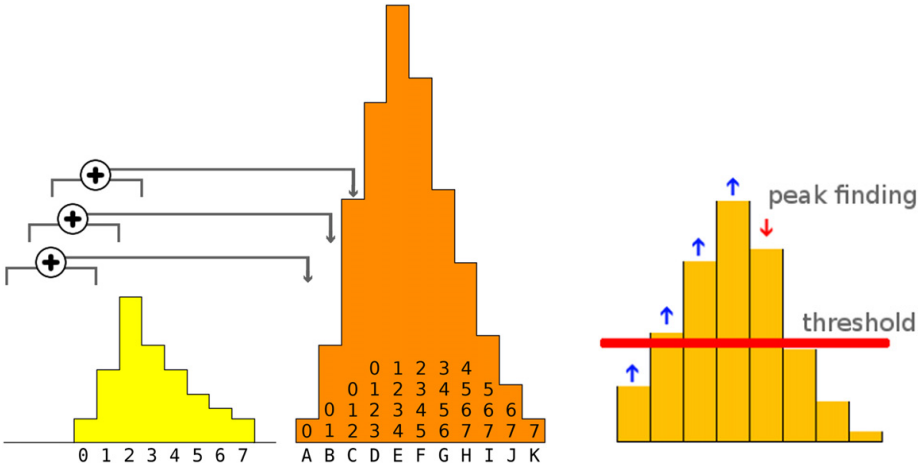

FIGURE 18 *Left:* Illustration of the time integration of the TRU signal. *Right:* Illustration of the required conditions for a trigger decision. Figures from [146].

issued if there is at least four increasing signal amplitudes before the amplitude again starts to decline. This is done to prevent triggering on random noise. When these two conditions are met, the TRU issues a trigger signal.

During the first long shutdown (2013-2015) at the LHC, several upgrades were done for EMCal. For example, the old readout control units were replaced by scalable readout units (SRU). On the TRU firmware side this required a change in the communication protocol. I helped to finalize this part of the code when I arrived to CERN in 2015. I also revised the part of code that mapped the EMCal towers to TRU channels and added a possibility for the TRU to send out a signature pattern of triggers, that can be received by CTP to confirm that they see the expected signal on their side.

After the update of the firmware and installation of DCal, the TRUs needed to be recommissioned before they could take a part in the physics data taking. This was required so that we can be sure that when a TRU sends a trigger, it is done at correct time and for correct reasons. The commissioning was done in several steps. First step was to mask any noisy channels. Certain channels might provide fake triggers due to electric noise somewhere in the detector. These channels must be masked out of the trigger input so that the trigger decisions are made only based on actual signals. The next step was to make sure that CTP sees the triggers sent by the TRUs. This was done by first sending a toggling pattern of triggers (trigger every second clock cycle) and then a signature pattern of triggers to the CTP. The signature pattern is different for different trigger inputs and can be used to identify a specific input. CTP then measures these signals in their end and make sure they see what is expected.

After the triggers are correctly propagated to CTP, the timing of the data sent by the TRU needs to be tuned. As mentioned previously, the trigger amplitudes will be read from the TRU after the arrival of the L0 confirm signal from CTP. The TRU has a rotating buffer, in which it stores the data from each clock cycle. TRU has a parameter that tells from which point of the buffer the data is sent when the

confirm signal arrives. The time it takes for signal to go to the CTP and back needs to be measured in order to ensure that the data sent by the TRU corresponds to the event in which the trigger is issued.

When the data from the TRUs can be seen, the next thing to do is to check that the data read from the TRUs corresponds to the data read from the front end electronics (FEE). The main readout of the towers in EMCal is done directly from FEE cards, and this data is used in EMCal analyses. We want to be sure that the same data is seen also in TRUs. To check this, artificial data is fed to the detector from LED inputs. The LED pulses should be seen everywhere in the detector. An analysis script has been developed that correlates the data that is read from TRUs to the data that is read from FEE. We must see good correspondence everywhere in the detector, otherwise something is wrong. This is a good way to spot badly or wrongly connected cables. These would show as anomalies the the TRU/FEE signal ratio in a specific part of the detector. An example of a plot produced by this analysis script from a LED run for a region of three TRUs is shown in Figure 19. The top left plot in this figure shown the signal amplitude in each TRU channel and the top right plot the signal amplitude in each FEE channel. The bottom left plot correlates these two amplitudes together by showing the TRU amplitude in the horizontal axis and the FEE amplitude in the vertical axis. The two black lines in this correlation plot show the region, where this ratio is expected to be. If a point goes outside of these boundaries, an entry in made to the bottom right histogram to identify the locations of possible problems. You can see that there are three channels with a lot of entries in the bottom right histogram. However, you can see from the top left histogram that there are no entries in these channels in the TRU data. This means that these channels are masked from the readout, likely because they are noisy. Thus these channels corresponds to the region in the correlation plot where TRU amplitude is zero and FEE amplitude shows some non-zero values. The stripe in the right side of the bottom right plot contains only very few hits. These might be isolated cases where the TRU/FEE signal ratio just crosses the boundary in the correlation plot. In general the region explored by Figure 19 looks very good and there is no reason to suspect any problems.

When we know that data in TRUs is from the correct events and it corresponds to the data in the front end, the last step is to align the timing of the trigger decisions. First step of the alignment is to make sure that the triggers come at the same time as for other trigger detectors for the same event. There is a parameter in TRU which can be used to delay the sending out of the trigger after it is generated. This must be tuned to a value which gives the trigger in EMCal in the same bunch crossing as in other trigger detectors. This alignment can be checked online by SMAQ plots. SMAQ is a tool provided by CTP that shows the timing of trigger signals from all the trigger detectors as seen by CTP. An example SMAQ plot taken during the commissioning of the triggers is shown in Figure 20. In the plot the horizontal axis shows relative timing in CTP and the vertical axis the trigger counts for each trigger class. Most of the triggers seem to be issued at time slot 344, so this is the time when the collision is happened. The timing of the EMCal trigger in the plot is given by the red histogram slightly below the center of the plot and

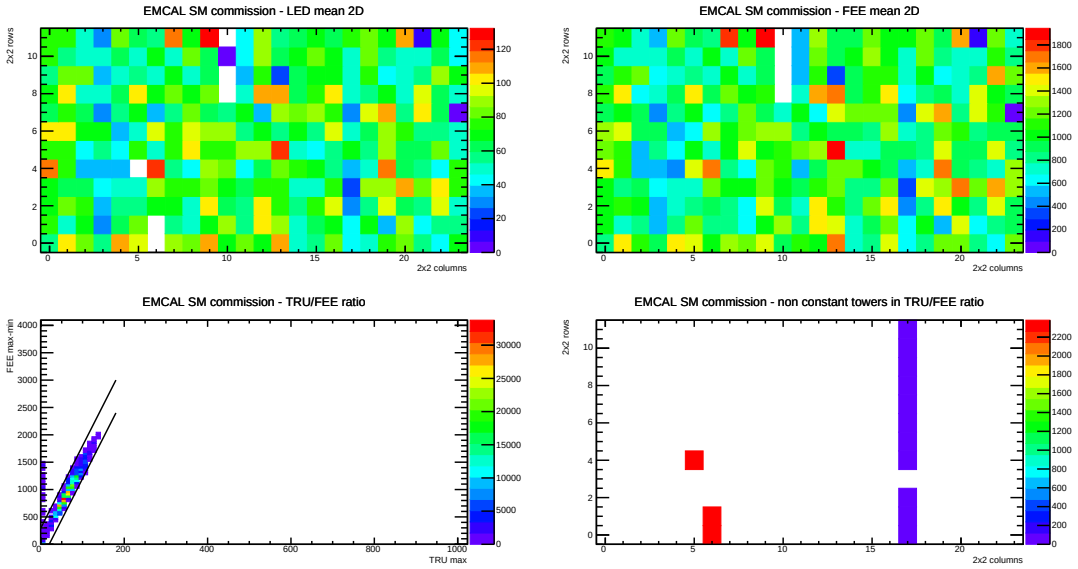

FIGURE 19 Comparison of signal amplitudes in TRUs and FEEs from a LED run.

the DCal timing by the green histogram at the top of the plot. It can be seen that most of EMCal and DCal triggers are coming at the correct time. What remains to be done is to narrow the trigger signals to be only one bunch crossing wide.

The second part of the time alignment is to tune the trigger timing inside each TRU. Different TRU channels correspond to different places in the detector and there might be small differences in the signal propagation time from one channel to another. As the trigger signal is sent out every 25 ns, there can be an ambiguity in which window the signal is sent. We need to align the phase of the internal TRU clock, which is used to generate the signal, with the STU clock, which determines when the signal is sent out, is such a way, that all the signals from one event are sent during the same window. To do this in practice, we need to measure the timing data from each TRU and see how it is distributed. If it is coming uniformly from all channels, no adjustment is needed. If there is a spread in two different windows, we adjust the internal TRU clock phase and measure again. The timing results in a close-to-final commissioning step integrated over all TRUs in EMCal and DCal are shown in Figure 21. In the left hand side plot one can see that the alignment in EMCal starts to look good. Most of the trigger decisions are sent at time step 8. In the DCal there is a small plateau spanning over a large region of time steps. This means that there has been a noisy trigger channel in some TRU sending triggers in random times. By masking the noisy channel and making final adjustments to the clock phase, an accuracy better than 99 % to send all the triggers in the same window was achieved for both EMCal and DCal.

During 2015, I did the above commissioning steps for the TRUs in EMCal and DCal and also wrote a guide how do to the different steps in detail in case the TRUs need to be recommissioned at some point. The L0 trigger was successfully included in the physics data taking in late 2015 and has been performing well since that. In Figure 22 the integrated luminosity for several trigger clusters in ALICE is shown for the data taking during summer 2017. EMCal and DCal L0

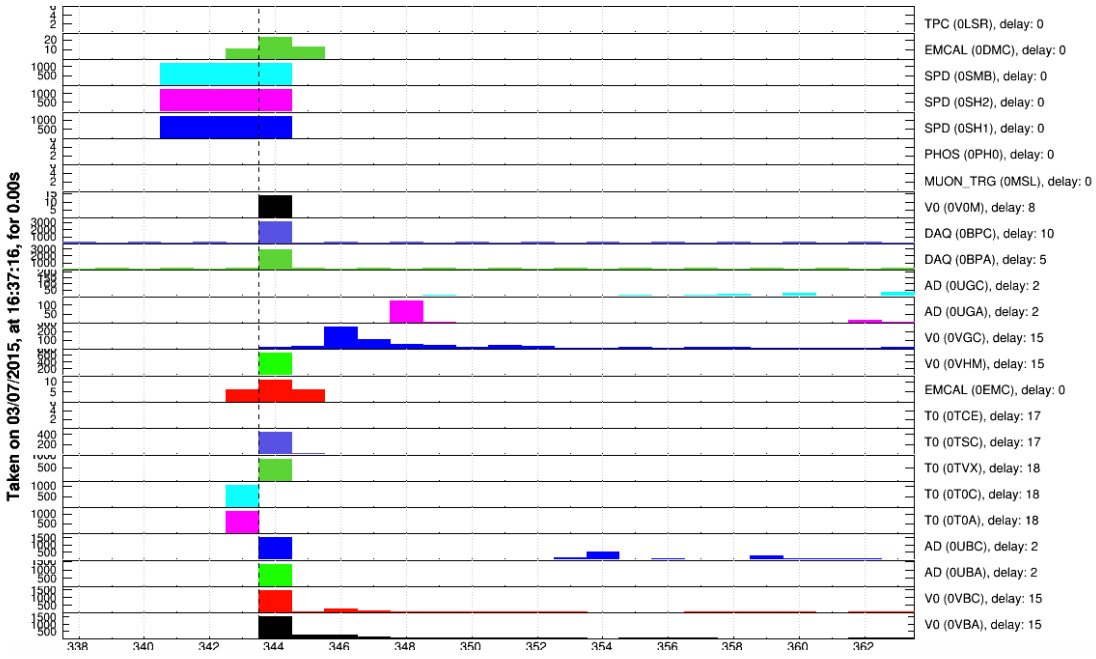

FIGURE 20 A SMAQ plot taken during the trigger commissioning. The plot describes the relative timing between signals from different trigger detectors. DCal signal is the green histogram on the top and EMCal signal the red histogram approximately at the middle of the plot.

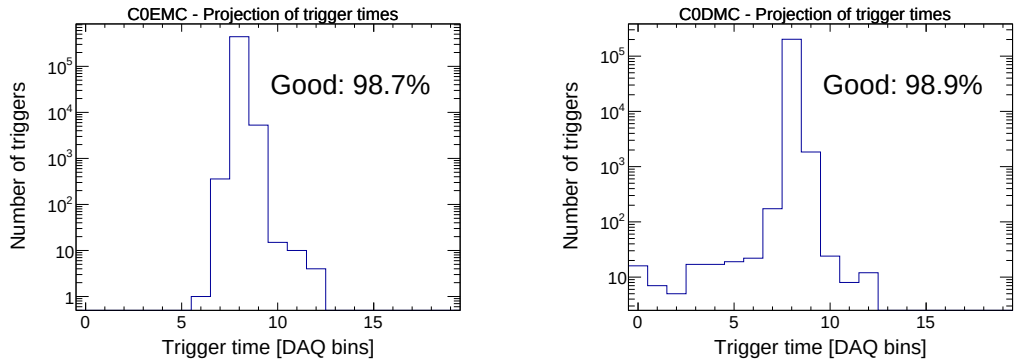

FIGURE 21 The number of trigger decisions sent in time steps of the internal TRU clock in EMCal (left) and DCal (right).

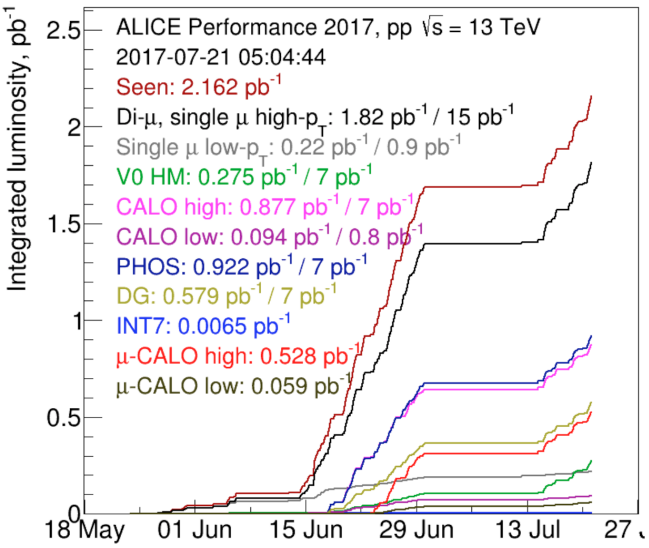

FIGURE 22 Integrated luminosity for different trigger clusters in ALICE in summer 2017. EMCal and DCal L0 triggers are part of all the CALO-classes.

triggers are part of the CALO-trigger classes. This figure confirms that the EMCal L0 trigger is a successful part of the ALICE trigger palette.

3 EVENT AND TRACK SELECTION

3.1 Event selection

This analysis uses minimum bias trigger to select the analyzed events. The minimum bias trigger for pp data is defined in such a way, that at least one hit in SPD or V0 detector is required. SPD is a cylindrical detector around the central beam pipe with a pseodorapidity coverage of $|\eta| < 2$. V0 consist of two scintillator hodoscopes, V0A and V0C, which cover the pseudorapidity region $2.8 < \eta < 5.1$ and $-3.7 < \eta < -1.7$ respectively. Thus, the minimum bias trigger fires if there is at least one charged particle within the aforementioned pseudorapidity region.

The minimum bias definition for p–Pb data is slightly different. Here a signal in both V0A and V0C is required. This change in the minimum bias definition was done in 2012, after better understanding of V0 signals was achieved [147]. This new definition reduces the contamination of the data sample caused by beam-gas events. The two V0 hodoscopes are not symmetrically around the interaction point, as illustrated in Figure 23. This arrangement and the time resolution of V0 allow to identify beam-gas events from beam-beam events occurring in the interaction point. An illustration for this for the $\sqrt{s} = 7\,\text{TeV}$ pp data is shown in Figure 24.

Because of the luminosity leveling to keep the occupancy on TPC in a manageable level, high pile-up is not an issue for ALICE. For the minimum bias pp and p–Pb data analyzed in this thesis the beam separation before the collision was tuned such that the mean number of interactions per bunch crossing was kept below 0.05 in order to avoid significant pile-up [147].

3.2 Track selection

To understand the track cuts used for the analysis, it is first useful to take a quick look on how the tracking in general is done in ALICE. A more detailed overview

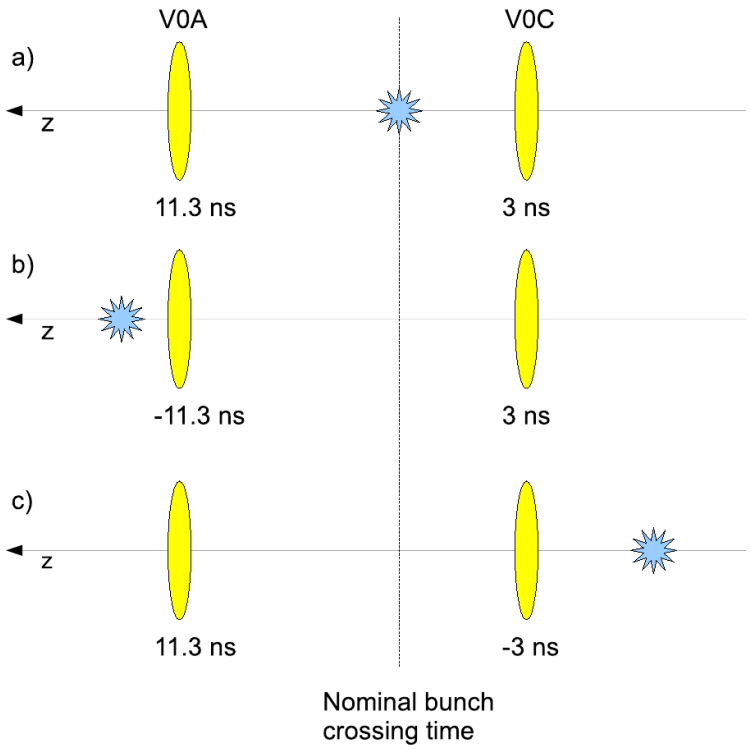

FIGURE 23 Schematic figure of the two V0 hodoscopes. The time it takes for a particle traveling at speed of light to reach V0A from the interaction point is 11.3 ns and the time to reach V0C is 3.0 ns, as illustrated in case a). Cases b) and c) show events, where a beam-gas interaction outside of the interaction point has occurred. Figure from [148].

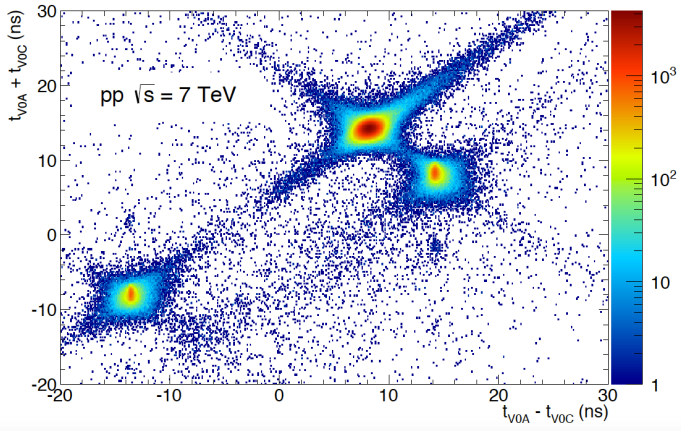

FIGURE 24 Separating beam-beam interactions from beam-gas interactions. Beam-beam interactions sit around $(8.3\text{ ns}, 14.3\text{ ns})$, while the beam-gas interactions can be found around $(14.3\text{ ns}, 8.3\text{ ns})$ and $(-14.3\text{ ns}, -8.3\text{ ns})$. Figure from [147].

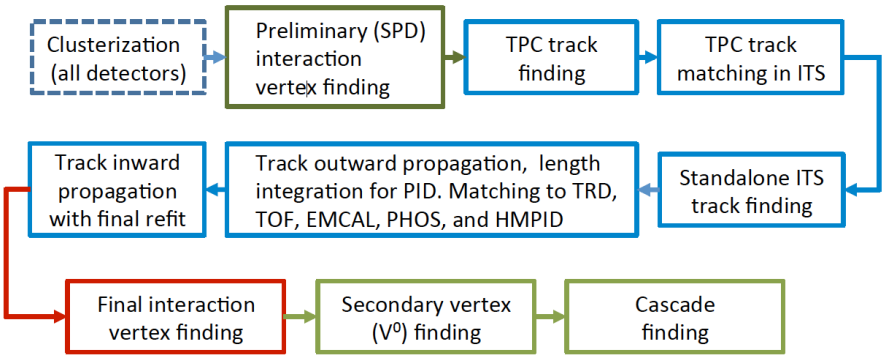

FIGURE 25 Event reconstruction flow. Figure from [147].

can be found from [147]. The tracking in ALICE follows the schema shown in Figure 25. The first step in the event reconstruction flow is the clusterization of data in all detectors, where the data produced by each detectors is converted into clusters. The clusters hold information, for example, about the position, timing and amplitude of the signals, as well as their errors. Then the primary vertex is determined using only SPD information, finding the point where the most lines defined by pairs of SPD clusters are pointing to.

The main reconstruction of tracks starts in TPC. There are 159 tangential pad rows in the TPC readout chambers. The track reconstruction starts from the outermost layer, and the clusters are paired with clusters in the next layer inwards, taking into account a proximity cut. When this track finding procedure hits the innermost pad row in TPC, this information is used as an initial seed for the track finding in ITS. Similar procedure of pairing adjacent layers with a proximity cut is then repeated in ITS.

After the reconstruction of track in ITS is completed, all the tracks are extrapolated to their point of closest approach to the preliminary interaction vertex. Then the second track fitting step begins, this time starting from the interaction point and proceeding outwards. A Kalman filter [149] technique is used to do the new fit using the clusters found in the previous stage. This time the tracks are matched also to the other detectors in the central barrel beyond TPC. When this step is complete, a final refit from the outermost TPC pad rows towards the interaction point is performed. The final track parameters come from this refit.

When the track parameters are final, the primary vertex can be determined with better accuracy than using only SPD information. The tracks are extrapolated to the nominal beam line and a weighted average of the points of closest approach determines the accurate primary vertex position.

The final step of the track reconstruction process is the determination of the secondary vertices. For this, all the tracks whose distance of closest approach (DCA) to the primary vertex is larger than a defined minimum value (0.5 mm in pp and 1 mm in Pb–Pb) are selected. For these tracks, points of closest approaches are determined for pairs of tracks. If the tracks are sufficiently close to each other and show characteristics of short lived particle decays (for example, decays of K^0_s or Ξ^-), these points are identified as secondary vetrices.

After this quick look on the track reconstruction in ALICE, we can move on to the track cuts that are used in this analysis. These cuts are summarized in Table 1. The set of track cuts used in the pp analysis is titled GlobalSDD and the set of cuts used in p–Pb analysis Hybrid. The hybrid tracks are selected in two steps, where in the second step some additional tracks are accepted, that were originally rejected in the first step. Both of these two cuts are standard track cuts used in ALICE, and they are readily implemented in the data files for analyzers. The parameters for the GlobalSDD cut are tuned to optimize the best possible track quality by minimizing the contamination form secondary particles. Secondary particles are particles that are not produced in the hard scattering, but are products of decays or interactions with the detector material [150]. For the hybrid tracks the φ acceptance is optimized to be as uniform as possible, with a small cost in the overall track quality.

The first requirements are on the quality of the track fit in ITS and TPC. The requirement χ^2 / ITS cluster < 36 only removes track with clear outliers. For TPC χ^2 / TPC cluster < 4 gives much more strict requirement for track quality. To be able to do the fit properly in ITS, it is required that there are at least 3 out of the maximum of 6 hits in ITS. In addition to this, in the GlobalSDD cut there is required to be one hit in SPD or in the first SDD layer. For the hybrid cuts in step 1 the requirement is that this hit is strictly in SPD. In the step 2 of the hybrid cut the ITS hit requirements are replaced by an additional vertex constraint, where the primary vertex itself is added as a point to the track to improve the momentum resolution. Requiring the hit in SPD makes the extrapolation of tracks to the primary vertex more reliable. Relaxing this condition to a hit in the first SDD layer or including the vertex itself in the track reconstruction is done to battle against the inefficiencies caused by inactive regions in SPD. The total inactive SPD volume was approximately 20 % during the pp data taking and approximately 5 % during the p–Pb data taking [147].

For the TPC, 70 crossed pad rows out of the maximum of 159 is required. This measures the effective track length inside the TPC. It is not the same as number of clusters, since it takes into account the fact that there might be a pad rows missing in the middle of the track due to charge in these clusters being below the threshold for some reason. In addition to this, it is required that the ratio between crossed rows and findable clusters is at least 0.8. Findable clusters are defined as the number of geometrically possible clusters which can be assigned to a track. It takes into account dead zones due to chamber boundaries and the limited η-acceptance. This can be different from the crossed rows if, for example, the particle interacts with the detector material and is absorbed. For both steps of the hybrid cut, it is also required that the fraction of shared clusters for a track is less than 40 %. A shared cluster is defined as a cluster that is shared with several tracks. On top of these cuts that remove a small fraction of bad quality tracks, we only accept tracks with $|\eta| < 0.8$ to avoid border effects of the TPC acceptance $|\eta| < 0.9$.

A few more cuts are included to make sure that the measured tracks are really produced in the primary collision. A track might gain a kink due to a particle

TABLE 1 Definitions of the main track cuts used in this analysis.

Track cut	GlobalSDD	Hybrid, step 1	Hybrid, step 2
χ^2 / ITS cluster	< 36	< 36	< 36
χ^2 / TPC cluster	< 4	< 4	< 4
Hits in ITS	3	3	0
ITS hit requirements	1 in SPD or first SDD layer	1 in SPD	No requirement
Vertex constraint	No	No	Yes
Number of crossed rows in TPC	70	70	70
TPC crossed rows over findable clusters	> 0.8	> 0.8	> 0.8
Fraction of shared TPC clusters	< 1	< 0.4	< 0.4
Kink daughters	Rejected	Rejected	Rejected
DCA_{xy}	< 0.0105 cm $+0.035$ cm $\cdot\, p_{\mathrm{T}}^{-1.1}$	< 3.2 cm	< 3.2 cm
DCA_{z}	< 2 cm	< 2.4 cm	< 2.4 cm
Other			Rejected by step 1

scattering or decay. After this, it is no longer describing the properties of the primary collisions. A particle after such a kink in the track is called kink daughter. Kink daughters are rejected in all the track cuts. The final cuts are on the distance of closest approach (DCA) of the track to primary vertex. To have confidence that the particle is produced in the primary collision, the track must come close enough from the primary vertex. There are different requirements for the transverse plane with respect to the beam (DCA_{xy}) and along the beam direction (DCA_z). For the GlobalSDD the DCA cut in the beam direction is $\mathrm{DCA}_z < 2$ cm and in the transverse plane it there is a momentum dependent cut $\mathrm{DCA}_{xy} < 0.0105\ \mathrm{cm} + 0.035\ \mathrm{cm} \cdot p_{\mathrm{T}}^{-1.1}$. For the hybrid track selection the DCA cuts are a bit looser measuring $\mathrm{DCA}_z < 2.4$ cm and $\mathrm{DCA}_{xy} < 3.2$ cm.

For the systematic uncertainty analysis slightly varied track cuts are studied and compared to these standard cuts. For the pp data, the systematic uncertainty coming from track selection is estimated by comparing a looser DCA cut with the regular tight DCA cut. This looser cut is the same as the DCA cut defined for the hybrid tracks in Table 1. For the p–Pb data, we compare a set of cuts close to GlobalSDD cut set to hybrid track cuts. The differences in this and the GlobalSDD cuts are, that now a hit in SPD is required instead of SPD or first SDD layer, and in TPC 50 cluster hits is required instead of crossed row requirements.

4 ANALYSIS METHODS

4.1 Two-particle correlations

Two-particle correlations is a statistical method, where pairs of particles from many events are studied. In each event the particles are classified as trigger particles, associated particles or background particles. The trigger particles are the particles we correlate the other particles with. The associated particles are particles that have a desired correlation with the trigger particle. The background particles are uncorrelated with the trigger particle or have an undesired correlation with the trigger particle. For a particle to be accepted as a trigger or an associated particle, it must fulfill the requirements preset for these particles. For example, one might require that the trigger particle transverse momentum must be on the interval $8 < p_{\mathrm{Tt}} < 10$ GeV/c and the associated particle transverse momentum on the interval $3 < p_{\mathrm{Ta}} < 4$ GeV/c. Any particles not fulfilling these requirements are not considered in the analysis. In the analysis each trigger particle is correlated with each other particle in the associated particle momentum range. When this pairing is done for many events, the statistical properties of the system can be obtained.

One example of the observables that can be studied is the azimuthal angle difference between the two particles $\Delta\varphi$. This is illustrated in Figure 26. In the left side of the figure the beam goes along the z-axis. Azimuthal angle is the angle in the transverse plane with respect to the beam. As most of the high-p_{T} events in colliders are di-jet events, when we collect statistics from many events a distribution as shown in the right side of the figure emerges. Here near side refers to particle pairs having $\Delta\varphi < \frac{\pi}{2}$ and the peak around $\Delta\varphi = 0$ is coming from the pairs of particles both coming from the same jet. The away side is defined to be the area $\frac{\pi}{2} < \Delta\varphi < \frac{3\pi}{2}$ and in the away side peak a trigger particle from one jet is correlated with an associated particle from another jet. In an ideal case the momentum conservation forces the two jets to be back-to-back. This is why the away side peak is generated around $\Delta\varphi = \pi$. The away side peak is lower and wider than the near side peak since in the actual experiment there are effects that cause deviations to the ideal back-to-back kinematics. These include higher order

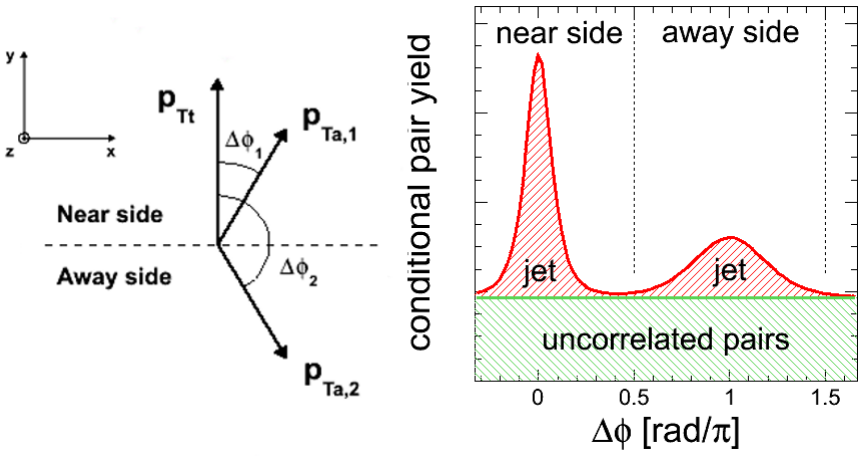

FIGURE 26 Example of two-particle correlations on $\Delta\varphi$. On the left side of the figure there is an illustration about the definition of $\Delta\varphi$. On the right side there is the correlation structure after collecting the data from many events.

corrections and partons having some intrinsic transverse momentum inside the colliding hadrons. Both of these two peaks are sitting on top of a nearly constant background, coming dominantly from the underlying event. As in the underlying event pairs the background particles are not correlated to the trigger particles in any particular manner, a uniform background below near and away side peak is seen.

4.2 Definition of j_T distribution and background

This analysis is done using two-particle correlations as the analysis method. The goal is to study the jet fragmentation transverse momentum j_T, which is defined as the transverse momentum component of the jet fragment with respect to the jet axis. In this analysis the jet axis is approximated by the trigger particle. We select the highest transverse momentum particle in each event to be the trigger particle. This is called the leading particle and if it has sufficiently high p_T, it is a good approximation of the jet axis.

We can construct an observable for j_T by interpreting the associated particles as jet fragments. In this case $\vec{j}_T$ is defined as the transverse momentum component of the associated particle momentum $\vec{p}_a$ with respect to the trigger particle momentum $\vec{p}_t$. The resulting $\vec{j}_T$ is illustrated in Figure 27. We are interested in the length of the $\vec{j}_T$ vector, which is defined as

$$j_T = \frac{|\vec{p}_t \times \vec{p}_a|}{|\vec{p}_t|}. \tag{30}$$

The results are presented in bins of the fragmentation variable $x_{\parallel}$. This is defined as the projection of the associated particle momentum to the trigger particle divided

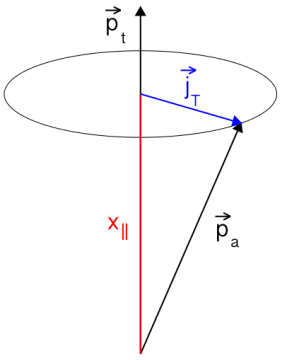

FIGURE 27 Illustration of $\vec{j}_T$ and $x_\parallel$. When the trigger particle is a high-p_T particle that approximates the jet axis sufficiently well, the $\vec{j}_T$ can be written as the transverse momentum component of the associated particle momentum $\vec{p}_a$ with respect to the trigger particle momentum $\vec{p}_t$. The fragmentation variable $x_\parallel$ is the projection of $\vec{p}_a$ to $\vec{p}_t$ divided by p_t.

by the trigger particle momentum:

$$x_\parallel = \frac{\vec{p}_t \cdot \vec{p}_a}{\vec{p}_t^{\,2}} \,. \tag{31}$$

Because $x_\parallel$ follows the trigger particle by construction, it is intuitive to define the near side with respect to this axis rather than using the traditional azimuthal angle difference. The associated particle is defined to be in the near side if it is in the same hemisphere as the trigger particle:

$$\vec{p}_t \cdot \vec{p}_a > 0 \,. \tag{32}$$

This definition raises a need for a non-standard acceptance correction method. For this, a new method is derived and all the details are presented in Section 4.4.

We have chosen to use $x_\parallel$ rather than p_{Ta} to bin the results because the definition of j_T in equation (30) has an explicit p_{Ta} dependence. This biases the p_{Ta} bins in a way that is illustrated in Figure 28. In this figure $|\vec{p}_{a,1}| = |\vec{p}_{a,2}|$ and $j_{T,1} = j_{T,2} = j_T$, but since $\vec{j}_T$ vectors point to different directions for particles 1 and 2, it follows that $p_{Ta,1} > p_{Ta,2}$. Thus the random orientation of $\vec{j}_T$ can affect the p_{Ta} bin the result is assigned to. Let us call the increase of p_{Ta} due to orientation of $\vec{j}_T$ an upwards fluctuation and the decrease of p_{Ta} a downwards fluctuation. The fact that the orientation of $\vec{j}_T$ affects p_{Ta} is likely to increase $\langle j_T \rangle$ in any given p_{Ta} bin, since the p_{Ta} spectrum is exponentially falling and it is thus more likely that a particle enters a p_{Ta} bin due to an upwards fluctuation over the lower bin edge than that a particle leaves the bin due to upwards or downwards fluctuations. This point is discussed in more detail with the help of a toy simulation in Appendix 1. In the case of $x_\parallel$ this bias is not present, since $x_\parallel$ is by definition perpendicular to $\vec{j}_T$.

Another advantage for using $x_\parallel$ binning is that it scales with trigger p_T. In this way the average fraction of the leading parton momentum taken by the

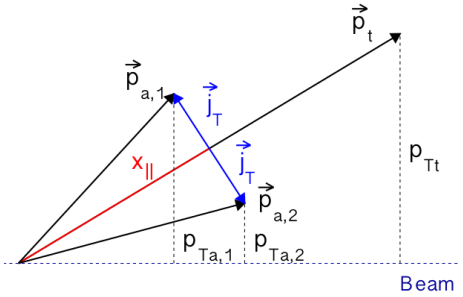

FIGURE 28 Illustration why p_{Ta} binning biases the j_{T} results.

leading particle ($\langle z_{\mathrm{t}} \rangle$) stays rather constant inside an $x_{\parallel}$ bin, as is illustrated in Appendix 2 with the help of a PYTHIA 8 study.

For the analysis we choose the trigger particles to be leading particles in the transverse momentum range $3 < p_{\mathrm{Tt}} < 15$ GeV/c. The lower limit is chosen to be $p_{\mathrm{Tt}} = 3$ GeV/c, since below that we do not trust that the leading particle can reliably estimate the jet axis. The upper limit is dictated by the statistics, the bins above $p_{\mathrm{Tt}} = 15$ GeV/c have too little statistics for reliable results. As associated particles we select particles with $x_{\parallel} > 0.2$. We only study the associated particles from the near side, since j_{T} as defined in equation (30) requires that the jet fragments come from the same jet as the trigger particle. The exact form of the extracted j_{T} distribution is

$$\frac{1}{N_{\mathrm{trigg}}} \frac{1}{j_{\mathrm{T}}} \frac{\mathrm{d}N}{\mathrm{d}j_{\mathrm{T}}} = \frac{N_{\mathrm{pairs}}(p_{\mathrm{Tt}}, p_{\mathrm{Ta}}, \Delta\eta, \Delta\varphi)\, C_{\mathrm{pair}}(p_{\mathrm{Tt}}, p_{\mathrm{Ta}})\, C_{\mathrm{Acc}}(\Delta\eta, \Delta\varphi)}{j_{\mathrm{T}}\, N_{\mathrm{trigg}}(p_{\mathrm{Tt}})\, C_{\mathrm{trigger}}(p_{\mathrm{Tt}})}, \tag{33}$$

where N_{trigg} is the number of triggers, $N_{\mathrm{pairs}}(p_{\mathrm{Tt}}, p_{\mathrm{Ta}}, \Delta\eta, \Delta\varphi)$ is the number of trigger-associated pairs, $C_{\mathrm{pair}}(p_{\mathrm{Tt}}, p_{\mathrm{Ta}})$ is the pair efficiency correction, $C_{\mathrm{trigger}}(p_{\mathrm{Tt}})$ is the single track efficiency correction for the trigger particle and $C_{\mathrm{Acc}}(\Delta\eta, \Delta\varphi)$ is the acceptance correction. In the analysis code level, the pair efficiency and acceptance corrections together with the $\frac{1}{j_{\mathrm{T}}}$ weight are applied when the pairs are filled to histograms. The details on how the corrections are obtained and why they are needed are explained in the next sections. The $\frac{1}{N_{\mathrm{trigg}}}$ scaling is applied later as this number is obtained by integrating the trigger p_{T} distribution over the range of a given bin. The trigger efficiency correction is applied when the trigger p_{T} distribution is filled. The purpose of the $\frac{1}{N_{\mathrm{trigg}}}$ scaling is to make datasets of different sizes comparable with each other.

The background for the measurement comes mostly from the underlying event. In addition to this, short lived particles that decay after the hadronization but before they hit the detector may add an additional undesired correlation component. There can also be a contribution from long range azimuthal correlations, that have been observed in pp system by CMS and ATLAS [151, 152] and in p–Pb system by ALICE, CMS and ATLAS [74, 153, 154]. However, the kinematic ranges in these studies are different than the range in this analysis. ALICE and CMS study trigger particles upto $p_{\mathrm{Tt}} = 4$ GeV/c and ATLAS upto $p_{\mathrm{Tt}} = 5$ GeV/c. These ranges only coincide with the lowest p_{Tt} bins in this analysis, and ATLAS reports

in [152] that the correlations get weaker above $p_{\mathrm{Tt}} = 3$ GeV/c. Furthermore CMS and ATLAS report the correlations in region $2 < \Delta\eta < 5$, while the reach of this analysis is $\Delta\eta < 1.6$. Thus the contribution of long range azimuthal correlations to the background of this analysis is most likely small.

To estimate the background contribution from the underlying event and long range azimuthal correlations, we rely on the fact that particles from the same jet are expected to be close to each other. Thus selecting pairs with large angular distance should give us contribution only from the background. This is done in the pseudorapidity gap background estimation method, in which all the pairs with $\Delta\eta > 1$ are defined to be background for the analysis. This background then needs to be extrapolated also to the region $\Delta\eta < 1$. For each large $\Delta\eta$ pair we find, we randomize new η values for the trigger and associated particles from the measured inclusive pseudorapidity distributions. This way 20 new pairs are generated for each large $\Delta\eta$ pair. This gives a background estimation for the whole η range in which the pseudorapidities follow the inclusive distributions, but the azimuthal angles and transverse momenta retain any possible characteristics that background pairs might have different with respect to the signal pairs.

For the systematic uncertainty analysis, a slightly varied background estimation method is also implemented. In the varied method all the pairs with $R = \sqrt{\Delta\varphi^2 + \Delta\eta^2} > 1$ are defined to be background pairs. The background is then extrapolated to the signal region by randomizing both pseudorapidities and azimuthal angles for the trigger and associated particles from the inclusive distributions. Defining the background this way we do not retain the possible azimuthal angle modulation for the background pairs. For this analysis we expect these modulations to be small, and thus believe that this method can be used for the systematic uncertainty estimation. However, this method cannot be extended to the Pb–Pb system, where a strong $\Delta\varphi$ modulation is observed [47, 155, 156].

4.3 Efficiency correction

The efficiency corrections are obtained from ALICE Monte Carlo productions by comparing the reconstructed particles to generator level particles. The idea of the efficiency correction is to correct for the reconstruction efficiency of charged physical primary particles. Charged physical primaries are particles produced in a collision including the products of strong and electromagnetic decay and excluding the feed-down from weak decays of strange particles [150]. Single track overall reconstruction correction $C(p_{\mathrm{T}})$ takes into account the contamination of the reconstructed track sample with fake primary tracks and the track reconstruction efficiency. It is given by

$$C^{-1}(p_{\mathrm{T}}) = \frac{M_{\mathrm{trgvtx}}(p_{\mathrm{T}}) + B(p_{\mathrm{T}})}{G_{\mathrm{trgvtx}}(p_{\mathrm{T}})}\,, \tag{34}$$

where M_{trgvtx} is the number of properly reconstructed primary tracks, B the number of fake and secondary tracks and G_{trgvtx} is the number of true charged

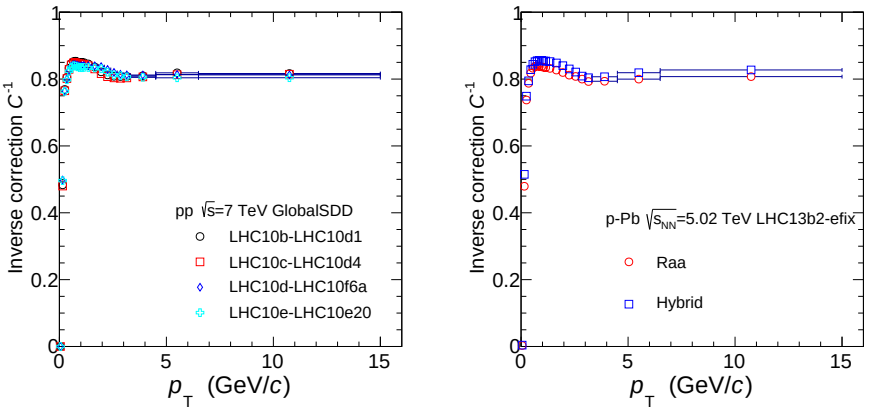

FIGURE 29 Inverse single particle overall efficiency correction for pp $\sqrt{s} = 7\,\text{TeV}$ (left) and p–Pb $\sqrt{s_{\text{NN}}} = 5.02\,\text{TeV}$ (right) for the track cuts used in this analysis.

physical primaries. All these three quantities are taken from triggered events where an event vertex is reconstructed. For the track cuts used in this analysis, the inverse correction factor $C^{-1}(p_{\text{T}})$ is presented in Figure 29.

Because this j_{T} analysis is a two-particle correlation analysis, we are always looking at pairs of particles instead of single particles. Thus we need to have a correction for a pair of particles instead of just a single particle. Since we only see the pair if we manage to reconstruct both of the particles, the pair efficiency correction C_{pair} becomes

$$C_{\text{pair}}(p_{\text{Tt}}, p_{\text{Ta}}) = C_{\text{trigger}}(p_{\text{Tt}})C_{\text{associated}}(p_{\text{Ta}})\,, \tag{35}$$

where C_{trigger} and $C_{\text{associated}}$ are the single track overall reconstruction corrections for trigger and associated particles.

Due to the fine granularity of the ALICE TPC, two track effects, like track merging or splitting, are small for pp and p–Pb collisions. It is reported in [157] that the effect from track merging or splitting for particle yields is approximately 0.5 % in pp collisions for pairs with $\Delta\phi = 0$. This uncertainty is small compared to other uncertainties in this analysis, and thus the two track effects are neglected.

4.4 Acceptance correction

Defining the near side as in equation (32) leads to specific requirements for acceptance correction. Traditionally the acceptance correction is obtained by dividing the same event distribution with the mixed event distribution. In the mixed event distribution particles from different events are correlated with each other. This kills all physical correlations between particles, but retains any possible detector or acceptance effects. Dividing by normalized mixed event distribution removes these effects from the same event distribution. With the new near side definition this does not work directly because in some cases the away side cuts away part

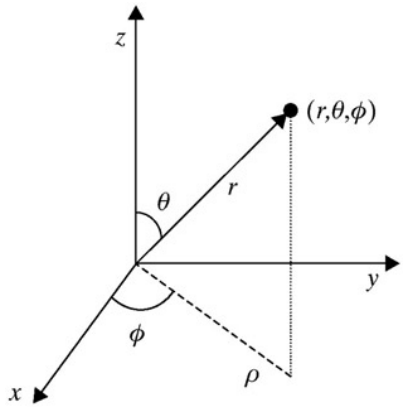

FIGURE 30 Definition of the spherical coordinate system. The beam is in z-direction.

of the acceptance. Thus we may lose some particles from a particular $(\Delta\eta, \Delta\varphi)$ region because these particles are now defined to be on the away side, not because of acceptance effects. This section explains in detail how these border effects can be taken into account.

Let us first take a look how the near side looks like following the definition given in equation (32). For this, we need to figure out the equation for the angle between trigger and associated particle as a function of the pseudorapidity and azimuthal angle of these particles. The derivation of this is best done in the spherical coordinates. The spherical coordinate system is defined as in Figure 30. Thus r is the magnitude of the vector, φ is the angle in the xy-plane and θ in the angle with respect to z-axis. In the experimental setup the beam axis will be in z-direction. The correspondence to the Cartesian coordinates is the following:

$$\begin{cases} x = r\sin(\theta)\cos(\varphi) \\ y = r\sin(\theta)\sin(\varphi) \\ z = r\cos(\theta) \end{cases} \tag{36}$$

Notice that the domains of the variables are:

$$\begin{cases} r \in [0,\infty[\\ \varphi \in [0,2\pi[\\ \theta \in [0,\pi] \end{cases} \tag{37}$$

The near side is defined to be the region of space, where the angle α between the trigger and associated particle momentum vectors is $\alpha < \frac{\pi}{2}$. The angle α can be calculated from the dot product of two vectors $\vec{v}_1$ and $\vec{v}_2$.

$$\begin{aligned} \vec{v}_1 \cdot \vec{v}_2 &= x_1x_2 + y_1y_2 + z_1z_2 \\ &= r_1r_2\sin(\theta_1)\cos(\varphi_1)\sin(\theta_2)\cos(\varphi_2) + r_1r_2\sin(\theta_1)\sin(\varphi_1)\sin(\theta_2)\sin(\varphi_2) \\ &\quad + r_1r_2\cos(\theta_1)\cos(\theta_2) \\ &= r_1r_2[\sin(\theta_1)\sin(\theta_2)(\cos(\varphi_1)\cos(\varphi_2) + \sin(\varphi_1)\sin(\varphi_2)) + \cos(\theta_1)\cos(\theta_2)] \\ &= r_1r_2[\sin(\theta_1)\sin(\theta_2)\cos(\varphi_1 - \varphi_2) + \cos(\theta_1)\cos(\theta_2)] \\ &= r_1r_2\cos(\alpha) \end{aligned} \tag{38}$$

Solving for α and using $\cos(\varphi_1 - \varphi_2) = \cos(\Delta\varphi)$ gives

$$\alpha = \arccos[\sin(\theta_1)\sin(\theta_2)\cos(\Delta\varphi) + \cos(\theta_1)\cos(\theta_2)] \,. \tag{39}$$

Remember that the angle θ with respect to the beam is connected to pseudorapidity η with

$$\eta = -\ln\left[\tan\left(\frac{\theta}{2}\right)\right] \Leftrightarrow \theta = 2\arctan(e^{-\eta}) \,. \tag{40}$$

We can see from equation (39) that for the azimuthal angle, the 3D near side definition depends only on the difference $\Delta\varphi$. However, for pseudorapidity such a simple dependence in not seen, but we need to take into account the pseudorapidities of trigger and associated particles separately.

We can find an equation for near-away side boundary form the equation (39). For the boundary $\alpha = \frac{\pi}{2}$, meaning that $\cos(\alpha) = 0$. Replacing θ with η as defined in equation (40), the equation (39) can be solved for η_1:

$$\eta_1 = -\ln\left[\tan\left[\frac{\arctan\left(\frac{-\cos\left(2\arctan(e^{-\eta_2})\right)}{\sin\left(2\arctan(e^{-\eta_2})\right)\cos(\Delta\varphi)}\right)}{2}\right]\right] \,. \tag{41}$$

An illustration how the near side looks like in (η_1, η_2) plane for constant values of $\Delta\varphi$ can be seen in Figure 31. In this notation η_1 stands for the trigger particle pseudorapidity and η_2 for the associated particle pseudorapidity. The black squares in the middle of the plots show the region $-0.8 < \eta_{1,2} < 0.8$, which is the acceptance of this analysis. The main difference to the traditional near side definition $\Delta\varphi < \frac{\pi}{2}$ is, that in the new definition part of the acceptance can be in the near side and part in the away side. This is because the near side for 3D definition depends on η_1 and η_2 in addition to $\Delta\varphi$. It turns out that this fact causes the traditional acceptance correction method of dividing by mixed event to break down in the edges of the phase space for this near side definition. Luckily, this can be fixed in a simple way, as will be explained in detail in the text below.

Let's first take a look at how the traditional acceptance correction is derived. The underlying assumption behind the acceptance correction is that the jet is symmetric around the jet axis. If we approximate $\eta \sim \theta$ and remember that we approximate the jet axis with a trigger particle, this translates to assuming that the pairs that have the same $\Delta\eta$ and $\Delta\varphi$ are similar.

It is useful to define a variable for the probability to see the associated particle inside the acceptance, provided that the trigger particle is inside the acceptance. We can call this the acceptance triangle $\mathrm{Acc}_\triangle$. The trigger particle is always required to be inside the acceptance, because no events are analyzed if the trigger happens to be outside. Written as a formula this reads

$$\mathrm{Acc}_\triangle = \frac{P(\text{inside})}{P(\text{inside}) + P(\text{outside})} = P(\text{inside}) \,, \tag{42}$$

where $P(\text{inside})$ is the probability that both trigger and associated particles are inside the acceptance and $P(\text{outside})$ is the probability that the associated particle

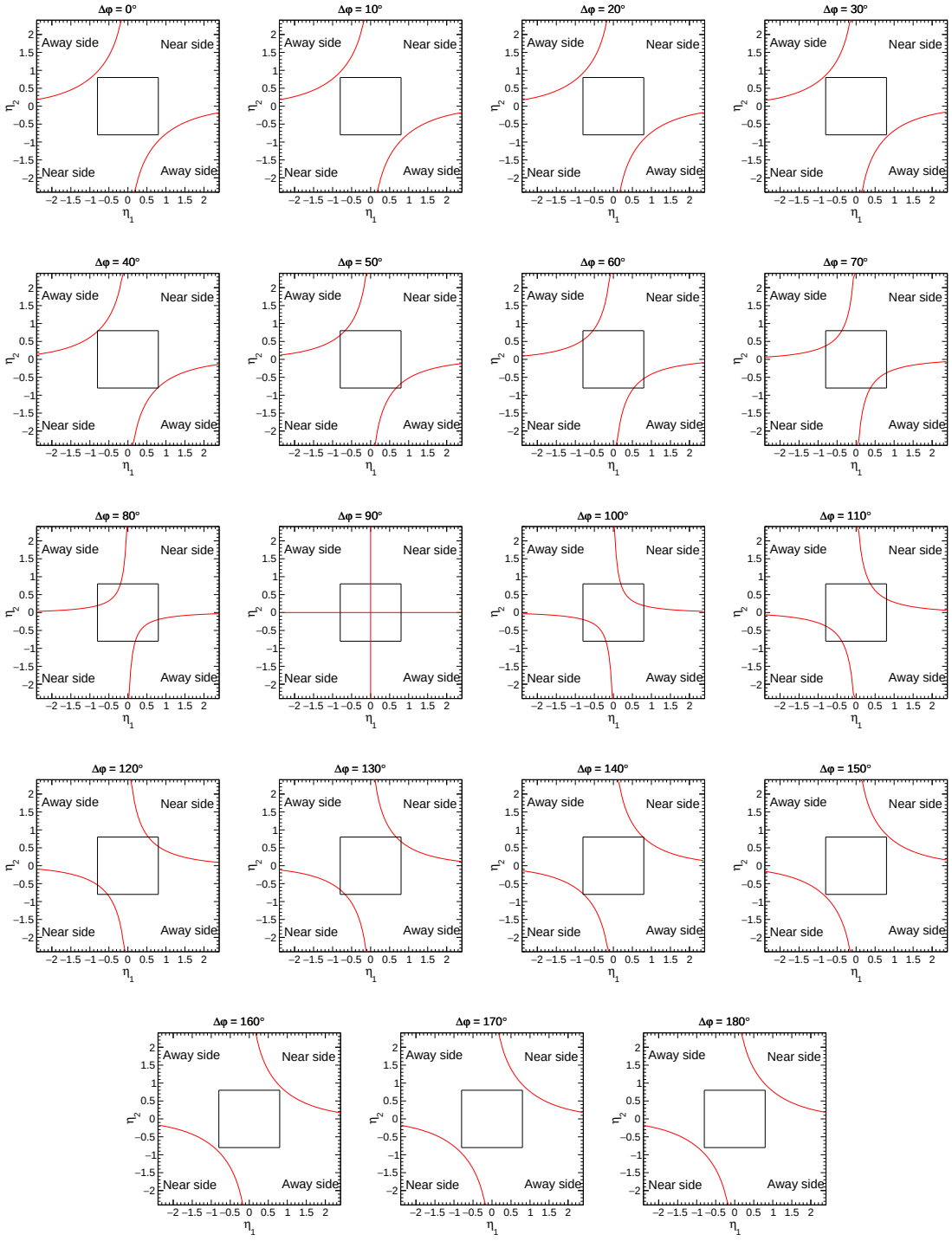

FIGURE 31 Illustration of 3D near side in (η_1,η_2) plane for constant values of $\Delta\varphi$. The acceptance of the analysis is presented by a black square.

is outside of the acceptance while the trigger particle is inside. Since the associated particle must always be either inside or outside of the acceptance, it follows that $P(\text{inside}) + P(\text{outside}) = 1$. These probabilities are illustrated in Figure 32. In the left hand side plot of this figure η_1 is the trigger particle pseudorapidity and η_2 the associated particle pseudorapidity. The figure is drawn for constant $\Delta\varphi$. In the traditional case, the figure will be identical for all $\Delta\varphi < \frac{\pi}{2}$. The black box in the middle is the acceptance of the analysis. As the acceptance is 0.8 units in pseudorapidity, the maximum $\Delta\eta$ that can be seen within this acceptance is $\Delta\eta_{\text{max}} = 1.6$. The black triangles on top and bottom of the box are the areas, where the associated particle is outside of the acceptance but where $\Delta\eta < 1.6$. A constant $\Delta\eta$ line is drawn to the figure. Since we assume that pairs with the same $\Delta\eta$ and $\Delta\varphi$ are similar and the figure is drawn for constant $\Delta\varphi$, we assume that the particles following this line are similar. The blue part of the line describes the particles that are inside the acceptance and the magenta part of the line the particles that are outside of the acceptance. The lengths of these lines are proportional to the probabilities to see an associated particle inside or outside of the acceptance. We can write the equation for the acceptance triangle using the lengths L of these lines as

$$\text{Acc}_{\triangle} = \frac{L(\text{inside})}{L(\text{inside}) + L(\text{outside})} \,. \tag{43}$$

Doing this calculation for each $\Delta\eta$ value yields a triangular shape for the acceptance triangle (hence the name), as can be seen in the right hand side plot of Figure 32. This acceptance effect introduces an unwanted bias to the measured distributions, since it is more probable to see pairs with small $\Delta\eta$ due to detector limitations. We can get rid of this bias by weighting all the pairs that are filled to data histograms by the inverse probability to see the pair. Thus the actual acceptance correction will be the inverse of the acceptance triangle

$$C_{\text{acc}}(\Delta\eta) = \frac{1}{\text{Acc}_{\triangle}} \,. \tag{44}$$

In an actual analysis, a simple triangle as shown in Figure 32 is not used. A mixed event distribution is used instead. Mixing particles from different events destroys all the possible correlations between the particles. The only effects that are left are detector effects. These include possible detector inefficiencies and the detector geometry. As all the correlations between the particles are destroyed, the mixed event distribution is proportional to the probability to see the associated particle inside the acceptance $P(\text{inside})$. In terms of Figure 32, this would be proportional to the length of the blue line $L(\text{inside})$. Now as the denominators in equations (42) and (43) are constant, normalizing the maximum of the mixed event distribution to 1 will give the properly normalized acceptance triangle. Then the acceptance correction for any given particle pair can be obtained by dividing it by the corresponding point in the mixed event distribution.

Now let's look at the 3D near side. Here there is some probability that the away side will be inside the acceptance. The particles that are not in our near side

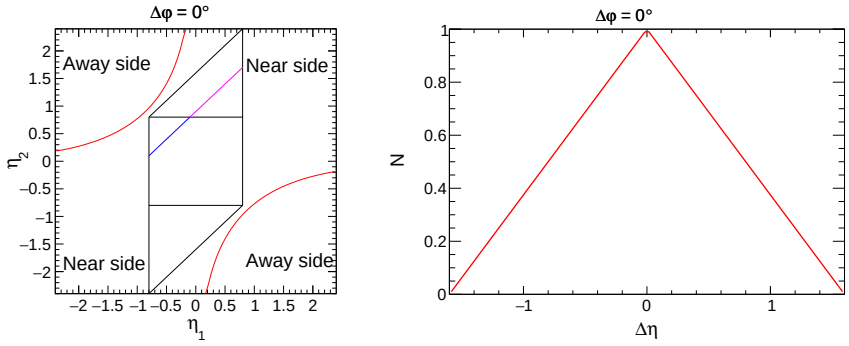

FIGURE 32 *Left:* Illustration on how the acceptance triangle is calculated in the traditional case. The black box in the middle is the acceptance of the detector. Assuming that the trigger particle hits the acceptance and $\Delta\eta < 1.6$, the associated particles can be found from the areas of the black triangles. The probability for an associated particle to be inside the acceptance is proportional to the length of the blue line and the probability for it to be outside of the acceptance is proportional to the length of the magenta line. *Right:* Traditional acceptance triangle.

distribution because they are left to the away side are different from the particles that we do not see because they are outside of the acceptance. They are not in the near side distribution because they are categorized as away side pairs, not because we fail to see them. Thus we should not correct for the particles that go to the away side. Now the definition of the acceptance triangle in 3D near side will be the probability to see the associated particle inside the acceptance, provided that the trigger particle is inside the acceptance *in the near side*.

If we look at the formula for the acceptance triangle in 3D near side, it is the same as for the traditional near side but with one notable exception, $P(\text{inside}) + P(\text{outside})$ is not necessarily 1 anymore

$$\text{Acc}_{\triangle} = \frac{P(\text{inside})}{P(\text{inside}) + P(\text{outside})} \,. \tag{45}$$

This is because now there is an additional component $P(\text{away})$ to the total probability which stands for trigger hitting the acceptance, but associated particle going to the away side. This point becomes clearer if you look at the left hand side plot of Figure 33. If we write the equation for the acceptance triangle in terms of lengths of the lines, we get the same equation (43) as in the traditional case. Now depending on the values of $\Delta\eta$ and $\Delta\varphi$, there might be additional component to the line that corresponds to $P(\text{away})$. This is illustrated in the figure by the cyan line. As the length of the cyan line may change from one occasion to another but the total length of the line is always the same, the proportions of blue and magenta line also change. This must be taken into account when the acceptance correction is calculated. What this means for the acceptance triangle is shown in the right hand plot of the same figure. We can see that the edges of the acceptance triangle are truncated.

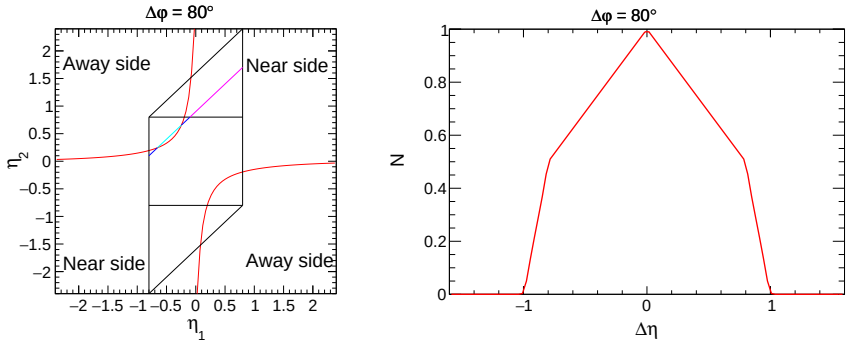

FIGURE 33 *Left:* Illustration on how the acceptance triangle is calculated for 3D near side. The black box in the middle is the acceptance of the detector. Assuming that the trigger particle hits the acceptance and $\Delta\eta < 1.6$, the associated particles can be found from the areas of the black triangles. The probability for an associated particle to be inside the acceptance is proportional to the length of the blue line and the probability for it to be outside of the acceptance is proportional to the length of the magenta line. The length of the cyan line is proportional to the probability that the associated particle is inside the acceptance, but is categorized to be in the away side. *Right:* Truncated acceptance triangle.

The length of the line on the away side (proportional to $P(\text{away})$) can be calculated analytically by solving the following equation pair:

$$\begin{cases} \eta_1 = -\ln\left[\tan\left[\dfrac{\arctan\left(\dfrac{-\cos\left(2\arctan(e^{-\eta_2})\right)}{\sin\left(2\arctan(e^{-\eta_2})\right)\cos(\Delta\varphi)}\right)}{2}\right]\right] \\ \eta_1 = \Delta\eta + \eta_2 \end{cases} \tag{46}$$

Here the first equation is the near-away side boundary given by equation (41) and the second equation is a constant $\Delta\eta$ line. When we solve the equation pair for η_2, we get the solution as a function of $\Delta\eta$ and $\Delta\varphi$. Depending on the values of $\Delta\eta$ and $\Delta\varphi$, there might be 0, 1 or 2 roots for this function. An example with zero roots is shown in the left hand side plot Figure 32 and an example with two roots on the left hand side plot of the Figure 33. In this analysis this pair of equations is solved numerically.

As the acceptance correction depends on both $\Delta\eta$ and $\Delta\varphi$, we can see the complete picture by making a 2D plot over the whole observed $(\Delta\eta,\Delta\varphi)$ space. This is done in Figure 34. The emerging shape looks a lot like Sauron's eye from the Lord of the Rings movie series.

Finally, let us take a look on the mixed event distributions in the 3D near side. As in the traditional case, the mixed event distribution will be proportional to the probability to see the associated particle inside the acceptance $P(\text{inside})$. In the traditional case this is directly proportional to the acceptance triangle, as can be seen from equation (42). But in the 3D near side this is not true, since

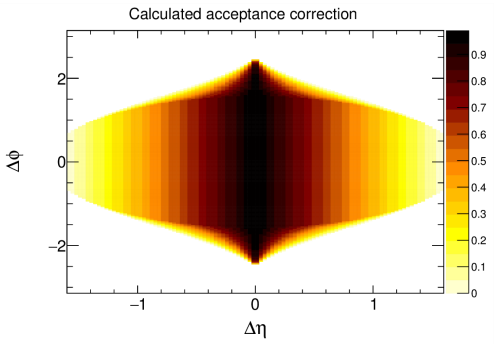

FIGURE 34 Calculated 3D near side acceptance correction over the whole $(\Delta\eta,\Delta\varphi)$ space. The distribution has a shape like "Sauron's eye".

the denominator of that equation is not constantly 1 anymore. Thus we need to use the form given in equation (45). This fact explains why we cannot simply normalize the mixed event distribution to one: the denominator is different in different areas of the phase space. We need to take this into account when we do the normalization.

To do the correction, we need to know the probability that the associated particle is in the near side, but outside of the acceptance. It turns out that this is easy to calculate. Take a look at the constant $\Delta\eta$ line in Figure 33. Because of symmetry of the near-away side boundary given by equation (41), if the length of the blue part of the constant $\Delta\eta$ line is larger than 0, the magenta part will be always completely in the near side. This allows us to calculate the length of the magenta line (proportional to the probability we're after) as

$$L(\text{outside}) = \sqrt{\Delta\eta^2 + \Delta\eta^2} = \sqrt{2}\Delta\eta \ . \tag{47}$$

You can see this by looking at the left hand side plot in Figure 32 or Figure 33. In the right-angled triangle formed by magenta line as hypotenuse and black lines as legs the length of each leg is $\Delta\eta$. Thus the length of the hypotenuse will be given by equation (47). To be able to make a correct calculation using the values given by equation (47), the mixed event distributions need to be normalized first. The maximum value after the normalization should correspond to the maximum possible length of the line inside the acceptance. This we can get by calculating the length of the diagonal of the black square in Figure 32 or Figure 33. From the Pythagorean theorem we get that this is $\sqrt{2}\Delta\eta_{\text{max}}$. Doing this normalization gives us the distribution of the lengths of lines inside the acceptance. To get the correction, we just do the calculation in equation (43) using equation (47) to get the length of the line outside of acceptance.

Let's check that this approach works in practice. The distribution of the lengths of lines inside the acceptance (proportional to the probability that the associated particle is inside the acceptance) from calculations is shown in Figure 35 together with the calculated acceptance correction. We should get a distribution similar to the right hand side plot in this figure from the mixed event distributions. Examples of mixed event distributions in different $x_{\parallel}$ bins are shown in Figure 36.

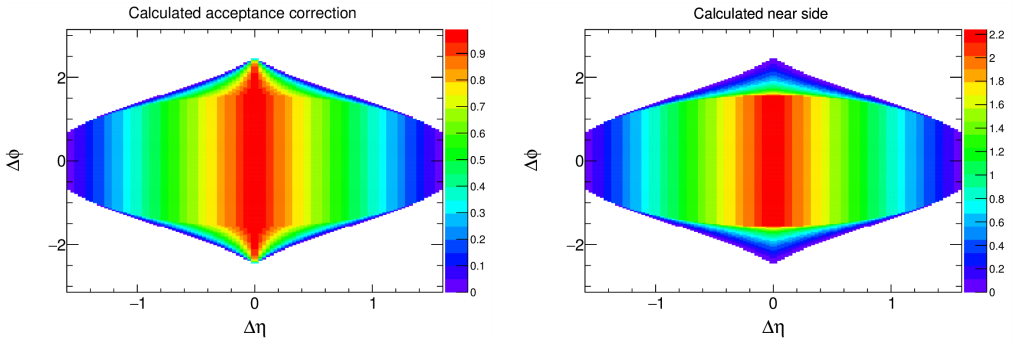

FIGURE 35 *Left:* Calculated acceptance correction for 3D near side. *Right:* Probability to see a particle pair with given values of $\Delta\eta$ and $\Delta\varphi$.

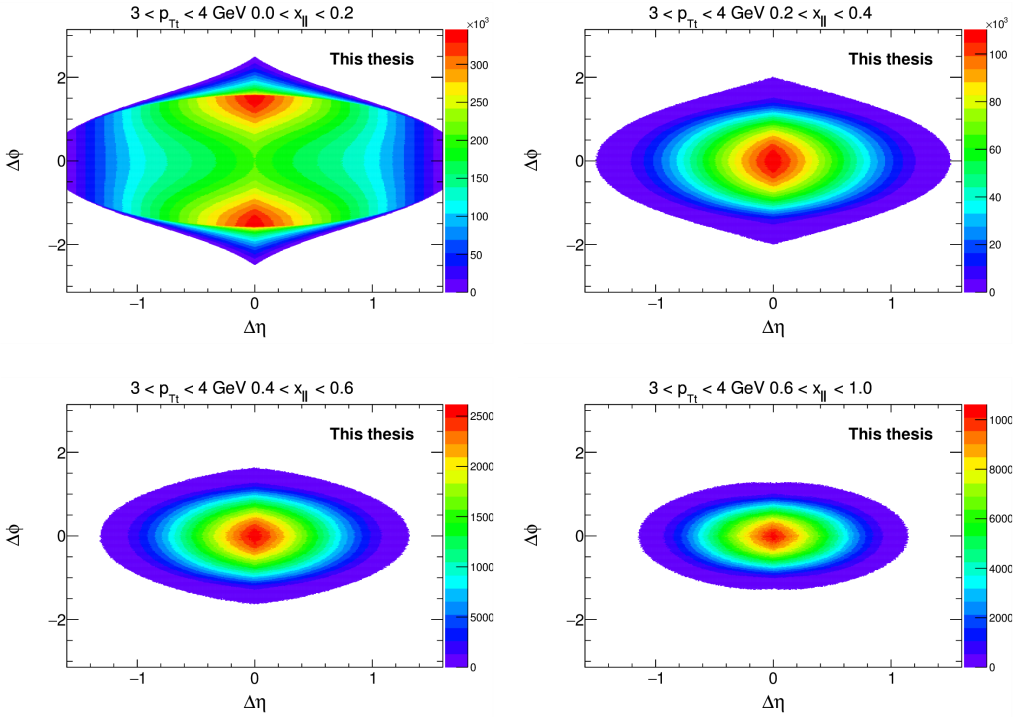

FIGURE 36 Examples of mixed event distributions in different $x_{||}$ bins. The $x_{||}$ binning biases strongly the mixed event distribution.

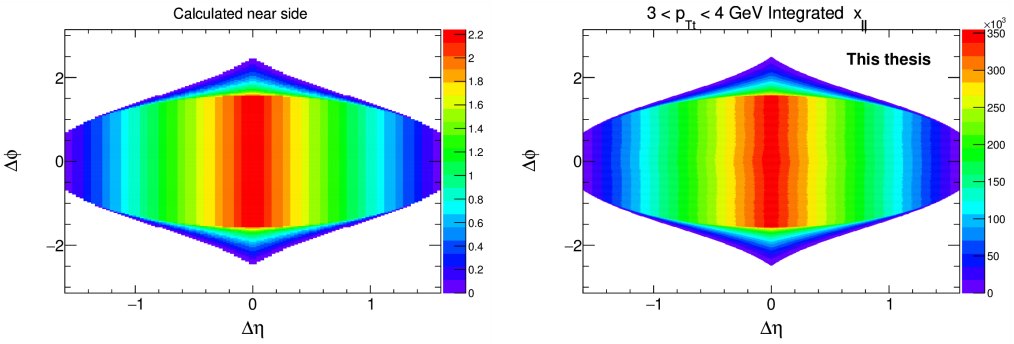

FIGURE 37 *Left:* Probability to see a particle pair with given values of $\Delta\eta$ and $\Delta\varphi$. *Right:* Mixed event distribution integrated over the $x_{||}$ bins.

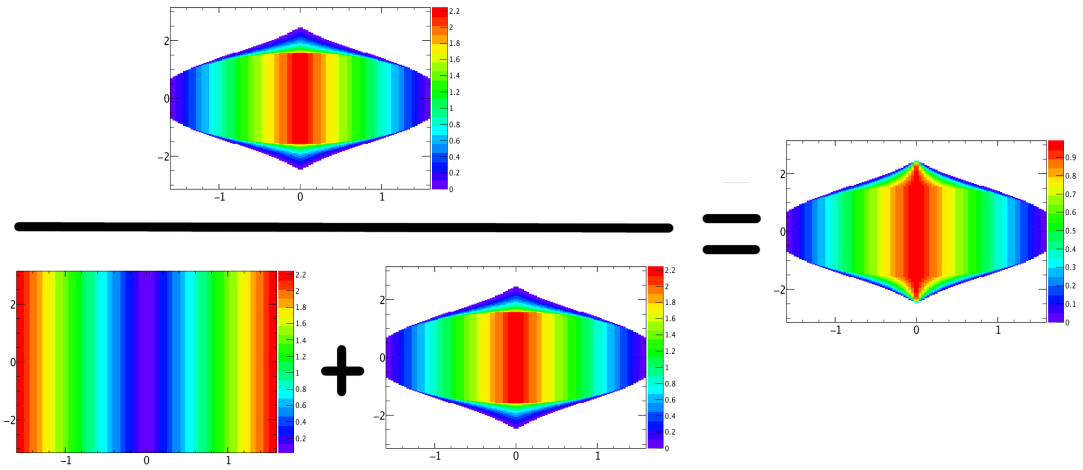

FIGURE 38 The method of getting the acceptance correction out of the mixed event distributions.

From this figure we see that the $x_{\parallel}$ binning strongly biases the mixed event distribution. The larger the $x_{\parallel}$, the closer to the trigger particle the associated particle wants to be. To remove this bias, we need to integrate over the $x_{\parallel}$ bins. You can see the comparison of the calculation and integrated mixed event distribution in Figure 37. When the $x_{\parallel}$ bins are integrated over, these two distributions agree very well with each other.

What remains to be checked is that we can regain the "Sauron's eye" shape using the distribution in Figure 37 as the line length inside the acceptance (probability that the associated particle is inside the acceptance) and the result given by equation (47) as the line length outside the acceptance (probability that the associated particle goes outside of the acceptance) and plugging them into equation (43). This is done in the Figure 38. Everything seems to work nicely, so the method described above can indeed be used to get the acceptance correction out of the mixed event distributions for the 3D near side.

4.5 Di-gluon PYTHIA

The goal of this analysis is to extract distinct j_{T} components for hadronization and QCD showering. Before looking at the real data, it was studied if this distinction is possible to make in a PYTHIA 8 simulation. An idealized system was chosen for this study to see the hadronization and showering components from the simulation as cleanly as possible. The simulation was setup in such a way, that the primary collision always produced an artificial resonance state which immediately decayed into two gluons. There is still some probability that one (or both) of the gluons experiences an early hard splitting leading into more than two jets in the final state, but most of the events produced by this simulation are ideal di-jet events.

In PYTHIA 8 the final state QCD shower is modeled as a timelike shower, as explained in Section 1.4.1. This showering process continues until a defined cut-off scale is reached, after which the partons are hadronized with the Lund string fragmentation model [106]. In the simulation we can disable the showering algorithm, forcing the partons to hadronize without going through the showering phase. This gives the component coming only from Lund string fragmentation. Based on equation (21), this component is expected to be Gaussian. It is possible to also disable the string fragmentation algorithm, but that we do not want to do since we want to see the final state particles. Thus we have chosen to study the part of the spectrum produced by the showering algorithm by subtracting the distribution where the showering is disabled from the distribution where it is enabled. When the peak coming from the fragmentation is removed, we see the showering tail that is left over.

The results from the study described above are presented in Figure 39. The red histogram in the figure shows the distribution when final state radiation is not allowed. It can be seen that the distribution is nearly Gaussian, but with a small tail. The black histogram is obtained when the final state radiation is turned

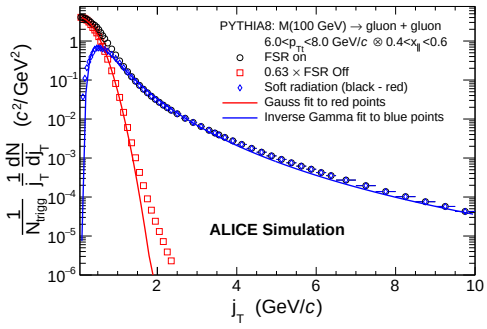

FIGURE 39 Results from PYTHIA 8 study with a di-gluon initial state. Black distribution is obtained when the final state radiation is on. When the final state radiation is turned off, the red distribution emerges. Blue one is calculated by subtracting the red from the black.

back on. There is still a Gaussian peak at small j_T but a long tail develops at larger j_T. To find the QCD showering part of the distribution, it is assumed that the hadronization is the dominant component at low j_T. The only hadronization distribution is scaled such that the ratio of red and black histograms is unity at $j_T = 0$. Without this scaling the red histogram would be higher than the black. The hadronization peak shrinks when the QCD radiation is turned on because now some of the virtuality of the leading particle is radiated to wider angles. When the leading parton hadronizes, is has thus smaller virtuality and can thus produce fewer particles, resulting in smaller peak. After the scaling the red histogram is subtracted from the black one to obtain the blue histogram, which now describes only the QCD showering part of the distribution in PYTHIA 8.

This study shows that the separation of the showering and hadronization parts of the jet fragmentation is clear in PYTHIA 8. To also look for two components in the real data, good fits were determined for hadronization and showering. The best fit functions we found are Gaussian function for the hadronization histogram and an inverse gamma function for the showering histogram. When writing the functional forms for these, we must take into account that we are measuring the length of a two dimensional vector. Thus we have chosen to express the functions in a polar coordinate system. We assume that the underlying two dimensional distribution is cylinder symmetric, meaning

$$\frac{\mathrm{d}^2N}{\mathrm{d}j_{\mathrm{Tx}}\mathrm{d}j_{\mathrm{Ty}}} = \frac{\mathrm{d}^2N}{j_{\mathrm{T}}\mathrm{d}j_{\mathrm{T}}\mathrm{d}\varphi} = \frac{\mathrm{d}N}{2\pi j_{\mathrm{T}}\mathrm{d}j_{\mathrm{T}}} \,. \tag{48}$$

Two dimensional Gaussian function is a product of two one dimensional Gaussian functions

$$\left.\frac{\mathrm{d}^2N}{\mathrm{d}j_{\mathrm{Tx}}\mathrm{d}j_{\mathrm{Ty}}}\right|_{\mathrm{Gauss}} = \frac{1}{2\pi\sigma_x\sigma_y}\, e^{-\left(\frac{j_{\mathrm{Tx}}^2}{2\sigma_x}+\frac{j_{\mathrm{Ty}}^2}{2\sigma_y}\right)} = \frac{1}{2\pi\sigma^2}\, e^{-\frac{j_{\mathrm{Tx}}^2+j_{\mathrm{Ty}}^2}{2\sigma^2}} \,, \tag{49}$$

where in the last equality cylinder symmetry $\sigma_x = \sigma_y = \sigma$ is assumed. In polar

coordinates this can be expressed as

$$\frac{1}{j_\mathrm{T}}\frac{\mathrm{d}N}{\mathrm{d}j_\mathrm{T}}\bigg|_\mathrm{Gauss} = \frac{1}{\sigma^2}\, e^{-\frac{j_\mathrm{T}^2}{2\sigma^2}} \,. \tag{50}$$

Notice that this functional form is properly normalized $\int_0^\infty \frac{\mathrm{d}N}{\mathrm{d}j_\mathrm{T}}\mathrm{d}j_\mathrm{T} = 1$. Similarly, we can obtain the following formula for the normalized inverse gamma function

$$\frac{1}{j_\mathrm{T}}\frac{\mathrm{d}N}{\mathrm{d}j_\mathrm{T}}\bigg|_\mathrm{Inverse\ Gamma} = \frac{a^{b-1}}{\Gamma(b-1)}\,\frac{e^{-\frac{a}{j_\mathrm{T}}}}{j_\mathrm{T}^{b+1}} \,, \tag{51}$$

where $b > 2$ is required for the function to be well defined. For the real data, these will be called the narrow and wide component respectively.

4.6 Fitting j_T distribution

Now that we know how to construct the distribution and estimate the background, what kind of corrections need to be applied and have an idea how the signal should look like, we can take the j_T distribution and fit it. In the fit the background estimate is combined with the estimates for the signal shapes for the two components. The fit function becomes

$$\begin{gathered}\text{Constant} \times \text{background} + \text{Gauss} + \text{Inverse Gamma} \\ B_0 \times \text{background} + \frac{B_2}{B_1^2}\, e^{-\frac{j_\mathrm{T}^2}{2B_1^2}} + \frac{B_3 B_5^{B_4-1}}{\Gamma(B_4-1)}\frac{e^{-\frac{B_5}{j_\mathrm{T}}}}{j_\mathrm{T}^{B_4+1}} \,,\end{gathered} \tag{52}$$

where $B_{0\ldots5}$ are fit parameters. Here it is good to notice that the shape of the background does not change from the one that the background estimation method gives, only the normalization is determined by the fit. More important is to notice that in this function it is assumed that the two j_T components are additive. This is not true in a general case, since QCD branching and hadronization are not two decoupled phenomena. The two distributions can be folded together. However, now we are considering only events where there is a high-p_T trigger particle around which the jet is formed. As sufficiently high-p_T partons radiate soft gluon radiation before they hadronize, the energy lost by the gluon emission is small compared to the original energy of the partons and the direction of their propagation is not changed much. Thus the high-p_T partons hadronize almost as if they would have suffered no final state radiation at all. Also as a high-p_T trigger particle is likely to take a large fraction of the initial momentum of the parton (it is a large z particle), the originating parton is likely to radiate less other particles compared to low z particles [158]. Thus there should not be many low momentum particles to fold the two distributions together. Based on this reasoning, we approximate that the contributions from showering and hadronization parts can be treated as a simple sum.

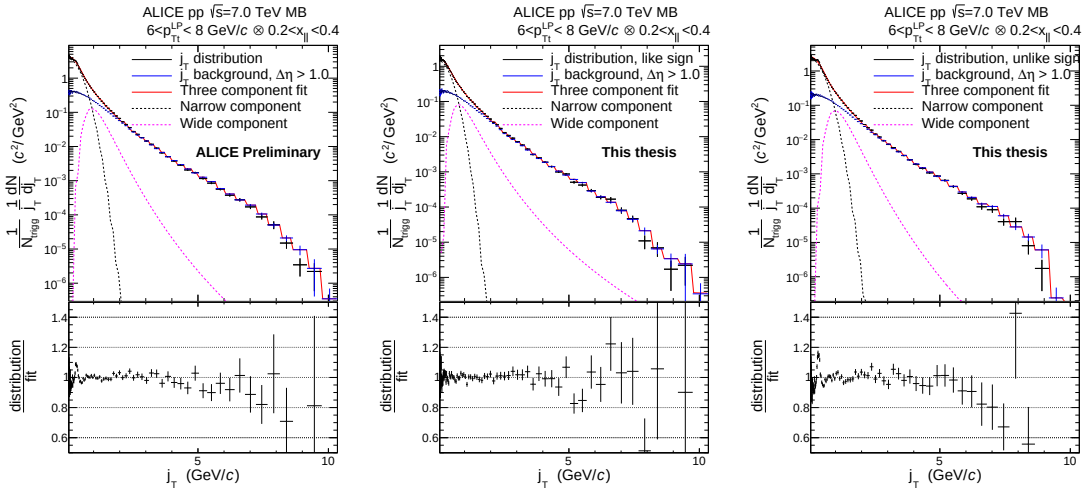

FIGURE 40 *Left:* Measured j_{T} distribution with a three component fit into it. The three components describe the background (blue), hadronization (black dashed) and showering (magenta). *Middle:* Measured j_{T} distribution for like sign pairs. *Right:* Measured j_{T} distribution for unlike sign pairs.

An example how the fit function in equation (52) manages to fit the measured j_{T} distribution is shown in the leftmost plot of Figure 40. In this plot the black histogram is the measured j_{T} distribution, containing both signal and the background. The blue histogram is the estimated background, where the normalization is given from the fit. Black dashed line is the Gaussian fit component and magenta dashed line the inverse gamma fit component. It can be seen from the distribution to fit ratio that the three component fit manages to describe the distribution really well over a wide j_{T} range. Only around $j_{\mathrm{T}} \sim 0.4$ GeV/c there is a small bump in the distribution to fit ratio.

We can start to investigate the origin of the bump by looking at the like and unlike sign j_{T} distributions. Like sign distribution is constructed out of pairs having the same charge ($++$ or $--$) and the unlike sign distribution out of the pairs having opposite charges ($-+$ or $+-$). The like sign distribution is shown in the middle plot of Figure 40. It can be seen that the bump vanished in this case. On the other hand, the bump is enhanced for the unlike sign distribution in the rightmost plot of Figure 40. These observations suggest that the bump might originate from particle decays after the hadronization.

Particles that decay after the hadronization but before hitting the detector can be one source of the background, since correlations resulting from the decays cannot be attributed to hadronization or QCD showering, which are the two measured components in this analysis. The invariant mass of a decaying particle pair assuming massless products is

$$M = \sqrt{2|\vec{p}_{\mathrm{t}}||\vec{p}_{\mathrm{a}}|(1-\cos\theta)}\,, \tag{53}$$

where θ is the angle between the trigger particle and the associated particle. If we write the definition of j_{T} from equation (30) using the angle θ rather than cross

product notation, it becomes

$$j_{\mathrm{T}} = |\vec{p}_{\mathrm{a}}| \sin\theta \, . \tag{54}$$

We can see from equations (53) and (54) that the invariant mass of the decaying pair is closely correlated to j_{T}. This could cause a bump as seen in Figure 40. It would also explain the like sign and unlike sign distributions. We are only measuring charged particles, so in order for the extra correlation to be visible in the measured distributions we need to find a pair of trigger and associated particles that are both charged decay products. The vast majority of particles produced have charges $-e$, 0, or e, where e is the elementary charge. In order to have a non-negligible component from a particle decay, the decaying particle needs to be neutral and decay into a pair with charges $-e$ and e.

Further evidence for this was sought from a PYTHIA 8 study. In PYTHIA simulation we know the history of the particles from the hadronization to the end of the simulation. Thus we can select as trigger only particles that did not decay after the hadronization. This way we avoid correlating two particles coming from another short lived particle. The results of this PYTHIA 8 study are shown in Figure 41. The schematic pictures on the left side of the figure illustrate events with stable and unstable triggers. In the top illustration the trigger particle is the π^+ going to the right and the red arrows connect the trigger with each associated particle in the event. In the bottom illustration the trigger is again the right-going π^+, but this time it is coming from the ρ^0 decay instead of directly from hadronization. When this is paired with the π^- coming also from the decay, we are not probing the fragmentation anymore, but the decay of ρ^0. The j_{T} distribution in the middle of the figure corresponds to regular data taking, where we cannot distinguish between stable and unstable triggers. It can be seen that also in the PYTHIA 8 simulation the bump around $j_{\mathrm{T}} \sim 0.4$ GeV/c appears. However, when we select only triggers that are stable after the hadronization, we get the distribution on the right side of the figure. Now the bump disappears and the fit agrees really well with the distribution over the whole j_{T} range.

We can compare the stable trigger distribution from PYTHIA 8 to the distribution with all triggers to see if the effect of the neutral meson decays is fully concentrated in the bump. This comparison is shown in Figure 42. Here we can see that the effect is much wider than the narrow peak that is clearly visible in the distribution. Depending a bit on the $x_{\parallel}$ bin, approximately the region $j_{\mathrm{T}} < 2$ GeV/c has a clear difference in the shape. Thus just fitting a smooth function below the bump will not be enough to take this effect into account.

We are not aware of a good data driven way to remove the cases where the trigger particle is a decay product from the real data. An invariant mass cut cannot be used, because as can be seen from equations (53) and (54) it is too closely correlated with j_{T}. A cut would not only cut out the resonances, but a big part of the regular distribution. Another method that was thought of was to use a template from PYTHIA to fit and remove the resonance contribution, but we decided against using this since in this case we felt that we would be relying too much on simulations. Thus a decision is made to leave the contribution from decaying resonances to the final j_{T} distributions and take their effect into account in the evaluation of the systematic uncertainties.

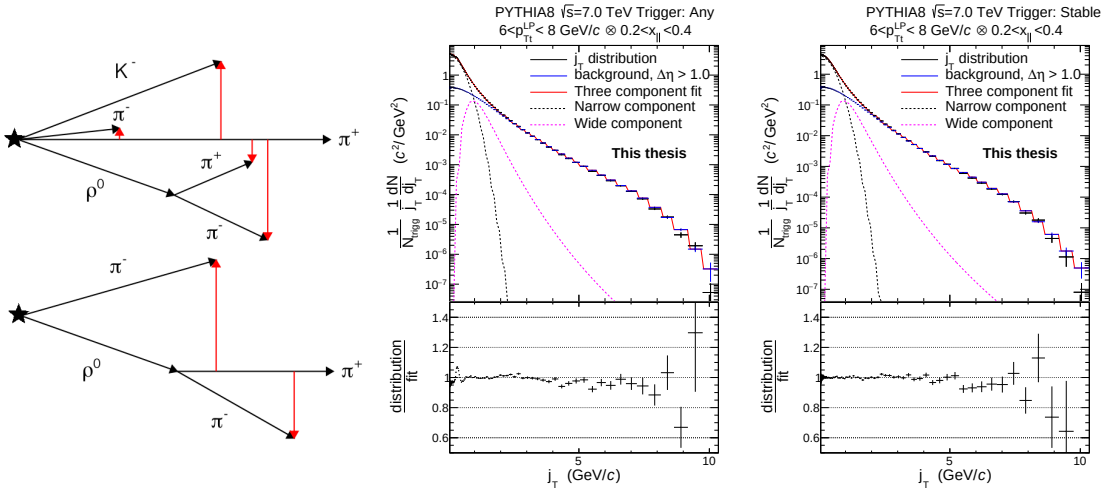

FIGURE 41 *Left:* Schematic illustration of an event with a stable trigger (top) and an unstable trigger (bottom). *Middle:* j_{T} distribution from PYTHIA 8 accepting both stable and unstable particles as triggers. *Right:* j_{T} distribution from PYTHIA 8 accepting only stable particles as triggers.

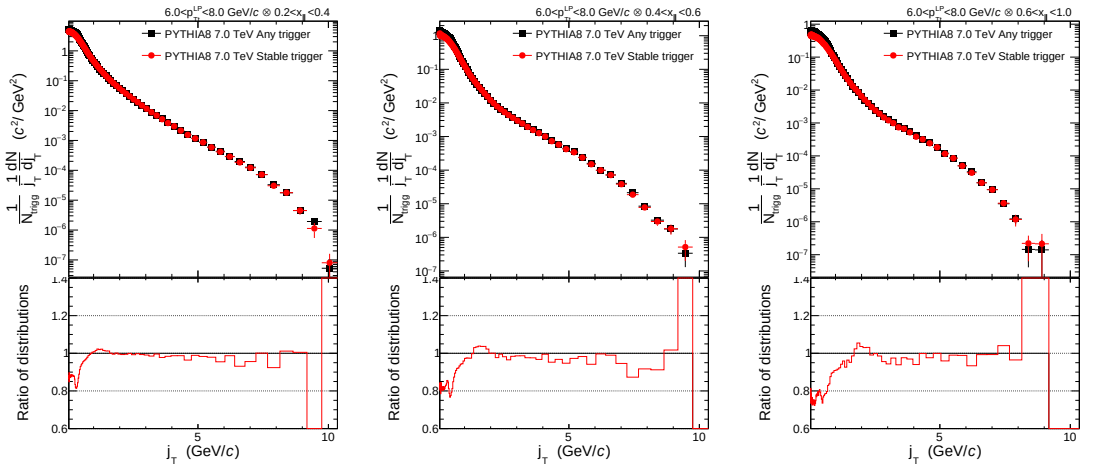

FIGURE 42 Comparison of a regular PYTHIA 8 run with a run where only stable triggers are selected. In the ratio it can be seen that the shape of the distribution is distorted from much larger region than just the small bump.

4.7 Extracting $\sqrt{\langle j_{\mathrm{T}}^2 \rangle}$ and per trigger yield

The final goal of the analysis is to extract the root-mean-square (RMS) and yield values from the j_{T} distribution. These are calculated from the fit parameters of the fit function (52).

The yield is defined to be the number N in the background subtracted $\frac{1}{N_{\mathrm{trigg}}} \frac{1}{j_{\mathrm{T}}} \frac{\mathrm{d}N}{\mathrm{d}j_{\mathrm{T}}}$ distribution. This can be obtained by integrating the distribution over all space. Assuming cylinder symmetry, we can use the result in equation (48) to obtain

$$\begin{aligned} \frac{N}{N_{\mathrm{trigg}}} &= \frac{1}{N_{\mathrm{trigg}}} \int_{-\infty}^{\infty} \int_{-\infty}^{\infty} \frac{\mathrm{d}^2 N}{\mathrm{d}j_{\mathrm{Tx}} \mathrm{d}j_{\mathrm{Ty}}} \mathrm{d}j_{\mathrm{Tx}} \mathrm{d}j_{\mathrm{Ty}} \\ &= \frac{1}{N_{\mathrm{trigg}}} \int_0^{\infty} \int_0^{2\pi} \frac{\mathrm{d}N}{2\pi j_{\mathrm{T}} \mathrm{d}j_{\mathrm{T}}} \, j_{\mathrm{T}} \, \mathrm{d}\varphi \, \mathrm{d}j_{\mathrm{T}} \\ &= \frac{1}{N_{\mathrm{trigg}}} \int_0^{\infty} \frac{1}{j_{\mathrm{T}}} \frac{\mathrm{d}N}{\mathrm{d}j_{\mathrm{T}}} \, j_{\mathrm{T}} \, \mathrm{d}j_{\mathrm{T}} \, . \end{aligned} \tag{55}$$

Here it is useful to notice that the distribution we fit is a $\frac{1}{N_{\mathrm{trigg}}} \frac{1}{j_{\mathrm{T}}} \frac{\mathrm{d}N}{\mathrm{d}j_{\mathrm{T}}}$ distribution. Thus for the Gauss part of the distribution, we can calculate the per trigger yield as

$$\frac{Y_{\mathrm{Gauss}}}{N_{\mathrm{trigg}}} = \int_0^{\infty} j_{\mathrm{T}} \, \frac{B_2}{B_1^2} \, e^{-\frac{j_{\mathrm{T}}^2}{2B_1^2}} \, \mathrm{d}j_{\mathrm{T}} = B_2 \, . \tag{56}$$

For inverse gamma function we get

$$\frac{Y_{\mathrm{InvGamma}}}{N_{\mathrm{trigg}}} = \int_0^{\infty} j_{\mathrm{T}} \, \frac{B_3 B_5^{B_4 - 1}}{\Gamma(B_4 - 1)} \frac{e^{-\frac{B_5}{j_{\mathrm{T}}}}}{j_{\mathrm{T}}^{B_4 + 1}} \, \mathrm{d}j_{\mathrm{T}} = B_3 \, . \tag{57}$$

The results are hardly surprising, since the fit function (52) is constructed from the normalized functions (50) and (51). The errors of the yield are simply the errors of fit parameters B_2 and B_3 given by the fitting procedure.

The mean for a random variable x following a probability density function $P(x)$ is [159]:

$$\langle x \rangle = \int x \, P(x) \mathrm{d}x \, . \tag{58}$$

To transform any function $f(x)$ having the property $0 \leq f(x) < \infty$ to a probability density function in an interval where the above condition holds, we need to normalize $f(x)$ with its integral over the given interval. Thus for such a function $f(x)$ we can define the root-mean-square value as:

$$\sqrt{\langle x^2 \rangle} = \sqrt{\frac{\int x^2 f(x) \, \mathrm{d}x}{\int f(x) \, \mathrm{d}x}} \, . \tag{59}$$

For the j_T distribution the mean of squares becomes

$$\left\langle j_\mathrm{T}^2 \right\rangle = \frac{\int_0^\infty j_\mathrm{T}^2 \, \frac{\mathrm{d}N}{\mathrm{d}j_\mathrm{T}} \, \mathrm{d}j_\mathrm{T}}{\int_0^\infty \frac{\mathrm{d}N}{\mathrm{d}j_\mathrm{T}} \, \mathrm{d}j_\mathrm{T}} = \frac{\int_0^\infty j_\mathrm{T}^3 \, \left(\frac{1}{j_\mathrm{T}} \, \frac{\mathrm{d}N}{\mathrm{d}j_\mathrm{T}} \right) \, \mathrm{d}j_\mathrm{T}}{\int_0^\infty j_\mathrm{T} \left(\frac{1}{j_\mathrm{T}} \, \frac{\mathrm{d}N}{\mathrm{d}j_\mathrm{T}} \right) \, \mathrm{d}j_\mathrm{T}} \, , \tag{60}$$

where the form $\frac{1}{j_\mathrm{T}} \, \frac{\mathrm{d}N}{\mathrm{d}j_\mathrm{T}}$ is highlighted since this is the form of the measured j_T distribution. The denominator is just the yield that has already been calculated, so the only thing left to get the RMS is to calculate the integral for the numerator.

For the Gaussian function the RMS becomes

$$\sqrt{\left\langle j_\mathrm{T}^2 \right\rangle}_\mathrm{Gauss} = \left(\frac{1}{B_2} \, \int_0^\infty j_\mathrm{T}^3 \, \frac{B_2}{B_1^2} \, e^{-\frac{j_\mathrm{T}^2}{2B_1^2}} \, \mathrm{d}j_\mathrm{T} \right)^{\frac{1}{2}} = \sqrt{2} B_1 \, , \tag{61}$$

and the final result for the inverse gamma function is

$$\sqrt{\left\langle j_\mathrm{T}^2 \right\rangle}_\mathrm{Inverse\ Gamma} = \left(\frac{1}{B_3} \, \int_0^\infty j_\mathrm{T} \, \frac{B_3 B_5^{B_4-1}}{\Gamma(B_4-1)} \frac{e^{-\frac{B_5}{j_\mathrm{T}}}}{j_\mathrm{T}^{B_4+1}} \, \mathrm{d}j_\mathrm{T} \right)^{\frac{1}{2}} = \frac{B_5}{\sqrt{(B_4-2)(B_4-3)}} \, , \tag{62}$$

where it is required that $B_4 > 3$. The errors for these are obtained by adding the errors for single fit parameters together in quadrature, taking into account the possible correlations between the parameters. In a general form the error formula reads

$$\delta f(x_1, \ldots, x_n) = \sqrt{\sum_{i=1}^{n} \left(\frac{\partial f}{\partial x_i} \delta x_i \right)^2 + 2 \sum_{\substack{i,j=1 \\ i<j}}^{n} \mathrm{cov}(x_i, x_j) \frac{\partial f}{\partial x_i} \frac{\partial f}{\partial x_j}} \, , \tag{63}$$

where $\mathrm{cov}(x_i, x_j)$ is the covariance between the parameters x_i and x_j. The errors of fit parameters and their covariances are given by the fitting procedure.

To see that the derived formulas give results that are of the correct order, some sanity checks were performed. In the sanity checks the RMS and per trigger yield for the signal histogram were obtained from bin counting. To get the RMS directly from the bins of the histogram, we need to remember that we are calculating it for a two dimensional vector. Assuming cylinder symmetry, we can transform the one dimensional histogram into a two dimensional one by rotating it around the origin. In principle this was done by weighting the content of each bin with the area of the corresponding disc that would be formed in such a rotation. It was found out that the relation

$$\sqrt{\left\langle j_\mathrm{T}^2 \right\rangle}_\mathrm{narrow} < \sqrt{\left\langle j_\mathrm{T}^2 \right\rangle}_\mathrm{bin\ counting} < \sqrt{\left\langle j_\mathrm{T}^2 \right\rangle}_\mathrm{wide} \tag{64}$$

always holds, as it should.

For the yields the sum of narrow and wide yields was compared to the yield obtained from bin counting. When calculating the yield from bin counting, the

content of each bin was multiplied by the value of j_T in the middle of the bin to get rid of the $\frac{1}{j_T}$ factor in the measured distribution. It was found out that the difference between fit and bin counting is smaller than 1 % in most cases, and also in the worst statistics bin this is approximately 3 %. These sanity checks give confidence that the formulas derived above provide reasonable results for the analysis.

5 SYSTEMATIC UNCERTAINTIES

The evaluation of systematic uncertainties is one of the most important and difficult tasks in experimental physics. In this analysis the systematic uncertainties are evaluated by identifying points in the analysis, where different choices could have meaningfully be made. If these choices show non-negligible systematic difference in the results for which we cannot give a good explanation, this difference will be assigned as a systematic uncertainty. In practice this is done by first obtaining the final RMS and yield results using the different choices inside the analysis. Then a ratio of the final results is taken, which is fitted to suppress possible statistical fluctuations and to better catch systematic trends. An example of the fitting procedure is presented in Figure 43. This figure contains the three different fits, that are used in the analysis. The first option is to fit a zeroth order polynomial, as shown in the left plot in Figure 43. If the ratio shows a linear p_{Tt} dependence, also first order polynomial can be used, as is done in the middle plot. If the p_{T} dependence is not clearly constant or linear, a combination of first and zeroth order polynomials can be made in different ranges of the ratio, as shown in the right hand side plot. No more that two different ranges are used to ensure that each fit has at least three points. Also no polynomials higher than first order are used in the analysis.

Three main sources of systematic uncertainty in the analysis are background evaluation, signal fitting and tracking. The first two are common for data and simulations, but in the simulations there is no uncertainty due to tracking. We know exactly all the particles that are produced in PYTHIA and Herwig.

5.1 Background

The first source of uncertainty for the background estimation is the way the randomization is done when extrapolating the background to the signal region. As explained in Section 4.2 we use η-gap method as a standard background estimate and R-gap for systematic uncertainty estimation. As azimuthal angle modulations are expected to be small for pp and p–Pb collisions in the kinematic

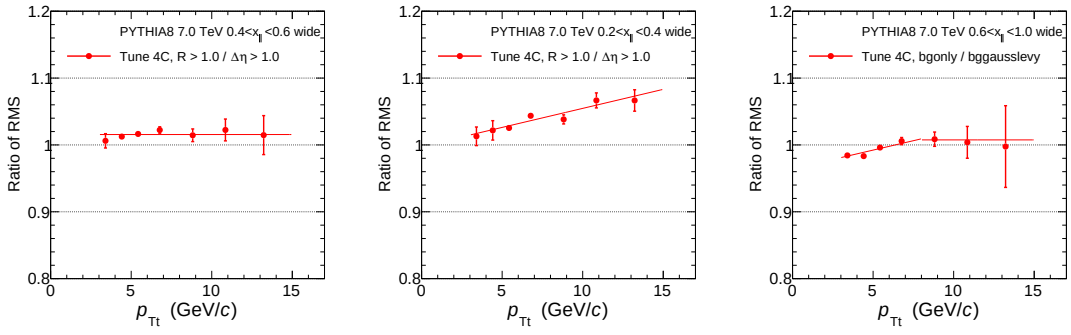

FIGURE 43 Examples on how systematic uncertainties are evaluated from ratios of final results following different choices. These examples are from a standalone PYTHIA 8 simulation. *Left:* Ratio plot with a zeroth order polynomial fitted into it. *Middle:* Ratio plot with a first order polynomial fitted into it. *Right:* Ratio plot with zeroth and first order polynomials fitted to different ranges.

range of this analysis, both of the two randomization methods should give the same result. If the analysis is later expanded to Pb–Pb data, R-gap should not be used for systematic uncertainty estimation since there large azimuthal angle modulations are expected due to hydrodynamic flow [47,155,156]. In the overview plots this source is referred as "randomization".

The second source that was checked from the background is the size of the η-gap above which all the particles are assumed to be coming from the background. Here two other values are compared to the standard gap $\Delta\eta > 1$, namely $\Delta\eta > 0.8$ and $\Delta\eta > 1.2$. All these gaps should be large enough that the jet correlations are dominantly at smaller angles. When the size of the gap is increased, we lose statistics from the background since it is generated from fewer pairs. This is the limiting factor to go to gaps larger than $\Delta\eta > 1.2$. This source will be referred as "gapSize" in the overview plots.

Finally the number of new pairs generated from a background pair to extrapolate the background was varied. As comparison to standard 20 pairs, 15 or 25 pairs were tested. Here the differences in the final results resulting from different number of pairs were negligible in all checked bins, so this does not contribute for any uncertainty for the final results.

5.2 Fitting methods

As explained in Section 4.6, the j_T distribution is fitted with the background estimate together with Gaussian and inverse gamma functions for narrow and wide j_T components in a single fit. Thus signal and background scale are determined simultaneously. We can also take a different approach and assume that the tail of the measured j_T distribution is dominated by background particles. This should be good approximation, since as mentioned earlier in this thesis, the jet correlations

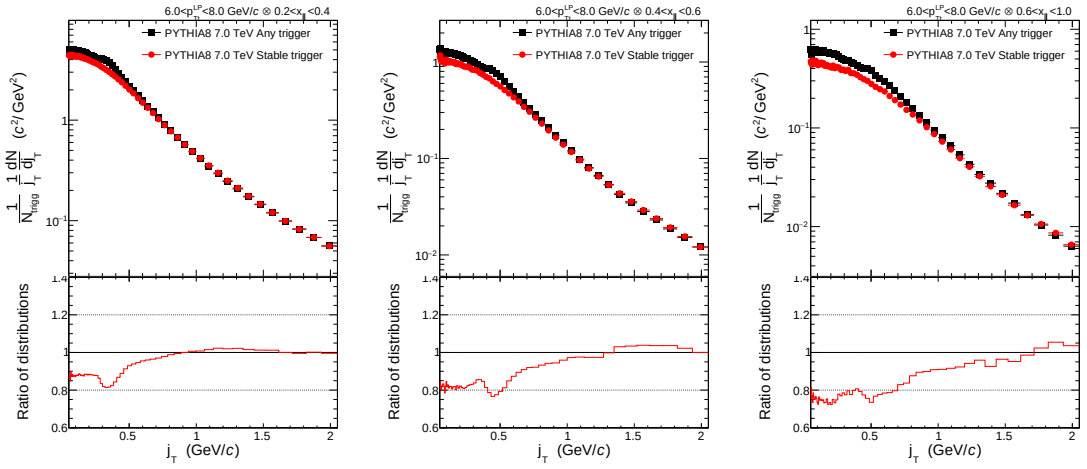

FIGURE 44 Comparison of a regular PYTHIA 8 run with a run where only stable triggers are selected, zoomed to region $j_{\mathrm{T}} < 2$ GeV/c. The region of the bump can be identified from the ratio of the distributions.

are expected to be rather narrow angle correlations. Larger j_{T} values will translate into larger angles between trigger and associated particles. Now the normalization for the background can be obtained by fitting the background estimate to the tail of the distribution. The obtained background can then be subtracted from the distribution to obtain the j_{T} signal. The signal can then be further fitted with the two component fit of Gaussian and inverse gamma functions. We should get the same outcome in both cases. The uncertainty raising from this source is called "fitSequence" in the overview plots.

Another source of uncertainty in the signal fitting method comes from the selection of the fit function itself. As was presented with di-gluon PYTHIA in Section 4.5 and using stable triggers in Section 4.6, the support for fit functions, or at least their characteristics, is strong from the simulations. As the fit to pp data is also good in Section 4.6, it was decided to estimate the uncertainty of the fit function from a fit to a restricted range rather that changing the fit function itself. The restricted range was selected in such a way, that the region where the neutral meson decay bump is the most visible is cut out. A zoom to low j_{T} comparing PYTHIA 8 run with all triggers to stable triggers is shown in Figure 44. From the ratio plot we can determine with decent accuracy the region where the distribution is not smooth. The regions to cut out are defined to be $0.25 < j_{\mathrm{T}} < 0.45$ GeV/c for $0.2 < x_{\parallel} < 0.4$ bin, $0.20 < j_{\mathrm{T}} < 0.60$ GeV/c for $0.2 < x_{\parallel} < 0.4$ bin and $0.20 < j_{\mathrm{T}} < 0.65$ GeV/c for $0.6 < x_{\parallel} < 1.0$ bin. The uncertainty coming from here is called "fitRange" in the overview plots.

5.3 Tracking

The uncertainty coming from the tracking is estimated varying the used track cuts. The track cut variations used for systematic uncertainty evaluation are defined at the end of Section 3.2. Separate single particle efficiency calculation is used for each track cut. In the overview plots the uncertainty estimated by varying track cuts is denoted "trackSelection".

Second source of uncertainty on tracking is the uncertainty on tracking efficiency. The determination of tracking efficiency is presented in Section 4.3. As the efficiency curves are obtained from a common Monte Carlo production, the uncertainty does not have to be calculated separately in each analysis, but we can use the numbers determined earlier by other analyses. For pp data the number is said to be 5 % in [160] and for p–Pb data it is 3 % according to [161]. Comparing the p_{T} spectra produced with the efficiency correction used in this analysis to the ones published in these papers, we decided to use the number 5 % directly in this analysis for pp data. There is a small difference in the p_{T} spectra for the p–Pb data, and to take this into account, we decided to increase the uncertainty to 4 % here. The tracking efficiency correction is applied only for yields, since this does not distort the shape of the distribution and thus does not affect the RMS. In the overview plots this is referenced as "trackingEfficiency".

Tracking efficiency might have also a second effect in addition to the overall uncertainty on yield. If we lose the leading particle due to tracking efficiency, we will do the correlations with respect to the subleading particle instead of the leading particle, as we would like to. This might have two different effects. There might be bin flow if the subleading particle goes to a lower p_{Tt} bin compared to the leading particle. This would cause an effect where we would see more yield in lower p_{Tt} bins compared to the larger bins. Also the shape might be distorted if the subleading particle is much worse approximation to the jet axis compared to the leading particle. This would show up in the RMS of the distribution. This effect was studied using a PYTHIA 8 simulation, where we first lost particles according to the same efficiency curve that is used with real data, and then corrected all the remaining particles with the efficiency. Possible effects from the lost leading particles should be visible when these results are compared with a regular PYTHIA 8 simulation, where all the particles are seen. However, the differences in these two simulations were negligible and thus we will not assign any systematic uncertainty from this effect.

5.4 Summary

The total systematic uncertainty is obtained by assuming that all the distinct sources are uncorrelated and adding them together in quadrature. The general trends in the uncertainties are, that the uncertainties for the yield are bigger than

for the RMS, and the uncertainties for the wide component are bigger than for the narrow component. The difference between yield and RMS can be understood as yield more easily reacts to changes in absolute value of the distribution. To change the RMS, the shape of the distribution needs to change. This is more unlikely than just changing the yield. The difference in narrow and wide component can be explained by signal-to-background ratio. This is much better for the narrow component. Thus the narrow component is much more robust against small changes in the background.

A summary for systematic uncertainties for narrow RMS and wide yield for $\sqrt{s} = 7\,\text{TeV}$ pp data can be seen in Figure 45. The uncertainties for wide yield are much bigger than for the narrow RMS. Here both of the effects explained before are in place. If we look at individual sources of uncertainties, the dominant source in most of the cases is the uncertainty coming from the fit function. In the smallest p_{T} bins also background randomization gives noticeable contribution. In this region the signal-to-background ratio is the worst, so the uncertainty on the background is the largest here. Third contribution that jumps out in a few bins is the uncertainty on track selection.

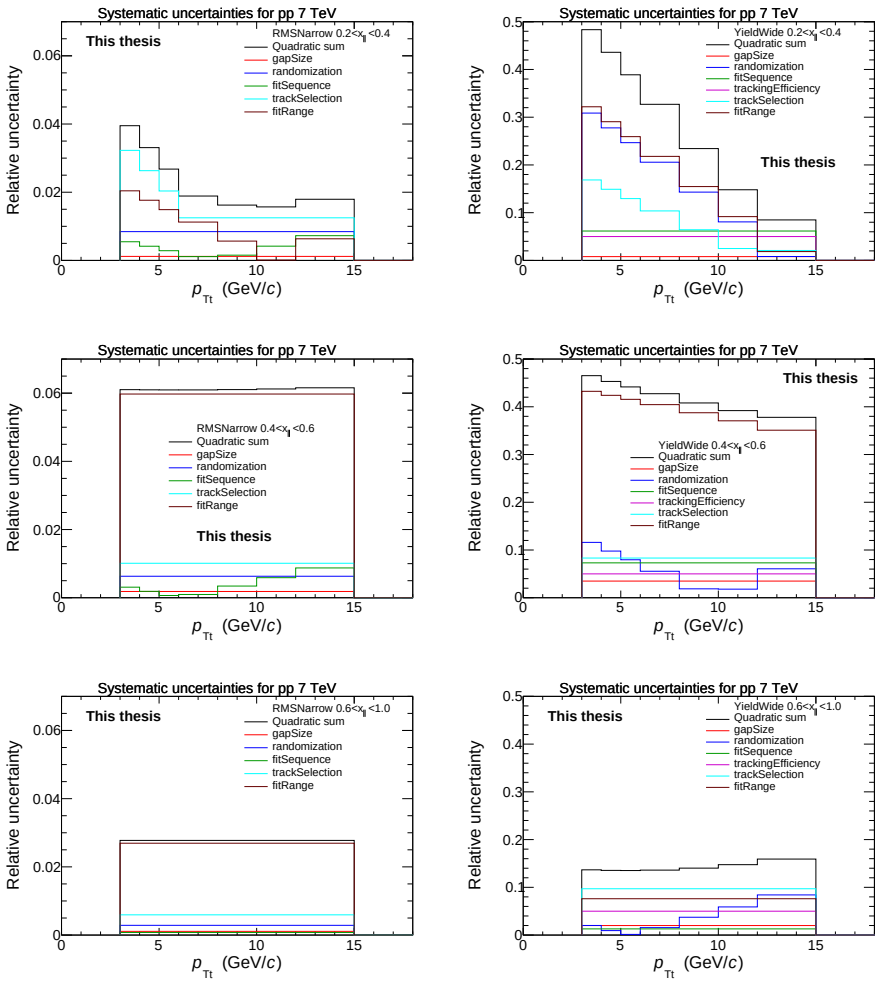

FIGURE 45 Summary of sources for systematic uncertainty for narrow RMS (left column) and wide yield (right column) for $\sqrt{s} = 7$ TeV pp data. The top row shows uncertainties in $0.2 < x_{||} < 0.4$ bin, the middle one in $0.4 < x_{||} < 0.6$ bin and the bottom one in $0.6 < x_{||} < 1.0$ bin.

6 RESULTS

6.1 Results for $\sqrt{\langle j_{\mathrm{T}}^2 \rangle}$

As we now know how to obtain and fit the signal and how to estimate the systematic uncertainties for the chosen methods, we can take a look at the final results. To begin, it is interesting to compare the results obtained in this analysis to similar analyses from earlier publications. The $\sqrt{\langle j_{\mathrm{T}}^2 \rangle}$ for one component has been published earlier, for example, by CCOR [162] and PHENIX [163]. The CCOR paper [162] does not specify how they exactly determine j_{T}, they just give the results. In the PHENIX paper [163] the j_{T} is determined from the azimuthal correlation function. They calculate the RMS j_{T} as

$$\sqrt{\langle j_{\mathrm{T}}^2 \rangle} = \sqrt{2}\, \frac{p_{\mathrm{Tt}} p_{\mathrm{Ta}}}{\sqrt{p_{\mathrm{Tt}}^2 + p_{\mathrm{Ta}}^2}}\, \sigma_{\mathrm{N}} \,, \tag{65}$$

where σ_{N} is the width of the near side peak in azimuthal angle distribution $\sigma_{\mathrm{N}}^2 = \langle \Delta\varphi^2 \rangle$. This is determined by fitting the peak with a Gaussian function. A one component fit was possible in the lower energies available at RHIC or ISR because there was not a clear wide component in the data, as is the case with the current analysis. This one component can be assumed to describe mainly the hadronization part of jet fragmentation, which corresponds to the narrow component in this analysis. Both CCOR and PHENIX required the trigger particle to have high p_{T}, which means that they are also likely to take a big portion of the momentum of initial parton (they are high z particles). PHENIX reports in [163] that this value is $\langle z_{\mathrm{t}} \rangle \sim 0.6$ and it is expected to be of the same order also in CCOR. When the trigger particle takes most of the momentum of the initial parton, there is not so much phase space for the QCD showering left. Thus we may assume that the dominant contribution to the particle spectrum should come from the hadronization part of the fragmentation and compare the results to the narrow component j_{T} results in this analysis. This comparison is done in Figure 46.

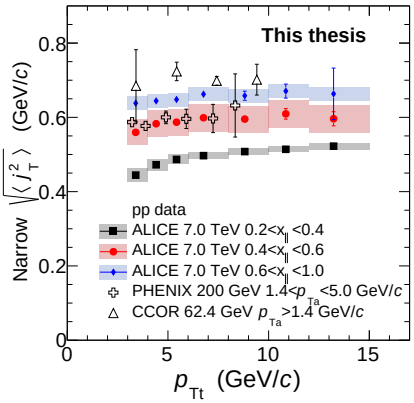

FIGURE 46 The narrow component $\sqrt{\langle j_T^2 \rangle}$ results in different $x_{\parallel}$ bins compared with earlier one component results from PHENIX and CCOR.

Before going to actual comparison, it is good to notice that there is a clear $x_{\parallel}$ dependence in the results of this analysis. This could be caused by kinematics. If the opening angle stays the same, larger associated momentum translates into larger j_T. On the other hand we know that larger momentum particles are more collimated, but the net effect of these two might still increase j_T. At least part of the $x_{\parallel}$ dependence could also come is the trigger is not perfectly aligned with the jet axis, as is assumed in the analysis. This would cause a widening effect for j_T that is stronger for higher $x_{\parallel}$ values, as explained in detail in Appendix 1.3.

The PHENIX results are compatible with the results from bin $0.4 < x_{\parallel} < 0.6$ and the CCOR results are close to the results from bin $0.6 < x_{\parallel} < 1.0$. We cannot use p_{Ta} bins in this analysis because of the bias they induce for the j_T distributions, so we cannot make a meaningful comparison using same binning. However, even in slightly different binning, we should be after the same physics and thus make a rough comparison. The results in this analysis are of the same order and have similar trends as has been previously seen in PHENIX and CCOR, which supports the expectation for the universality of the jet hadronization.

A more detailed look on the $\sqrt{\langle j_T^2 \rangle}$ results obtained in this analysis is given in Figure 47. In this figure the pp data at $\sqrt{s} = 7\,\mathrm{TeV}$ and the p–Pb data at $\sqrt{s_{\mathrm{NN}}} = 5.02\,\mathrm{TeV}$ are compared with PYTHIA 8 tune 4C [164] simulations with the same energies. It should be noted that the simulated system in the PYTHIA 8 event generator is pp in both cases. The different panels in the figure correspond to different $x_{\parallel}$ bins. In the highest $x_{\parallel}$ bin we run out of statistics for p–Pb data for the highest p_{Tt} values. Thus no p–Pb data is shown above $p_{\mathrm{Tt}} = 10\,\mathrm{GeV}/c$. This is why the PYTHIA 8 simulation at $\sqrt{s} = 5.02\,\mathrm{TeV}$ is also shown only upto this value.

Let us first take a look at the narrow component results. In each $x_{\parallel}$ bin, for both datasets and simulations the narrow component results lie on top of each other. On top of this, the p_{Tt} trend is mostly flat. In the few first p_{Tt} bins in $0.2 < x_{\parallel} < 0.4$ bin a slightly rising trend is observed. These are the lowest p_T bins used in the analysis, and it might be that the assumption on a sufficiently high-p_T trigger particle, that can well approximate the direction of the jet axis,

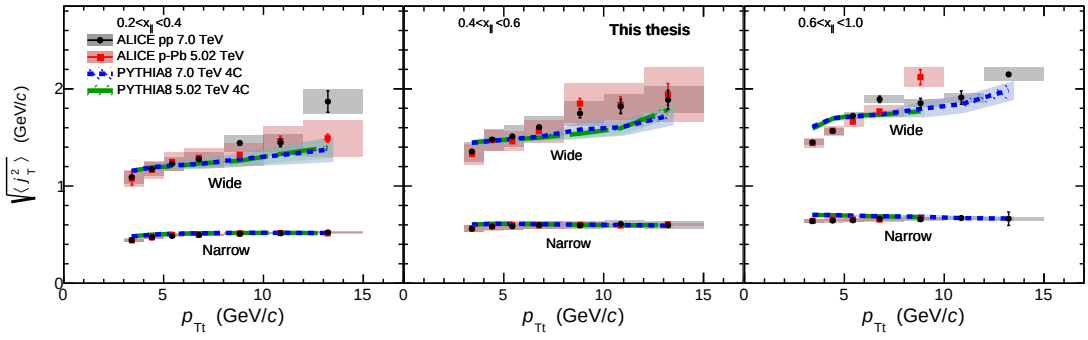

FIGURE 47 The $\sqrt{\langle j_{\mathrm{T}}^2 \rangle}$ results for narrow and wide components. The black points are the ALICE pp data at $\sqrt{s} = 7\,\mathrm{TeV}$ and the red points the ALICE p–Pb data at $\sqrt{s_{\mathrm{NN}}} = 5.02\,\mathrm{TeV}$. The blue and green lines are PYTHIA 8 tune 4C simulations with the same energies as data. The shaded areas around the points and the lines represent the systematic uncertainties of the measurement.

starts to break down on these bins. In Appendix 1.3 it is demonstrated how recoiling partons during the hadronization might cause a rising p_{Tt} trend in $\sqrt{\langle j_{\mathrm{T}}^2 \rangle}$. This effect would be the strongest in the smallest $x_{\parallel}$ bin, since in this bin $\langle z_{\mathrm{t}} \rangle$ is largest and thus initial parton momentum the smallest and the assumptions of the analysis require a high momentum leading parton. The similarity between datasets and flatness as a function of p_{Tt} suggest that the jet fragments coming from the hadronization spread similarly around the jet axis in different systems, regardless of the colliding particles or the momentum of scattered partons. The Lund string fragmentation model seems to reproduce this feature, as PYTHIA 8 is able to describe the data.

Moving on to the wide component results, we can see that the p_{Tt} trend clearly changes. A flat trend is not observed anymore, but the wide component $\sqrt{\langle j_{\mathrm{T}}^2 \rangle}$ grows as p_{Tt} grows. The trend is again similar in both datasets and simulations. The change in the trend tells us that the QCD showering part of the jet fragmentation is not system independent in the same way as hadronization. Instead, the jet fragments are spreading farther away from the jet axis when higher transverse momentum leading particle is present in the event. To explain this effect, we can first note that according to the PYTHIA 8 study presented in Appendix 2 the average fraction of the leading parton momentum taken by the leading particle decreases slightly as a function of p_{Tt} inside an $x_{\parallel}$ bin. When the fraction of the momentum taken by the trigger decreases slightly and the absolute momentum increases, there is more phase space left over for QCD radiation to take place. More splittings are likely to spread also to larger angles, which would cause $\sqrt{\langle j_{\mathrm{T}}^2 \rangle}$ to grow as a function of p_{Tt}. If this is the case, we should also see an increase of per trigger j_{T} yield as a function of p_{Tt} for the wide component.

If there would be significant cold nuclear matter effects, we should see them as a difference in wide component RMS results between pp and p–Pb data. It was speculated in Section 1.2.3 that multiple scattering of partons inside the heavy

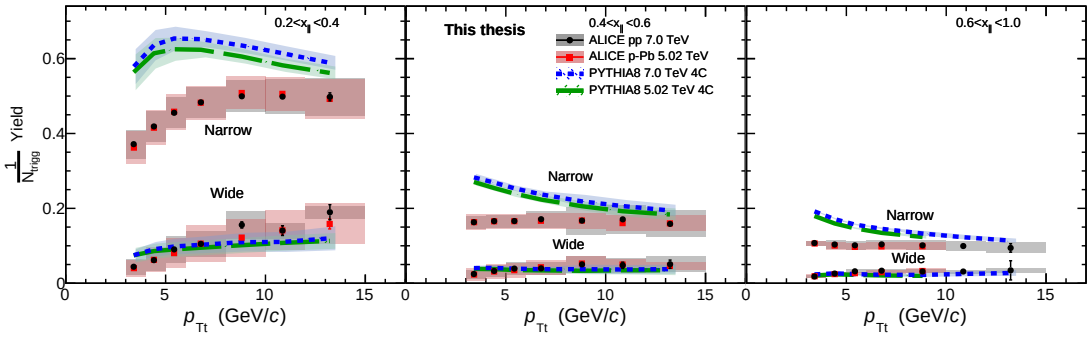

FIGURE 48 The per trigger j_T yields for narrow and wide components. The black points are the ALICE pp data at $\sqrt{s} = 7\,\text{TeV}$ and the red points the ALICE p–Pb data at $\sqrt{s_{\text{NN}}} = 5.02\,\text{TeV}$. The blue and green lines are PYTHIA 8 tune 4C simulations with the same energies as data. The shaded areas around the points and the lines represent the systematic uncertainties of the measurement.

nucleus could lead to broadening of jets. In this analysis this would show up as an increase of $\sqrt{\langle j_{\text{T}}^2 \rangle}$ in the p–Pb system as compared to the pp system. Seeing that the two different PYTHIA 8 curves from different energies lie on top of each other, we do not expect there to be an effect from the different collision energies. Now that also the data from pp collisions at $\sqrt{s} = 7\,\text{TeV}$ and p–Pb collisions at $\sqrt{s_{\text{NN}}} = 5.02\,\text{TeV}$ are perfectly compatible with each other, we can say that we see no cold nuclear matter effects in this analysis.

6.2 Results for per trigger j_T yield

The narrow and wide component yield results for pp data at $\sqrt{s} = 7\,\text{TeV}$, p–Pb data at $\sqrt{s_{\text{NN}}} = 5.02\,\text{TeV}$ and PYTHIA 8 tune 4C simulations in the same energies are presented in Figure 48. Let us begin again inspecting these results from the narrow component. The yields from pp and p–Pb data are on top of each other. We saw already in the RMS plots that the $\sqrt{\langle j_{\text{T}}^2 \rangle}$ widths for the different collision systems are the same, and now we can see that there is no modification in the yields either. As before, the interpretation of this observation is that the hadronization proceeds in a similar manner in different systems.

If we look at the PYTHIA 8 simulations for the narrow component yield, it can be seen that they overestimate the data by upto 50 %. Similar observation has been previously made by ALICE in the underlying event paper [157]. You can see one azimuthal correlation function plot from that paper in Figure 49. In this plot an older PYTHIA 8 tune called tune 1 is used as opposed to the tune 4C, which is used in the analysis presented in this thesis. However, it was found out that in case of this analysis the difference in yield when using tune 1 or tune 4C is small. Thus comparing the black data points in Figure 49 to the blue PYTHIA 8 simulation line provides a relevant comparison for this analysis. The narrow component yield

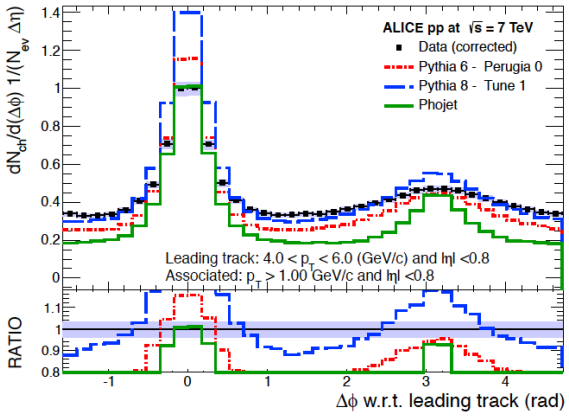

FIGURE 49 Azimuthal correlation function published in the underlying event paper by ALICE [157]. In the center of the near side peak the PYTHIA simulation overestimates the peak, but the description in better on the edges of the peak.

corresponds to the yield close to $\Delta\varphi = 0$ in the near side peak. It can be seen that in this region the PYTHIA 8 simulation shows much higher peak than the ALICE data, which is the same observation that is made in this analysis.

There is also a difference in the p_{Tt} trends between data and PYTHIA 8. In the $0.2 < x_{\parallel} < 0.4$ bin the data rises monotonically, but PYTHIA 8 starts to decrease after first three p_{Tt} bins. In the higher $x_{\parallel}$ bins there is also a clear decrease in the j_{T} yield as a function of p_{Tt}, which is not visible in data. The simulation seems to be closest to the data in the highest p_{Tt} bins.

Moving on to the wide component yield results, first we can note that the systematic uncertainties start to get quite large. This makes seeing trends more difficult. As for the p_{Tt} trend, it looks like yield would be slightly rising as p_{Tt} rises. The increased phase space for soft gluon radiation at higher p_{Tt} could explain this trend, as was already proposed when examining the RMS results. However, the systematic uncertainties are so large, that the results are also compatible with a flat trend within the error bars. The best thing that can be said here is that the explanation given for the RMS is still plausible after seeing the yield results, but not much more support is given to it from here.

Comparing pp results to p–Pb results we again get results that are exactly on top of each other. This is hardly surprising after seeing the RMS results that show the same thing and confirms the conclusion that no cold nuclear matter effects are visible in this analysis.

For the wide component PYTHIA 8 simulations are actually within the systematic uncertainties of the measurement. This means that the simulation is doing better job here than it did for the narrow component. This is again compatible with the ALICE underlying event paper [157]. The wide component would now correspond to the edges of the near side peak in Figure 49. Near the edges of the peak the black data points are much closer to the blue PYTHIA 8 simulation than in the middle of the peak. This means that the yield of the wide component in the simulation should be close to the one coming from the data.

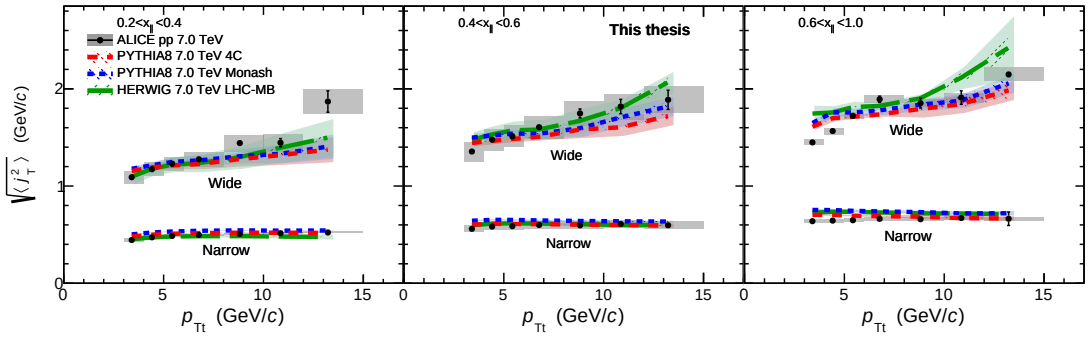

FIGURE 50 The $\sqrt{\langle j_{\mathrm{T}}^2 \rangle}$ results for the $\sqrt{s} = 7$ TeV pp data (black points) compared with PYTHIA 8 and Herwig 7 simulations. The different tunes are PYTHIA 8 tune 4C (red), PYTHIA 8 Monash tune (blue) and Herwig 7 LHC-MB tune (green).

6.3 Comparison to models

In the previous section there has already been some comparison to PYTHIA 8 simulations, but a more comprehensive comparison of the data to different simulations is presented in this section. The comparison is done only to the $\sqrt{s} = 7$ TeV pp data, since the simulations are pp simulations and it is thus more straightforward to make the comparison this way. Together with the PYTHIA 8 tune 4C [164], the comparison is done to the PYTHIA 8 Monash tune [165] and the Herwig 7 LHC-MB tune. Both of the PYTHIA 8 tunes use the data from LEP and Tevatron as the baseline for tuning the parameters. The PYTHIA 8 tune 4C is the default tune in late PYTHIA 8.1 versions and it includes a study of early LHC $\sqrt{s} = 7$ TeV pp data. The Monash tune is a newer and improved tune, including an improved study of the old data and more data from LHC. It is the default tune in PYTHIA since version 8.2. The LHC-MB tune for Herwig 7 is tuned to the ATLAS pp data at $\sqrt{s} = 7$ TeV and is recommended to be used for minimum bias simulations at the Herwig 7 web pages [166].

The $\sqrt{\langle j_{\mathrm{T}}^2 \rangle}$ results for different event generators together with pp data are shown in Figure 50. We can start to examine the figure again from the narrow component. The narrow component $\sqrt{\langle j_{\mathrm{T}}^2 \rangle}$ results for all the simulated datasets are close to pp data, but PYTHIA 8 tune 4C seems to be the most consistently closest to the data. Monash tune tends to be slightly above the data and Herwig 7 has stronger $x_{\parallel}$ dependence than PYTHIA 8 simulations or the data. If you look closely you can see that the green Herwig 7 curve is below the data on $0.2 < x_{\parallel} < 0.4$ bin, on top of the data in $0.4 < x_{\parallel} < 0.6$ bin, and above the data on $0.6 < x_{\parallel} < 1.0$ bin. It is stated in [94] that usually cluster hadronization model gives slightly less good results than string model, but it does so with fewer parameters. As Herwig 7 uses the cluster hadronization model as opposed to Lund string model in PYTHIA 8, it could be that this statement is reflected in this analysis in slightly too strong $x_{\parallel}$ dependence for the cluster hadronization model.

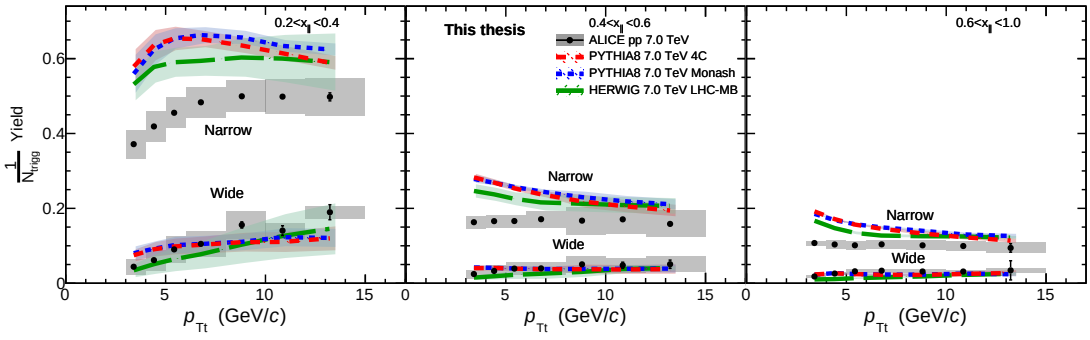

FIGURE 51 The per trigger j_T yields for the $\sqrt{s} = 7$ TeV pp data (black points) compared with PYTHIA 8 and Herwig 7 simulations. The different tunes are PYTHIA 8 tune 4C (red), PYTHIA 8 Monash tune (blue) and Herwig 7 LHC-MB tune (green).

For the wide component RMS results all event generators are again providing results that are close to measured data. The two PYTHIA 8 datasets are very close to each other, with the Monash tune slightly closer to the data. Herwig 7 tends to be consistently above the PYTHIA 8 results with the exception of the few lowest p_{Tt} and $x_{\parallel}$ bins. The main difference between PYTHIA 8 and Herwig 7 shower algorithms is the choice of the evolution parameter in the DGLAP equation 7, as explained in detail in Section 1.4. In Herwig 7 this variable is chosen such that angular ordering is ensured, while in PYTHIA 8 the ordering is done in decreasing hardness of the splittings. It seems that when angular ordering is followed exactly, more particles at large angles are produced.

The per trigger j_T yields from different simulations are compared to pp data in Figure 51. For the narrow component yield we see that all the simulations are overestimating the yield. Herwig 7 is closer to the data that either of the PYTHIA 8 curves, but still clearly above it. Thus it seems that for the parameters used in these simulations, the cluster hadronization model produces less particles than the string model, but even less would be needed to match the data.

Also the p_{Tt} trends for all the simulations seem to be different than the trend in the data. The pp data shows no dependence on p_{Tt} in the $0.4 < x_{\parallel} < 0.6$ and $0.6 < x_{\parallel} < 1.0$ bins, while in all the simulations the yield decreases with p_{Tt}. For Herwig 7 the trend becomes quite flat for the highest p_{Tt} bins in these two $x_{\parallel}$ bins, agreeing better with the data. This flattening is not so clear in either of the PYTHIA 8 tunes, even though also for them the discrepancy with the data gets smaller towards higher p_{Tt}.

For the wide component yield Herwig 7 seems to be again describing it better than either of the PYTHIA 8 tunes. In Herwig 7 the j_T yield raises stronger as a function of p_{Tt} than for either of the PYTHIA 8 tunes. In higher $x_{\parallel}$ bins both PYTHIA 8 tunes show flat trend when data and Herwig tend to have a slightly rising trend. Exactly fulfilling angular ordering in the parton shower seems to favor large p_{Tt} particle production more than when the splittings are ordered in decreasing hardness. However, the error bars for the yields are large and thus no strong conclusions can be made out of these hints.

7 SUMMARY AND OUTLOOK

A new method to study the jet fragmentation transverse momentum j_T is developed in this thesis. The method enables to separate distinct components for the QCD showering (wide) and hadronization (narrow) from two-particle correlation analysis. The main goal is to extract $\sqrt{\langle j_T^2 \rangle}$ and per trigger j_T yields for both of the components.

The narrow component RMS results can be related to previous j_T measurements made by CCOR and PHENIX and the results from these previous analyses are along the same lines as the results from this analysis, as is shown in Figure 46. The narrow component $\sqrt{\langle j_T^2 \rangle}$ results from this analysis show clear $x_{\parallel}$ dependence, which might a kinematics effect. If the angle between the particles stays roughly the same and p_{Ta} grows, this translates into larger $\sqrt{\langle j_T^2 \rangle}$. Inside one $x_{\parallel}$ bin there is no dependence on p_{Tt}. As also both collisions systems and energies give the same results, the narrow component $\sqrt{\langle j_T^2 \rangle}$ results support the expectation of universal jet hadronization.

The wide component RMS results in Figure 47 are not independent of p_{Tt} as the narrow component results were, but now $\sqrt{\langle j_T^2 \rangle}$ rises as p_{Tt} rises. This observation could be explained by increased phase space for soft gluon radiation allowed at higher momenta. This explanation is supported by the wide component yield results in Figure 48, where the trend seems to also be slightly rising, as should happen if the available phase space increases.

Possible cold nuclear matter effects can be searched for by comparing the wide component RMS and yield results in the pp and p–Pb datasets, as is done in Figures 47 and 48. As both of the datasets give the same results, no evidence of the cold nuclear matter effects is seen in this analysis.

The final results are also compared to PYTHIA 8 and Herwig 7 simulations in Figures 50 and 51. In general the simulations describe the data well, but both of them overestimate the narrow component yield. An interesting detail is the difference between the two simulations for the wide component RMS. The RMS seems to rise slightly stronger for Herwig as a function of p_{Tt} and especially

in the high p_{Tt} region Herwig gives systematically larger values than PYTHIA. One possible explanation for this could be differences how angular ordering is implemented in the shower algorithm for these generators. This hints that the wide component could have some discriminating power between different models for angular ordering.

A natural continuation for this analysis would be to study j_{T} distributions also in the Pb–Pb data. The used analysis methods should be mostly applicable also in the heavy ion system. The R-gap method used to estimate the systematic uncertainties for the j_{T} background is however unusable due to flow modulation, so a new method for this needs to be developed. Also in the high multiplicity environment of heavy ion collisions there might be merging of tracks in the detector. This effect needs to be evaluated and also corrected if it turns out to be non-negligible.

It will be interesting to see if the narrow component stays intact in heavy ion collisions, as is expected if the hadronization happens outside the hot medium. Even more interesting will be to see how the wide component is modified. Previous measurements show that the near side jet peak should broaden in heavy ion collisions [167]. This is mainly due to parton interactions with quark-gluon plasma [168]. In the hot medium also color decoherence effects are expected, leading into anti-anglular ordering [169] and even broader jet shape. One also expects gluon jets to be more suppressed by the hot medium than quark jets [170], which in turn would make the jets narrower. How the total effect looks like and whether the wide j_{T} component is capable of distinguishing the effects from different contributions remains to be seen.

APPENDIX 1 TOY SIMULATION

APPENDIX 1.1 Simulation details

The analysis methods and assumptions can be tested in an idealized situation using a simplistic toy simulation. For this analysis a toy simulation was written that creates events where there can be a jet on top of a background distribution or only the background. The jet is present in 80 % of the events and in the remaining 20 % only background will be generated.

In the background events the particles are distributed uniformly within $-0.8 < \eta < 0.8$ and their p_{T} in GeV/c is randomly sampled from exponentially suppressed distribution

$$f(p_{\mathrm{T}}) = (0.4 + p_{\mathrm{T}})e^{-3p_{\mathrm{T}}} \, . \tag{66}$$

The variable p_{T} is allowed to be in range [0,20]. The constants in this equation and in equation (68) are chosen such that the resulting overall p_{T} spectrum matches the one measured by ALICE [160] within 30 %. The multiplicity k of the event is sampled from negative binomial distribution

$$f(k) = N \, \frac{\Gamma(k+r)}{\Gamma(k+1)\Gamma(r)} \, (1-p)^k p^r \, , \tag{67}$$

where the parameters $N = 1.06773$, $r = 1.13092$ and $p = 0.0887187$ are obtained by fitting this function to the ALICE data [171].

In the jet events there is a simple jet generated on top of underlying event background. First, the p_{T} of the jet is sampled from the interval $3 < p_{\mathrm{T,jet}} < 200$ GeV/c using power law

$$f(p_{\mathrm{T}}) = p_{\mathrm{T}}^{-5} \text{ GeV}/c \, . \tag{68}$$

The direction of the jet axis is random within $-0.8 < \eta < 0.8$. This jet is then fragmented by first sampling a random z from the fragmentation function

$$f(z) = N \, (1-z)^a \, e^{-bz} \, , \tag{69}$$

where $N = 7.7$, $a = 0.15$ and $b = 8.5$. The form and parameters of the fragmentation function are taken from the Master's thesis of Elias Barba Moral [172], where he studied the fragmentation function using ATLAS data. A new massless hadron is generated from the jet by setting $p_{\mathrm{hadron}} = z p_{\mathrm{jet}}$. A j_{T} kick is then given to this new hadron such that the direction of the kick is random in the plane perpendicular to the jet axis. The magnitude of the kick is sampled from a Gaussian distribution

$$f(j_{\mathrm{T}}) = j_{\mathrm{T}} \, e^{\frac{-j_{\mathrm{T}}^2}{2\sigma^2}} \text{ GeV}/c \tag{70}$$

with $\sigma = \frac{0.6}{\sqrt{2}}$. The factor $\sqrt{2}$ is added to σ because we are sampling length for two dimensional vector from one dimensional distribution. The one j_{T} factor

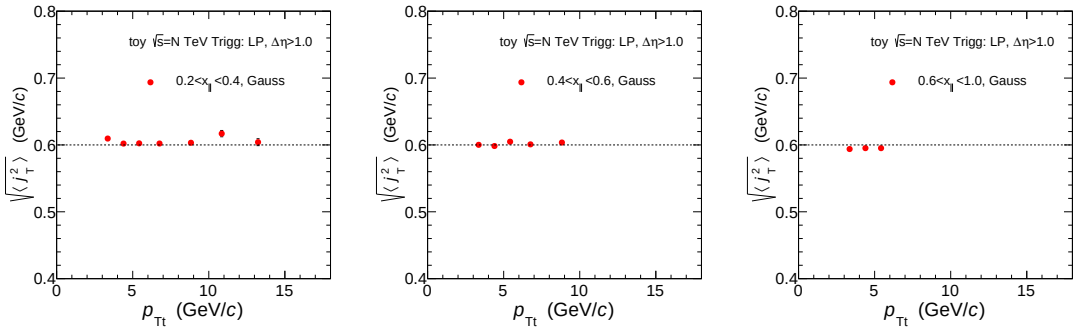

FIGURE 52 The $\sqrt{\langle j_{\mathrm{T}}^2 \rangle}$ results obtained from data generated by the toy simulation. We seem to regain nicely the inserted $\sqrt{\langle j_{\mathrm{T}}^2 \rangle} = 0.6$ GeV.

before the Gaussian function is the Jacobian of polar coordinates. After this the momentum of jet axis is updated by multiplying the original momentum by $1 - z$. This process is continued until $E_{\mathrm{jet}} < 1$ GeV. Next we find the particle among the generated particles that has the highest p_{T} and align it among the jet axis to match the assumption made in this analysis. The total multiplicity of the jet event is sampled from the same negative binomial distribution given by equation (67) as for background event. If the jet fragmentation produces enough particles to fill the multiplicity requirements, 2 background particles are added to the event. Otherwise the missing multiplicity is filled with background particles. The background particles are generated in the same manner as in only background events.

In both cases the events with generated particles are analyzed using the standard analysis methods presented in chapter 4.

APPENDIX 1.2 Results in $x_{\parallel}$ and p_{Ta} bins

The data produced by the toy simulation is analyzed using the same analysis macros as for the real data. The exception is that as there is no wide component in the simulation, the fit function consists only of the background and the Gaussian component. The obtained results are presented in Figure 52. It can be seen that the inserted value $\sqrt{\langle j_{\mathrm{T}}^2 \rangle} = 0.6$ GeV/c is nicely regained. The higher $x_{\parallel}$ bins in Figure 52 lack some data points, since the parameters of the simulation do not generate much associated particles there.

We can do the same study in p_{Ta} bins to check if the analysis works properly also when binned differently. The final $\sqrt{\langle j_{\mathrm{T}}^2 \rangle}$ results in a few lowest p_{Ta} bins are shown in Figure 53. The fitting procedure in the lowest p_{Ta} bin was not very stable, so the p_{Ta} trend is a bit different than in other bins. The results are anyhow clear, binning the results in p_{Ta} biases the distributions towards higher j_{T}

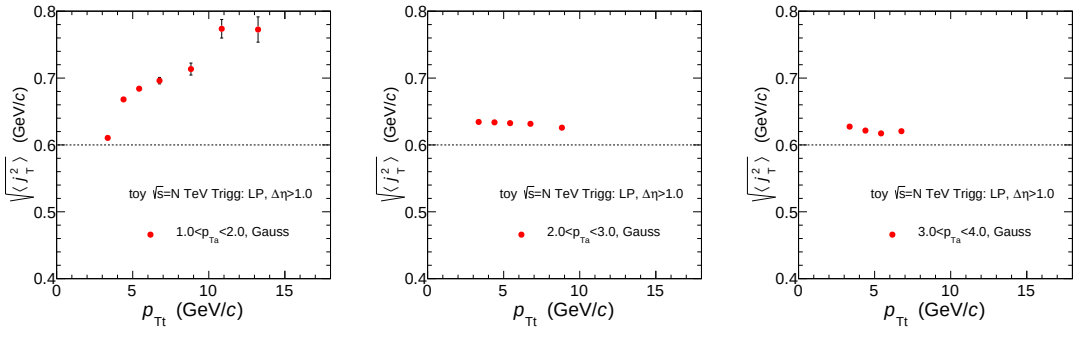

FIGURE 53 The $\sqrt{\langle j_{\mathrm{T}}^2 \rangle}$ results obtained from data generated by the toy simulation. In p_{Ta} bins the obtained results do not match the input.

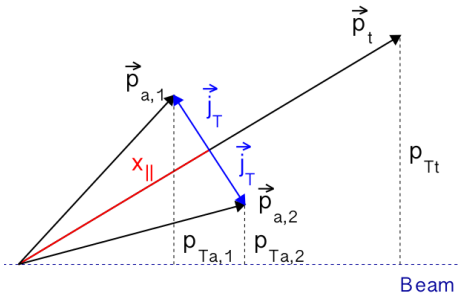

FIGURE 54 Illustration why p_{Ta} binning biases the $\sqrt{\langle j_{\mathrm{T}}^2 \rangle}$ results.

values. This effect can be understood from kinematics as illustrated by Figure 54. The direction of the j_{T} kick affects the p_{T} of the associated particle. In Figure 54 associated particles labeled 1 and 2 have both the same magnitude of momentum, $|\vec{p}_{\mathrm{Ta},1}| = |\vec{p}_{\mathrm{Ta},2}|$. Their only difference is that as they fragment from the jet axis, they receive the j_{T} kick into opposite directions. From this it follows that $p_{\mathrm{Ta},1} > p_{\mathrm{Ta},2}$. This becomes a problem when $p_{\mathrm{Ta},1}$ and $p_{\mathrm{Ta},2}$ end up in different associated particle bins. This "bin flow" effect is stronger for higher values for j_{T}, making it more likely for larger j_{T} values to flow into other bins. As the p_{T} spectrum is exponentially falling, there are more high j_{T} particles flowing to a given bin over the lower p_{Ta} border of that bin than there are high j_{T} particles flowing out of the bin over the higher p_{Ta} border of the bin. Thus an enhancement of $\sqrt{\langle j_{\mathrm{T}}^2 \rangle}$ is seen in all the bins of the analysis and this enhancement is stronger in lower p_{Ta} bins.

It should be noted that as $x_{\parallel}$ is by definition perpendicular to j_{T}, as can be seen from Figure 54. Thus the "bin flow" effect does not exist for $x_{\parallel}$ bins.

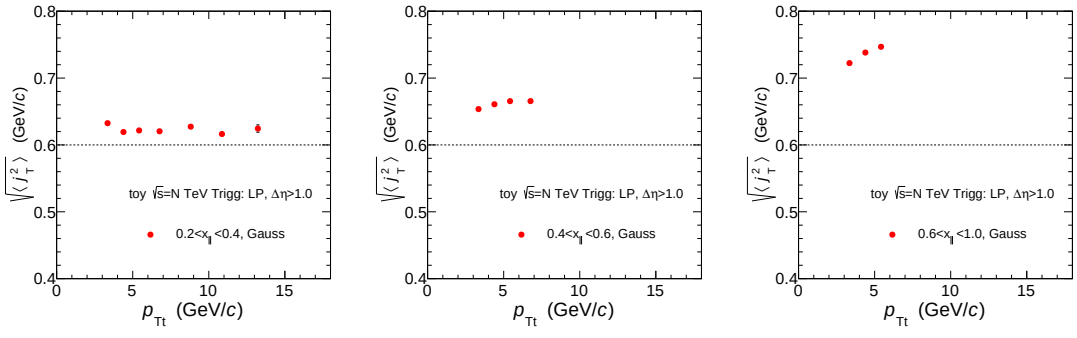

FIGURE 55 The $\sqrt{\langle j_T^2 \rangle}$ results obtained from data generated by the toy simulation where the j_T kick is given also for the trigger particle. Now there is $x_{\parallel}$ dependence on the results.

APPENDIX 1.3 Breaking the trigger assumptions

An idealized simulation is a good place to do some basic tests how the results are affected, if the assumptions are not perfectly correct. We tested what happens if the trigger particle is not aligned with the jet axis, but gets the same j_T kick as is given for the associated particles. The $\sqrt{\langle j_T^2 \rangle}$ results with this setup are shown in Figure 55. Here we see some $x_{\parallel}$ dependence which was not present when the trigger was aligned with the jet axis. In the smallest $x_{\parallel}$ bin the obtained $\sqrt{\langle j_T^2 \rangle}$ results are still close to the input, but the difference grows when $x_{\parallel}$ increases. Too high $\sqrt{\langle j_T^2 \rangle}$ values are observed. The reason for this is illustrated in Figure 56. The jet fragments are distributed approximately evenly in all directions around the jet axis. Especially the distance to the farthest away fragments is constant in every direction. If we now choose to correlate these fragments with a particle that is not aligned with the jet axis, the distribution around becomes biased in some direction. The jet fragments are likely to be farther away from this particle than they are from the jet axis. Thus the $\sqrt{\langle j_T^2 \rangle}$ increases.

Comparing the left and right pictures in Figure 56 illustrates why there is $x_{\parallel}$ dependence when trigger is not perfectly aligned with the jet axis. In both of the pictures all the blue $\vec{j}_T$ vectors with respect to the jet axis are the same. The only difference is the magnitudes of $\vec{p}_{a,1}$ and $\vec{p}_{a,2}$ vectors, resulting different $x_{\parallel}$ values. Now if you compare the magenta vectors representing the j_T with respect to the trigger particle, you see that in the orientation when the direction of j_T kick given to the associated particle is different to the one given in trigger, the j_T with respect to trigger increases more when the $x_{\parallel}$ is bigger. This explains the $x_{\parallel}$ dependence and needs to be kept in mind when interpreting the results from real data.

In the toy simulation we can go even further in breaking the assumptions. In addition to giving j_T kick also to the trigger, we can recoil the jet axis every time a new particle is generated. This is done such that when a particle is generated and

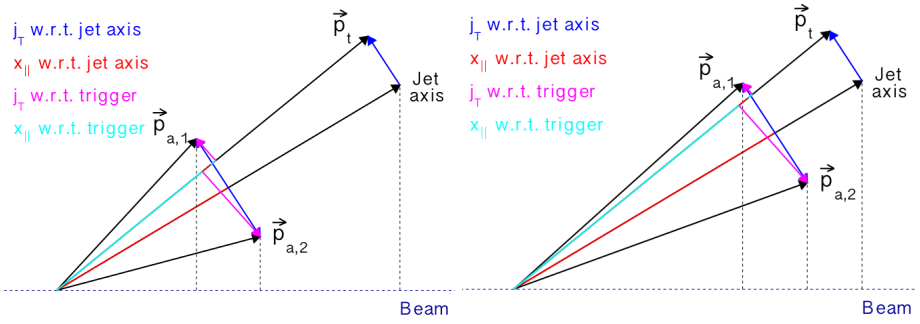

FIGURE 56 Illustration of the widening effect of $\sqrt{\langle j_{\mathrm{T}}^2 \rangle}$ as a function of $x_{\parallel}$. *Left:* Kick in trigger for small $x_{\parallel}$. *Right:* Kick in trigger for large $x_{\parallel}$.

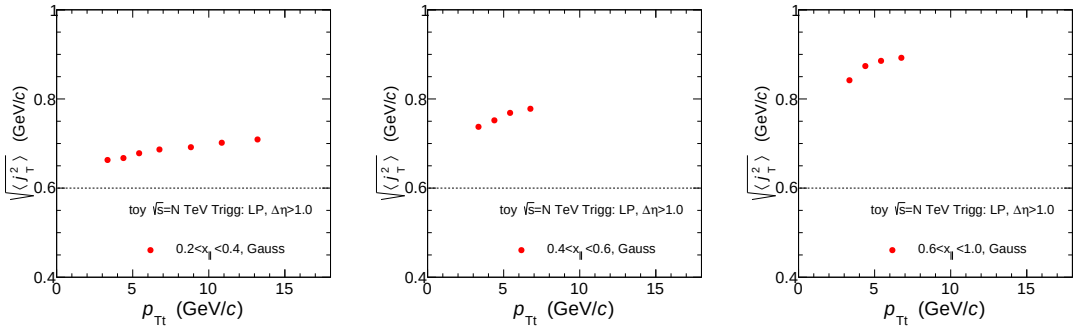

FIGURE 57 The $\sqrt{\langle j_{\mathrm{T}}^2 \rangle}$ results obtained from data generated by the toy simulation where the j_{T} kick is given also for the trigger particle and the jet axis is recoiled every time a new particle is generated. Together with $x_{\parallel}$ dependence, also p_{Tt} dependence appears.

a kick of $\vec{j}_{\mathrm{T}}$ is given to it, a kick of $-\vec{j}_{\mathrm{T}}$ is given to the jet axis. The results of this simulation are shown in Figure 57. We see that the $x_{\parallel}$ dependence is now even stronger than in the case where the jet axis is not allowed to recoil. In addition to that, there is now p_{Tt} dependence on the results. When p_{Tt} rises, $\sqrt{\langle j_{\mathrm{T}}^2 \rangle}$ also rises. An explanation for this trend could be that there can be more particles fragmenting from the jet at higher momentum. This means than the jet axis has more opportunities to recoil, can is thus likely point farther away from the trigger particle, resulting in increased $\sqrt{\langle j_{\mathrm{T}}^2 \rangle}$.

APPENDIX 2 STUDY ON $\langle Z \rangle$ OF TRIGGER PARTICLES

To get some quantitative information to argue that the momentum fraction z the leading particle takes from the leading parton stays rather constant inside an $x_{\parallel}$ bin, a simple PYTHIA 8 study was conducted. This study was done with PYTHIA 8 rather than real data, since in PYTHIA we do not need to care about edge effects of acceptance. To obtain z_{t}, it is assumed that the jet around the leading particle gives a good approximation of the leading parton kinematics. Then z_{t} becomes the fraction of the jet momentum taken by the leading particle. Since for this study it is sufficient to see z_{t} trends, we decided that using jet reconstruction via FastJet [173] package is not needed, but a simplified method can be used. The following algorithm was used to determine z_{t}:

1. Determine the leading particle
2. Define a cone of radius $R = \sqrt{\Delta\varphi^2 + \Delta\eta^2} = 0.6$ around the leading particle
3. Calculate the momentum vector of the jet: $\vec{p}_{\mathrm{jet}} = \sum_{i \in \mathrm{cone}} \vec{p}_i$
4. Calculate $z_{\mathrm{t}} = \frac{|\vec{p}_t|}{|\vec{p}_{\mathrm{jet}}|}$

In step 4 also the projection of trigger particle momentum with respect to the jet axis was used as a numerator instead of just trigger particle momentum, but the results in both cases were the same. This estimate assumes that all the particles close to the trigger particle are coming from the leading parton fragmentation. No background subtraction is applied.

The obtain the results, a PYTHIA 8 run with Monash tune was performed. In the run the trigger particle was required to be in the same range as normally in the analysis, $|\eta_{\mathrm{t}}| < 0.8$. To avoid the effects of jet cone hitting the edge of the acceptance and thus artificially enhancing z_{t}, all the associated particles in the range $|\eta_{\mathrm{a}}| < 0.8 + 0.6 = 1.4$ were accepted when determining the z_{t}. However, when doing the correlations and filling histograms, only associated particles in range $|\eta_{\mathrm{a}}| < 0.8$ were considered to do the correlations for similar particle pairs as in the actual analysis. For each trigger associated pair, the z_{t} value was filled in the corresponding $x_{\parallel}$ bin. The only correction applied for this number was the acceptance correction, coming from the fact that it is more likely to see a pair with small $\Delta\eta$ due to limited η acceptance.

Two examples of the obtained z_{t} distribution are presented in Figure 58. In the left plot there is an example from bin $4 < p_{\mathrm{Tt}} < 5\,\mathrm{GeV}/c$ and $0.2 < x_{\parallel} < 0.4$. In this low momentum bin, the distribution is a bit distorted in the high z region. It is not obvious what causes this distortion, but a good candidate would be the simplistic jet reconstruction algorithm that is used to obtain the results. On the right hand side of Figure 58 a higher momentum bin $8 < p_{\mathrm{Tt}} < 10\,\mathrm{GeV}/c$ and $0.4 < x_{\parallel} < 0.6$ is shown. In this bin the distortion is significantly smaller. As we are mostly interested in the mean of the distribution, we do not reckon that this small distortion will affect the mean much.

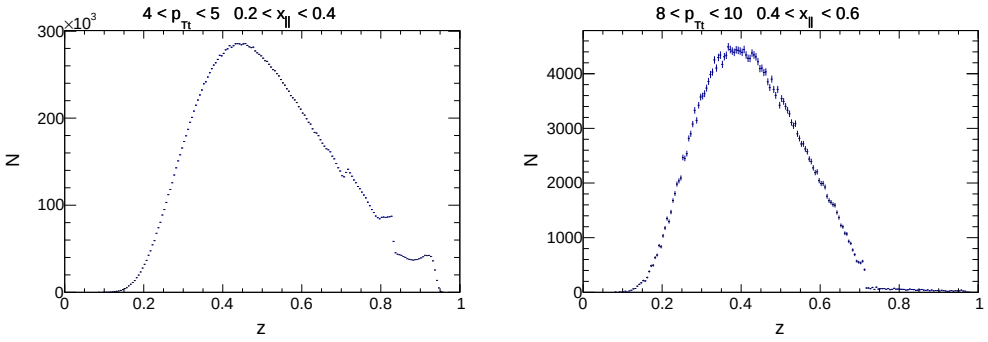

FIGURE 58 Trigger z distributions from PYTHIA 8 in two different p_{Tt} and $x_{\parallel}$ bins.

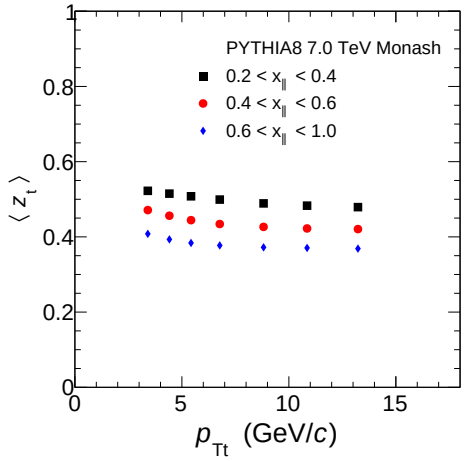

FIGURE 59 The $\langle z_{\mathrm{t}} \rangle$ results as a function of p_{Tt}. Different $x_{\parallel}$ bins are shown in different colors.

The $\langle z_{\mathrm{t}} \rangle$ results as a function of p_{Tt} for all the $x_{\parallel}$ bins are presented in Figure 59. There are two trends visible in this figure. First, one can see that there is a clear ordering in $x_{\parallel}$, with lowest $x_{\parallel}$ bins showing the largest $\langle z_{\mathrm{t}} \rangle$. This is as expected, since if we have a particle in the event whose momentum component to the direction of the trigger particle is large compared to the trigger momentum (high $x_{\parallel}$), the trigger cannot have taken a very large fraction of the original parton momentum. In addition to this, inside each $x_{\parallel}$ bin the $\langle z_{\mathrm{t}} \rangle$ values go slightly down as p_{Tt} grows. The difference between the first and the last points in approximately 0.05 units. This observation can be understood as a competition of two effects. As the trigger p_{T} grows for constant associated p_{T}, it is likely to take a larger fraction from the original parton momentum. Vice versa if associated p_{T} grows for constant trigger p_{T}, the trigger is likely to take a smaller fraction from the original parton momentum. Inside an $x_{\parallel}$ bin the p_{Ta} grows as the p_{Tt} grows and the net effect seems to be that the $\langle z_{\mathrm{t}} \rangle$ trend is slightly decreasing.

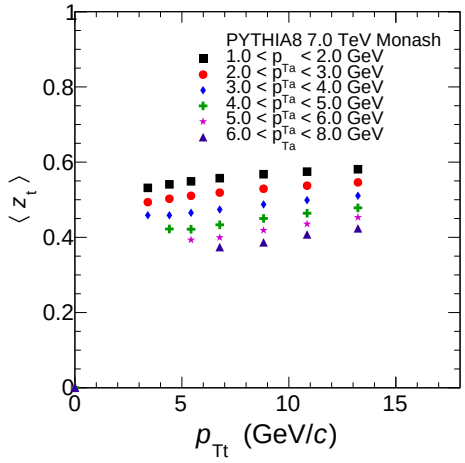

FIGURE 60 The $\langle z_t \rangle$ results as a function of p_{Tt}. Different p_{Ta} bins are shown in different colors.

To verify that the expected trend is obtained in p_{Ta} bins, the same study was repeated binning the distributions in p_{Ta} rather than $x_{\parallel}$. The $\langle z_t \rangle$ in p_{Ta} bins are shown in Figure 60. Indeed, in all of the explored p_{Ta} bins a rising trend as a function of p_{Tt} is seen, as was expected from the reasoning above and also from previous $\langle z_t \rangle$ studies presented, for example, by PHENIX [163].

APPENDIX 3 GLOSSARY OF USED SYMBOLS

ACORDE	-	ALICE Cosmic Ray Detector
AD	-	ALICE Diffractive detector OR Antimatter Decelerator
CERN	-	European Organization for Nuclear Research
CTP	-	Central Trigger Processor
DCA	-	Distance of Closest Approach
DCal	-	Di-Jet Calorimeter
DGLAP	-	Dokshitzer–Gribov–Lipatov–Altarelli–Parisi equation
EMCal	-	Electromagnetic Calorimeter
FEE	-	Front-End Electronics
FMD	-	Forward Multiplicity Detector
FPGA	-	Field-Programmable Gate Array
HMPID	-	High Momentum Particle Identification
ITS	-	Inner Tracking System
L0	-	Level-0 trigger decision
L1	-	Level-1 trigger decision
LHC	-	Large Hadron Collider
PHOS	-	Photon Spectrometer
PMD	-	Photon Multiplicity Detector
pQCD	-	Perturbative QCD
PS	-	Proton Synchrotron
QCD	-	Quantum Chromodynamics
QED	-	Quantum Electrodynamics
RF	-	Radio Frequency
RMS	-	Root-Mean-Square
RHIC	-	Relativistic Heavy Ion Collider
SDD	-	Silicon Drift Detector
SMAQ	-	CTP Trigger Decision Snapshot Monitor
SPD	-	Silicon Pixel Detector
SPS	-	Super Proton Synchrotron
SRU	-	Scalable Readout Unit
SSD	-	Silicon Strip Detector
T0	-	T0 detector
TOF	-	Time of Flight detector
TPC	-	Time Projection Chamber
TRD	-	Transition Radiation Detector
TRU	-	Trigger Region Unit
V0	-	V0 detector
ZDC	-	Zero Degree Calorimeter

REFERENCES

[1] A. Einstein and M. Grossmann, "Entwurf einer verallgemeinerten Relativitätstheorie und eine Theorie der Gravitation. I.," *Zeitschrift für Mathematik und Physik* **62** (1913) 225–261.

[2] **Particle Data Group** Collaboration, C. Patrignani *et al.*, "Review of Particle Physics," *Chin. Phys.* **C40** no. 10, (2016) 100001.

[3] S. L. Glashow, "Partial Symmetries of Weak Interactions," *Nucl. Phys.* **22** (1961) 579–588.

[4] S. Weinberg, "A Model of Leptons," *Phys. Rev. Lett.* **19** (1967) 1264–1266.

[5] S. L. Glashow, J. Iliopoulos, and L. Maiani, "Weak Interactions with Lepton-Hadron Symmetry," *Phys. Rev.* **D2** (1970) 1285–1292.

[6] R. K. Ellis, B. R. Webber, and W. J. Stirling, *QCD and Collider Physics*. Cambridge University Press, 1996.

[7] M. L. Perl, E. R. Lee, and D. Loomba, "A Brief review of the search for isolatable fractional charge elementary particles," *Mod. Phys. Lett.* **A19** (2004) 2595–2610.

[8] F. Halzen and A. D. Martin, *Quarks & Leptons: An Introductory Course in Modern Particle Physics*. John Wiley & Sons, 1984.

[9] T. Renk, "Jet correlations — opportunities and pitfalls," *Nucl. Phys.* **A932** (2014) 334–341, arXiv:1404.0793 [hep-ph].

[10] T. Sjöstrand, S. Mrenna, and P. Z. Skands, "A Brief Introduction to PYTHIA 8.1," *Comput. Phys. Commun.* **178** (2008) 852–867, arXiv:0710.3820 [hep-ph].

[11] T. Sjöstrand, S. Ask, J. R. Christiansen, R. Corke, N. Desai, P. Ilten, S. Mrenna, S. Prestel, C. O. Rasmussen, and P. Z. Skands, "An Introduction to PYTHIA 8.2," *Comput. Phys. Commun.* **191** (2015) 159–177, arXiv:1410.3012 [hep-ph].

[12] M. Bähr *et al.*, "Herwig++ Physics and Manual," *Eur. Phys. J.* **C58** (2008) 639–707, arXiv:0803.0883 [hep-ph].

[13] J. Bellm *et al.*, "Herwig 7.0/Herwig++ 3.0 release note," *Eur. Phys. J.* **C76** no. 4, (2016) 196, arXiv:1512.01178 [hep-ph].

[14] **Crystal Ball** Collaboration, D. Williams *et al.*, "Formation of the Pseudoscalars π^0, η and η' in the Reaction $\gamma\gamma \to \gamma\gamma$," *Phys. Rev.* **D38** (1988) 1365.

[15] D. J. Gross and F. Wilczek, "Asymptotically Free Gauge Theories. 1," *Phys. Rev.* **D8** (1973) 3633–3652.

[16] H. D. Politzer, "Reliable Perturbative Results for Strong Interactions?," *Phys. Rev. Lett.* **30** (1973) 1346–1349.

[17] D. W. Duke and R. G. Roberts, "Analysis of Nucleon Structure Function Moments From Electron and Muon Data and Critical Tests of Asymptotic Freedom," *Phys. Lett.* **85B** (1979) 289–292.

[18] N. K. Nielsen, "Asymptotic Freedom as a Spin Effect," *Am. J. Phys.* **49** (1981) 1171.

[19] A. Deur, S. J. Brodsky, and G. F. de Teramond, "The QCD Running Coupling," *Prog. Part. Nucl. Phys.* **90** (2016) 1–74, arXiv:1604.08082 [hep-ph].

[20] W. A. Bardeen, A. J. Buras, D. W. Duke, and T. Muta, "Deep Inelastic Scattering Beyond the Leading Order in Asymptotically Free Gauge Theories," *Phys. Rev.* **D18** (1978) 3998.

[21] J. C. Collins and M. J. Perry, "Superdense Matter: Neutrons Or Asymptotically Free Quarks?," *Phys. Rev. Lett.* **34** (1975) 1353.

[22] H. H. Gutbrod, A. M. Poskanzer, and H. G. Ritter, "Plastic Ball Experiments," *Rept. Prog. Phys.* **52** (1989) 1267.

[23] **NA35** Collaboration, M. Gazdzicki *et al.*, "Neutral Strange Particle Production in S S Collisions at 200 GeV/nucleon," *Nucl. Phys.* **A498** (1989) 375C–384C. [,647(1989)].

[24] **NA44** Collaboration, I. Bearden *et al.*, "Strange meson enhancement in Pb Pb collisions," *Phys. Lett.* **B471** (1999) 6–12, arXiv:nucl-ex/9907013 [nucl-ex].

[25] **WA97** Collaboration, E. Andersen *et al.*, "Strangeness enhancement at mid-rapidity in Pb Pb collisions at 158 A-GeV/c," *Phys. Lett.* **B449** (1999) 401–406.

[26] **CERES** Collaboration, B. Lenkeit *et al.*, "Recent results from Pb - Au collisions at 158 GeV/c per nucleon obtained with the CERES spectrometer," *Nucl. Phys.* **A661** (1999) 23–32, arXiv:nucl-ex/9910015 [nucl-ex].

[27] **NA50** Collaboration, M. C. Abreu *et al.*, "Anomalous J / psi suppression in Pb - Pb interactions at 158 GeV/c per nucleon," *Phys. Lett.* **B410** (1997) 337–343.

[28] **BRAHMS** Collaboration, I. Arsene *et al.*, "Quark gluon plasma and color glass condensate at RHIC? The Perspective from the BRAHMS experiment," *Nucl. Phys.* **A757** (2005) 1–27, arXiv:nucl-ex/0410020 [nucl-ex].

[29] **PHOBOS** Collaboration, B. B. Back *et al.*, "The PHOBOS perspective on discoveries at RHIC," *Nucl. Phys.* **A757** (2005) 28–101, arXiv:nucl-ex/0410022 [nucl-ex].

[30] **STAR** Collaboration, J. Adams *et al.*, "Experimental and theoretical challenges in the search for the quark gluon plasma: The STAR Collaboration's critical assessment of the evidence from RHIC collisions," *Nucl. Phys.* **A757** (2005) 102–183, arXiv:nucl-ex/0501009 [nucl-ex].

[31] **PHENIX** Collaboration, K. Adcox *et al.*, "Formation of dense partonic matter in relativistic nucleus-nucleus collisions at RHIC: Experimental evaluation by the PHENIX collaboration," *Nucl. Phys.* **A757** (2005) 184–283, arXiv:nucl-ex/0410003 [nucl-ex].

[32] **BRAHMS** Collaboration, I. Arsene *et al.*, "Transverse momentum spectra in Au+Au and d+Au collisions at s**(1/2) = 200 GeV and the pseudorapidity dependence of high p(T) suppression," *Phys. Rev. Lett.* **91** (2003) 072305, arXiv:nucl-ex/0307003 [nucl-ex].

[33] **PHOBOS** Collaboration, B. B. Back *et al.*, "Centrality dependence of charged hadron transverse momentum spectra in d + Au collisions at S(NN)**1/2 = 200 GeV," *Phys. Rev. Lett.* **91** (2003) 072302, arXiv:nucl-ex/0306025 [nucl-ex].

[34] **STAR** Collaboration, J. Adams *et al.*, "Evidence from d + Au measurements for final state suppression of high p(T) hadrons in Au+Au collisions at RHIC," *Phys. Rev. Lett.* **91** (2003) 072304, arXiv:nucl-ex/0306024 [nucl-ex].

[35] **PHENIX** Collaboration, S. S. Adler *et al.*, "Absence of suppression in particle production at large transverse momentum in S(NN)**(1/2) = 200 GeV d + Au collisions," *Phys. Rev. Lett.* **91** (2003) 072303, arXiv:nucl-ex/0306021 [nucl-ex].

[36] D. H. Rischke, "The Quark-Gluon Plasma in Equilibrium," *Prog. Part. Nucl. Phys.* **52** (2004) 197–296, arXiv:nucl-th/0305030 [nucl-th].

[37] Y. Aoki, G. Endrodi, Z. Fodor, S. D. Katz, and K. K. Szabo, "The Order of the quantum chromodynamics transition predicted by the standard model of particle physics," *Nature* **443** (2006) 675–678, arXiv:hep-lat/0611014 [hep-lat].

[38] **STAR** Collaboration, L. Adamczyk *et al.*, "Beam energy dependence of moments of the net-charge multiplicity distributions in Au+Au collisions at RHIC," *Phys. Rev. Lett.* **113** (2014) 092301, arXiv:1402.1558 [nucl-ex].

[39] S. Ejiri, "Canonical partition function and finite density phase transition in lattice QCD," *Phys. Rev.* **D78** (2008) 074507, arXiv:0804.3227 [hep-lat].

[40] G. Odyniec, "Future of the beam energy scan program at RHIC," *EPJ Web Conf.* **95** (2015) 03027.

[41] **FAIR** Collaboration, P. Senger, "Exploring the QCD phase diagram at neutron star densities: the CBM experiment at FAIR," *PoS* **ICPAQGP2015** (2017) 107.

[42] **NICA** Collaboration, A. N. Sissakian and A. S. Sorin, "The nuclotron-based ion collider facility (NICA) at JINR: New prospects for heavy ion collisions and spin physics," *J. Phys.* **G36** (2009) 064069.

[43] "GSI web site." www.gsi.de. Reference date: 2012-09-12.

[44] R. Snellings, "Elliptic Flow: A Brief Review," *New J. Phys.* **13** (2011) 055008, arXiv:1102.3010 [nucl-ex].

[45] P. J. Siemens and J. O. Rasmussen, "Evidence for a blast wave from compress nuclear matter," *Phys. Rev. Lett.* **42** (1979) 880–887.

[46] **ALICE** Collaboration, B. Abelev *et al.*, "Pion, Kaon, and Proton Production in Central Pb–Pb Collisions at $\sqrt{s_{\mathrm{NN}}} = 2.76$ TeV," *Phys. Rev. Lett.* **109** (2012) 252301, arXiv:1208.1974 [hep-ex].

[47] **ALICE** Collaboration, K. Aamodt *et al.*, "Higher harmonic anisotropic flow measurements of charged particles in Pb-Pb collisions at $\sqrt{s_{\mathrm{NN}}}$=2.76 TeV," *Phys. Rev. Lett.* **107** (2011) 032301, arXiv:1105.3865 [nucl-ex].

[48] **ALICE** Collaboration, J. Adam *et al.*, "Correlated event-by-event fluctuations of flow harmonics in Pb-Pb collisions at $\sqrt{s_{\mathrm{NN}}} = 2.76$ TeV," *Phys. Rev. Lett.* **117** (2016) 182301, arXiv:1604.07663 [nucl-ex].

[49] B. H. Alver, C. Gombeaud, M. Luzum, and J.-Y. Ollitrault, "Triangular flow in hydrodynamics and transport theory," *Phys. Rev.* **C82** (2010) 034913, arXiv:1007.5469 [nucl-th].

[50] M. Luzum and J.-Y. Ollitrault, "Extracting the shear viscosity of the quark-gluon plasma from flow in ultra-central heavy-ion collisions," *Nucl. Phys.* **A904-905** (2013) 377c–380c, arXiv:1210.6010 [nucl-th].

[51] H. Niemi, G. S. Denicol, H. Holopainen, and P. Huovinen, "Event-by-event distributions of azimuthal asymmetries in ultrarelativistic heavy-ion collisions," *Phys. Rev.* **C87** no. 5, (2013) 054901, arXiv:1212.1008 [nucl-th].

[52] A. Bilandzic, C. H. Christensen, K. Gulbrandsen, A. Hansen, and Y. Zhou, "Generic framework for anisotropic flow analyses with multiparticle azimuthal correlations," *Phys. Rev.* **C89** no. 6, (2014) 064904, arXiv:1312.3572 [nucl-ex].

[53] **ALICE** Collaboration, S. Acharya *et al.*, "Systematic studies of correlations between different order flow harmonics in Pb-Pb collisions at $\sqrt{s_{\rm NN}}$ = 2.76 TeV," arXiv:1709.01127 [nucl-ex].

[54] J. Qian and U. Heinz, "Hydrodynamic flow amplitude correlations in event-by-event fluctuating heavy-ion collisions," *Phys. Rev.* **C94** no. 2, (2016) 024910, arXiv:1607.01732 [nucl-th].

[55] Z.-W. Lin, C. M. Ko, B.-A. Li, B. Zhang, and S. Pal, "A Multi-phase transport model for relativistic heavy ion collisions," *Phys. Rev.* **C72** (2005) 064901, arXiv:nucl-th/0411110 [nucl-th].

[56] Z.-W. Lin, "Evolution of transverse flow and effective temperatures in the parton phase from a multi-phase transport model," *Phys. Rev.* **C90** no. 1, (2014) 014904, arXiv:1403.6321 [nucl-th].

[57] H. Niemi, K. J. Eskola, and R. Paatelainen, "Event-by-event fluctuations in a perturbative QCD + saturation + hydrodynamics model: Determining QCD matter shear viscosity in ultrarelativistic heavy-ion collisions," *Phys. Rev.* **C93** no. 2, (2016) 024907, arXiv:1505.02677 [hep-ph].

[58] **STAR** Collaboration, C. Adler *et al.*, "Disappearance of back-to-back high p_T hadron correlations in central Au+Au collisions at $\sqrt{s_{\rm NN}}$ = 200 GeV," *Phys. Rev. Lett.* **90** (2003) 082302, arXiv:nucl-ex/0210033 [nucl-ex].

[59] **PHENIX** Collaboration, K. Adcox *et al.*, "Suppression of hadrons with large transverse momentum in central Au+Au collisions at $\sqrt{s_{\rm NN}}$ = 130 GeV," *Phys. Rev. Lett.* **88** (2002) 022301, arXiv:nucl-ex/0109003 [nucl-ex].

[60] **ALICE** Collaboration, K. Aamodt *et al.*, "Suppression of Charged Particle Production at Large Transverse Momentum in Central Pb-Pb Collisions at $\sqrt{s_{\rm NN}} = 2.76$ TeV," *Phys. Lett.* **B696** (2011) 30–39, arXiv:1012.1004 [nucl-ex].

[61] **STAR** Collaboration, B. I. Abelev *et al.*, "Identified baryon and meson distributions at large transverse momenta from Au+Au collisions at s(NN)**(1/2) = 200 GeV," *Phys. Rev. Lett.* **97** (2006) 152301, arXiv:nucl-ex/0606003 [nucl-ex].

[62] **PHENIX** Collaboration, S. S. Adler *et al.*, "Identified charged particle spectra and yields in Au+Au collisions at S(NN)**1/2 = 200 GeV," *Phys. Rev.* **C69** (2004) 034909, arXiv:nucl-ex/0307022 [nucl-ex].

[63] **CMS** Collaboration, S. Chatrchyan *et al.*, "Observation and studies of jet quenching in PbPb collisions at nucleon-nucleon center-of-mass energy = 2.76 TeV," *Phys. Rev.* **C84** (2011) 024906, arXiv:1102.1957 [nucl-ex].

[64] V. Kartvelishvili, R. Kvatadze, and R. Shanidze, "On Z and Z + jet production in heavy ion collisions," *Phys. Lett.* **B356** (1995) 589–594, arXiv:hep-ph/9505418 [hep-ph].

[65] R. B. Neufeld and I. Vitev, "The Z^0-tagged jet event asymmetry in heavy-ion collisions at the CERN Large Hadron Collider," *Phys. Rev. Lett.* **108** (2012) 242001, arXiv:1202.5556 [hep-ph].

[66] R. B. Neufeld, I. Vitev, and B. W. Zhang, "The Physics of Z^0/γ^*-tagged jets at the LHC," *Phys. Rev.* **C83** (2011) 034902, arXiv:1006.2389 [hep-ph].

[67] **CMS** Collaboration, S. Chatrchyan *et al.*, "Studies of jet quenching using isolated-photon+jet correlations in PbPb and pp collisions at $\sqrt{s_{\mathrm{NN}}} = 2.76$ TeV," *Phys. Lett.* **B718** (2013) 773–794, arXiv:1205.0206 [nucl-ex].

[68] **CMS** Collaboration, S. Chatrchyan *et al.*, "Measurement of isolated photon production in pp and PbPb collisions at $\sqrt{s_{\mathrm{NN}}} = 2.76$ TeV," *Phys. Lett.* **B710** (2012) 256–277, arXiv:1201.3093 [nucl-ex].

[69] R. B. Neufeld, I. Vitev, and B. W. Zhang, "The Physics of Z^0/γ^*-tagged jets at the LHC," *Phys. Rev.* **C83** (2011) 034902, arXiv:1006.2389 [hep-ph].

[70] **CMS** Collaboration, A. M. Sirunyan *et al.*, "Study of Jet Quenching with $Z+$jet Correlations in Pb-Pb and pp Collisions at $\sqrt{s_{\mathrm{NN}}} = 5.02$ TeV," *Phys. Rev. Lett.* **119** no. 8, (2017) 082301, arXiv:1702.01060 [nucl-ex].

[71] T. Matsui and H. Satz, "J/ψ Suppression by Quark-Gluon Plasma Formation," *Phys. Lett.* **B178** (1986) 416–422.

[72] S. Digal, P. Petreczky, and H. Satz, "Quarkonium feed down and sequential suppression," *Phys. Rev.* **D64** (2001) 094015, arXiv:hep-ph/0106017 [hep-ph].

[73] **CMS** Collaboration, V. Khachatryan *et al.*, "Suppression of $\Upsilon(1S)$, $\Upsilon(2S)$ and $\Upsilon(3S)$ production in PbPb collisions at $\sqrt{s_{\mathrm{NN}}}$ = 2.76 TeV," *Phys. Lett.* **B770** (2017) 357–379, arXiv:1611.01510 [nucl-ex].

[74] **ALICE** Collaboration, B. Abelev *et al.*, "Long-range angular correlations on the near and away side in p-Pb collisions at $\sqrt{s_{\mathrm{NN}}} = 5.02$ TeV," *Phys. Lett.* **B719** (2013) 29–41, arXiv:1212.2001 [nucl-ex].

[75] **CMS** Collaboration, S. Chatrchyan *et al.*, "Multiplicity and transverse momentum dependence of two- and four-particle correlations in pPb and PbPb collisions," *Phys. Lett.* **B724** (2013) 213–240, arXiv:1305.0609 [nucl-ex].

[76] **ATLAS** Collaboration, G. Aad *et al.*, "Measurement of long-range pseudorapidity correlations and azimuthal harmonics in $\sqrt{s_{\mathrm{NN}}} = 5.02$ TeV proton-lead collisions with the ATLAS detector," *Phys. Rev.* **C90** no. 4, (2014) 044906, arXiv:1409.1792 [hep-ex].

[77] X.-f. Guo, "Jet broadening in deeply inelastic scattering," *Phys. Rev.* **D58** (1998) 114033, arXiv:hep-ph/9804234 [hep-ph].

[78] J.-w. Qiu and G. F. Sterman, "QCD and rescattering in nuclear targets," *Int. J. Mod. Phys.* **E12** (2003) 149, arXiv:hep-ph/0111002 [hep-ph].

[79] A. Krzywicki, J. Engels, B. Petersson, and U. Sukhatme, "Does a Nucleus Act Like a Gluon Filter?," *Phys. Lett.* **85B** (1979) 407–412.

[80] **ATLAS** Collaboration, G. Aad *et al.*, "Light-quark and gluon jet discrimination in pp collisions at $\sqrt{s} = 7$ TeV with the ATLAS detector," *Eur. Phys. J.* **C74** no. 8, (2014) 3023, arXiv:1405.6583 [hep-ex].

[81] T. Sjöstrand and P. Z. Skands, "Transverse-momentum-ordered showers and interleaved multiple interactions," *Eur. Phys. J.* **C39** (2005) 129–154, arXiv:hep-ph/0408302 [hep-ph].

[82] V. N. Gribov and L. N. Lipatov, "Deep inelastic e p scattering in perturbation theory," *Sov. J. Nucl. Phys.* **15** (1972) 438–450. [Yad. Fiz.15,781(1972)].

[83] G. Altarelli and G. Parisi, "Asymptotic Freedom in Parton Language," *Nucl. Phys.* **B126** (1977) 298–318.

[84] Y. L. Dokshitzer, "Calculation of the Structure Functions for Deep Inelastic Scattering and e+ e- Annihilation by Perturbation Theory in Quantum Chromodynamics.," *Sov. Phys. JETP* **46** (1977) 641–653. [Zh. Eksp. Teor. Fiz.73,1216(1977)].

[85] V. V. Sudakov, "Vertex parts at very high-energies in quantum electrodynamics," *Sov. Phys. JETP* **3** (1956) 65–71. [Zh. Eksp. Teor. Fiz.30,87(1956)].

[86] Y. L. Dokshitzer, V. A. Khoze, A. H. Müller, and S. I. Troian, *Basics of Perturbative QCD*. Editions Frontières, Gif-sur-Yvette, France, 1991.

[87] **OPAL** Collaboration, M. Z. Akrawy *et al.*, "A Study of coherence of soft gluons in hadron jets," *Phys. Lett.* **B247** (1990) 617–628.

[88] **TASSO** Collaboration, W. Braunschweig *et al.*, "Global Jet Properties at 14 GeV to 44 GeV Center-of-mass Energy in e^+e^- Annihilation," *Z. Phys.* **C47** (1990) 187–198.

[89] Y. I. Azimov, Y. L. Dokshitzer, V. A. Khoze, and S. I. Troyan, "Similarity of Parton and Hadron Spectra in QCD Jets," *Z. Phys.* **C27** (1985) 65–72.

[90] S. Catani, Y. L. Dokshitzer, M. H. Seymour, and B. R. Webber, "Longitudinally invariant K_t clustering algorithms for hadron hadron collisions," *Nucl. Phys.* **B406** (1993) 187–224.

[91] S. D. Ellis and D. E. Soper, "Successive combination jet algorithm for hadron collisions," *Phys. Rev.* **D48** (1993) 3160–3166, arXiv:hep-ph/9305266 [hep-ph].

[92] Y. L. Dokshitzer, G. D. Leder, S. Moretti, and B. R. Webber, "Better jet clustering algorithms," *JHEP* **08** (1997) 001, arXiv:hep-ph/9707323 [hep-ph].

[93] M. Cacciari, G. P. Salam, and G. Soyez, "The Anti-k(t) jet clustering algorithm," *JHEP* **04** (2008) 063, arXiv:0802.1189 [hep-ph].

[94] A. Buckley *et al.*, "General-purpose event generators for LHC physics," *Phys. Rept.* **504** (2011) 145–233, arXiv:1101.2599 [hep-ph].

[95] J. C. Collins, D. E. Soper, and G. F. Sterman, "Factorization for Short Distance Hadron - Hadron Scattering," *Nucl. Phys.* **B261** (1985) 104–142.

[96] H. U. Bengtsson, "The Lund Monte Carlo for High p_{T} Physics," *Comput. Phys. Commun.* **31** (1984) 323.

[97] H. U. Bengtsson and G. Ingelman, "The Lund Monte Carlo for High p_{T} Physics," *Comput. Phys. Commun.* **34** (1985) 251.

[98] H.-U. Bengtsson and T. Sjöstrand, "The Lund Monte Carlo for Hadronic Processes: Pythia Version 4.8," *Comput. Phys. Commun.* **46** (1987) 43.

[99] T. Sjöstrand, "High-energy physics event generation with PYTHIA 5.7 and JETSET 7.4," *Comput. Phys. Commun.* **82** (1994) 74–90.

[100] T. Sjöstrand, P. Eden, C. Friberg, L. Lonnblad, G. Miu, S. Mrenna, and E. Norrbin, "High-energy physics event generation with PYTHIA 6.1," *Comput. Phys. Commun.* **135** (2001) 238–259, arXiv:hep-ph/0010017 [hep-ph].

[101] T. Sjöstrand, S. Mrenna, and P. Z. Skands, "PYTHIA 6.4 Physics and Manual," *JHEP* **05** (2006) 026, arXiv:hep-ph/0603175 [hep-ph].

[102] T. Sjöstrand, "The Lund Monte Carlo for Jet Fragmentation," *Comput. Phys. Commun.* **27** (1982) 243.

[103] T. Sjöstrand, "The Lund Monte Carlo for e+ e- Jet Physics," *Comput. Phys. Commun.* **28** (1983) 229.

[104] T. Sjöstrand, "The Lund Monte Carlo for Jet Fragmentation and e+ e- Physics: Jetset Version 6.2," *Comput. Phys. Commun.* **39** (1986) 347–407.

[105] T. Sjöstrand and M. Bengtsson, "The Lund Monte Carlo for Jet Fragmentation and e+ e- Physics. Jetset Version 6.3: An Update," *Comput. Phys. Commun.* **43** (1987) 367.

[106] B. Andersson, G. Gustafson, G. Ingelman, and T. Sjöstrand, "Parton Fragmentation and String Dynamics," *Phys.Rept.* **97** (1983) 31–145.

[107] G. Marchesini and B. R. Webber, "Monte Carlo Simulation of General Hard Processes with Coherent QCD Radiation," *Nucl. Phys.* **B310** (1988) 461–526.

[108] S. Gieseke, P. Stephens, and B. Webber, "New formalism for QCD parton showers," *JHEP* **12** (2003) 045, arXiv:hep-ph/0310083 [hep-ph].

[109] D. Amati and G. Veneziano, "Preconfinement as a Property of Perturbative QCD," *Phys. Lett.* **83B** (1979) 87–92.

[110] "CERN Experiments." https://home.cern/about/experiments. Reference date: 2017-03-09.

[111] L. Evans and P. Bryant, "LHC Machine," *JINST* **3** (2008) S08001.

[112] "LHC Programme Coordination." https://lpc.web.cern.ch/Default.htm. Reference date: 2017-09-19.

[113] **ALICE** Collaboration, K. Aamodt *et al.*, "The ALICE experiment at the CERN LHC," *JINST* **3** (2008) S08002.

[114] **ALICE** Collaboration, K. Aamodt *et al.*, "Elliptic flow of charged particles in Pb-Pb collisions at 2.76 TeV," *Phys. Rev. Lett.* **105** (2010) 252302, arXiv:1011.3914 [nucl-ex].

[115] **ATLAS** Collaboration, G. Aad *et al.*, "The ATLAS Experiment at the CERN Large Hadron Collider," *JINST* **3** (2008) S08003.

[116] **CMS** Collaboration, S. Chatrchyan *et al.*, "The CMS Experiment at the CERN LHC," *JINST* **3** (2008) S08004.

[117] **ATLAS** Collaboration, G. Aad *et al.*, "Observation of a new particle in the search for the Standard Model Higgs boson with the ATLAS detector at the LHC," *Phys. Lett.* **B716** (2012) 1–29, arXiv:1207.7214 [hep-ex].

[118] **CMS** Collaboration, S. Chatrchyan *et al.*, "Observation of a new boson at a mass of 125 GeV with the CMS experiment at the LHC," *Phys. Lett.* **B716** (2012) 30–61, arXiv:1207.7235 [hep-ex].

[119] **LHCb** Collaboration, A. A. Alves, Jr. *et al.*, "The LHCb Detector at the LHC," *JINST* **3** (2008) S08005.

[120] **LHCb** Collaboration, R. Aaij *et al.*, "First Evidence for the Decay $B_s^0 \to \mu^+\mu^-$," *Phys. Rev. Lett.* **110** no. 2, (2013) 021801, arXiv:1211.2674 [hep-ex].

[121] **LHCf** Collaboration, O. Adriani *et al.*, "The LHCf detector at the CERN Large Hadron Collider," *JINST* **3** (2008) S08006.

[122] **TOTEM** Collaboration, G. Anelli *et al.*, "The TOTEM experiment at the CERN Large Hadron Collider," *JINST* **3** (2008) S08007.

[123] **MoEDAL** Collaboration, B. Acharya *et al.*, "Search for magnetic monopoles with the MoEDAL prototype trapping detector in 8 TeV proton-proton collisions at the LHC," *JHEP* **08** (2016) 067, arXiv:1604.06645 [hep-ex].

[124] **TOTEM** Collaboration, G. Antchev *et al.*, "Luminosity-independent measurements of total, elastic and inelastic cross-sections at $\sqrt{s} = 7$ TeV," *EPL* **101** no. 2, (2013) 21004.

[125] "ALICE figure repository." https://aliceinfo.cern.ch/Figure/. Reference date: 2017-12-04.

[126] **ALICE** Collaboration, K. Aamodt *et al.*, "Charged-particle multiplicity density at mid-rapidity in central Pb-Pb collisions at $\sqrt{s_{\mathrm{NN}}} = 2.76$ TeV," *Phys. Rev. Lett.* **105** (2010) 252301, arXiv:1011.3916 [nucl-ex].

[127] **ALICE** Collaboration, *Technical Design Report of the Time Projection Chamber*, January, 2000. CERN-OPEN-2000-183, CERN-LHCC-2000-001.

[128] **ALICE** Collaboration, *Technical Design Teport of the Inner Tracking System (ITS)*, June, 1999. CERN-LHCC-99-12.

[129] **ALICE** Collaboration, *Technical Design Report of the Transition Radiation Detector*, October, 2001. ALICE-TDR-9, CERN-LHCC-2001-021, LYCEN-2001-97.

[130] **ALICE** Collaboration, *Addendum to the Technical Design Report of the Time of Flight System (TOF)*, April, 2002. CERN-LHCC-2002-016.

[131] **ALICE** Collaboration, *Technical Design Report of the High Momentum Particle Identification Detector*, August, 1998. CERN-LHCC-98-19.

[132] **ALICE** Collaboration, B. Abelev *et al.*, "Neutral pion and η meson production in proton-proton collisions at $\sqrt{s} = 0.9$ TeV and $\sqrt{s} = 7$ TeV," *Phys. Lett.* **B717** (2012) 162–172, arXiv:1205.5724 [hep-ex].

[133] **ALICE** Collaboration, J. Adam *et al.*, "Direct photon production in Pb-Pb collisions at $\sqrt{s_{\rm NN}} = 2.76$ TeV," *Phys. Lett.* **B754** (2016) 235–248, arXiv:1509.07324 [nucl-ex].

[134] **ALICE** Collaboration, *Electromagnetic Calorimeter Technical Design Report*, September, 2008. CERN-LHCC-2008-014, CERN-ALICE-TDR-014.

[135] **ALICE** Collaboration, *Technical Design Report of the Photon Ppectrometer (PHOS)*, March, 1999. CERN-LHCC-99-04.

[136] **ALICE** Collaboration, *ALICE DCal: An Addendum to the EMCal Technical Design Report Di-Jet and Hadron-Jet Correlation Measurements in ALICE*, June, 2010. CERN-LHCC-2010-011, ALICE-TDR-14-add-1.

[137] **ALICE** Collaboration, *Addendum to the Technical Design Report of the Dimuon Forward Spectrometer*, December, 2000. ALICE-TDR-5-add-1, CERN-LHCC-2000-046.

[138] **ALICE** Collaboration, *Technical Design Report on Forward Detectors: FMD, T0 and V0*, September, 2004. CERN-LHCC-2004-025.

[139] **ALICE** Collaboration, B. Abelev *et al.*, "Centrality determination of Pb-Pb collisions at $\sqrt{s_{\rm NN}}$ = 2.76 TeV with ALICE," *Phys. Rev.* **C88** no. 4, (2013) 044909, arXiv:1301.4361 [nucl-ex].

[140] **ALICE** Collaboration, *Addendum to the Technical Design Report of the Photon Multiplicity Detector (PMD)*, September, 2003. CERN-LHCC-2003-038.

[141] **ACORDE** Collaboration, A. Fernández *et al.*, "ACORDE a Cosmic Ray Detector for ALICE," *Nucl. Instrum. Meth.* **A572** (2007) 102–103, arXiv:physics/0606051 [physics].

[142] **ALICE** Collaboration, *Technical Design Report of the Zero Degree Calorimeter (ZDC)*, March, 1999. CERN-LHCC-99-05.

[143] **ALICE** Collaboration, J. Adam *et al.*, "Centrality dependence of particle production in p-Pb collisions at $\sqrt{s_{\rm NN}}$= 5.02 TeV," *Phys. Rev.* **C91** no. 6, (2015) 064905, arXiv:1412.6828 [nucl-ex].

[144] J.-C. Cabanillas-Noris, M. I. Martinez, and I. L. Monzon, "ALICE Diffractive Detector Control System for RUN-II in the ALICE Experiment," *J. Phys. Conf. Ser.* **761** no. 1, (2016) 012025, arXiv:1609.08056 [physics.ins-det].

[145] J.-P. Revol, E. Calvo Villar, and C. Mayer, "General Charasteristics of the AD Detector." Alice public note pub-3033, April, 2016.

[146] J. Kral, T. Awes, H. Muller, J. Rak, and J. Schambach, "L0 trigger for the EMCal detector of the ALICE experiment," *Nucl. Instrum. Meth.* **A693** (2012) 261–267.

[147] **ALICE** Collaboration, B. B. Abelev *et al.*, "Performance of the ALICE Experiment at the CERN LHC," *Int. J. Mod. Phys.* **A29** (2014) 1430044, arXiv:1402.4476 [nucl-ex].

[148] J. F. Grosse-Oetringhaus, *Measurement of the Charged-Particle Multiplicity in Proton-Proton Collisions with the ALICE Detector*. PhD thesis, Munster U., 2009. http://inspirehep.net/record/887184/files/CERN-THESIS-2009-033.pdf.

[149] R. Frühwirth, "Application of Kalman filtering to track and vertex fitting," *Nucl. Instrum. Meth.* **A262** (1987) 444–450.

[150] **ALICE** Collaboration, "The ALICE definition of primary particles,". https://cds.cern.ch/record/2270008.

[151] **CMS** Collaboration, V. Khachatryan *et al.*, "Observation of Long-Range Near-Side Angular Correlations in Proton-Proton Collisions at the LHC," *JHEP* **09** (2010) 091, arXiv:1009.4122 [hep-ex].

[152] **ATLAS** Collaboration, G. Aad *et al.*, "Observation of Long-Range Elliptic Azimuthal Anisotropies in $\sqrt{s}$ =13 and 2.76 TeV pp Collisions with the ATLAS Detector," *Phys. Rev. Lett.* **116** no. 17, (2016) 172301, arXiv:1509.04776 [hep-ex].

[153] **CMS** Collaboration, S. Chatrchyan *et al.*, "Observation of long-range near-side angular correlations in proton-lead collisions at the LHC," *Phys. Lett.* **B718** (2013) 795–814, arXiv:1210.5482 [nucl-ex].

[154] **ATLAS** Collaboration, G. Aad *et al.*, "Observation of Associated Near-Side and Away-Side Long-Range Correlations in $\sqrt{s_{\mathrm{NN}}} = 5.02$ TeV Proton-Lead Collisions with the ATLAS Detector," *Phys. Rev. Lett.* **110** no. 18, (2013) 182302, arXiv:1212.5198 [hep-ex].

[155] **CMS** Collaboration, S. Chatrchyan *et al.*, "Studies of azimuthal dihadron correlations in ultra-central PbPb collisions at $\sqrt{s_{\mathrm{NN}}} = 2.76$ TeV," *JHEP* **02** (2014) 088, arXiv:1312.1845 [nucl-ex].

[156] **ATLAS** Collaboration, J. Jia, "Measurement of elliptic and higher order flow from ATLAS experiment at the LHC," *J. Phys.* **G38** (2011) 124012, arXiv:1107.1468 [nucl-ex].

[157] **ALICE** Collaboration, B. Abelev *et al.*, "Underlying Event measurements in pp collisions at $\sqrt{s} = 0.9$ and 7 TeV with the ALICE experiment at the LHC," *JHEP* **07** (2012) 116, arXiv:1112.2082 [hep-ex].

[158] **ATLAS** Collaboration, G. Aad *et al.*, "Measurement of the jet fragmentation function and transverse profile in proton-proton collisions at a center-of-mass energy of 7 TeV with the ATLAS detector," *Eur. Phys. J.* **C71** (2011) 1795, arXiv:1109.5816 [hep-ex].

[159] F. James, *Statistical Methods in Experimental Physics*. World Scientific, 2nd edition ed., 2008.

[160] **ALICE** Collaboration, B. B. Abelev *et al.*, "Energy Dependence of the Transverse Momentum Distributions of Charged Particles in pp Collisions Measured by ALICE," *Eur. Phys. J.* **C73** no. 12, (2013) 2662, arXiv:1307.1093 [nucl-ex].

[161] **ALICE** Collaboration, B. B. Abelev *et al.*, "Transverse momentum dependence of inclusive primary charged-particle production in p-Pb collisions at $\sqrt{s_{\rm NN}} = 5.02$ TeV," *Eur. Phys. J.* **C74** no. 9, (2014) 3054, arXiv:1405.2737 [nucl-ex].

[162] **CCOR** Collaboration, A. Angelis *et al.*, "A Measurement of the Transverse Momenta of Partons, and of Jet Fragmentation as a Function of $\sqrt{s}$ in pp Collisions," *Phys. Lett.* **B97** (1980) 163–168.

[163] **PHENIX** Collaboration, S. S. Adler *et al.*, "Jet properties from dihadron correlations in p+p collisions at $\sqrt{s} = 200$ GeV," *Phys. Rev.* **D74** (2006) 072002, arXiv:hep-ex/0605039 [hep-ex].

[164] R. Corke and T. Sjostrand, "Interleaved Parton Showers and Tuning Prospects," *JHEP* **03** (2011) 032, arXiv:1011.1759 [hep-ph].

[165] P. Skands, S. Carrazza, and J. Rojo, "Tuning PYTHIA 8.1: the Monash 2013 Tune," *Eur. Phys. J.* **C74** no. 8, (2014) 3024, arXiv:1404.5630 [hep-ph].

[166] "Minimum bias tunes for Herwig." https://herwig.hepforge.org/tutorials/mpi/tunes.html. Reference date: 2017-11-20.

[167] **ALICE** Collaboration, J. Adam *et al.*, "Evolution of the longitudinal and azimuthal structure of the near-side jet peak in Pb-Pb collisions at $\sqrt{s_{\rm NN}} = 2.76$ TeV," *Phys. Rev.* **C96** no. 3, (2017) 034904, arXiv:1609.06667 [nucl-ex].

[168] C. A. Salgado and U. A. Wiedemann, "Medium modification of jet shapes and jet multiplicities," *Phys. Rev. Lett.* **93** (2004) 042301, arXiv:hep-ph/0310079 [hep-ph].

[169] Y. Mehtar-Tani, C. A. Salgado, and K. Tywoniuk, "Anti-angular ordering of gluon radiation in QCD media," *Phys. Rev. Lett.* **106** (2011) 122002, arXiv:1009.2965 [hep-ph].

[170] Y.-T. Chien and I. Vitev, "Towards the understanding of jet shapes and cross sections in heavy ion collisions using soft-collinear effective theory," *JHEP* **05** (2016) 023, arXiv:1509.07257 [hep-ph].

[171] **ALICE** Collaboration, K. Aamodt *et al.*, "Charged-particle multiplicity measurement in proton-proton collisions at $\sqrt{s} = 7$ TeV with ALICE at LHC," *Eur. Phys. J.* **C68** (2010) 345–354, arXiv:1004.3514 [hep-ex].

[172] E. B. Moral, "Analysis of the fragmentation function based on ATLAS data on proton-proton collisions at $\sqrt{s} = 7$ TeV," Master's thesis, University of Jyväskylä, 2016.

[173] M. Cacciari, G. P. Salam, and G. Soyez, "FastJet User Manual," *Eur. Phys. J.* **C72** (2012) 1896, arXiv:1111.6097 [hep-ph].